LOW PLATINUM ELECTRODES FOR PROTON EXCHANGE FUEL CELLS MANUFACTURED BY REACTIVE SPRAY DEPOSITION TECHNOLOGY

by

Justin Roller

A THESIS SUBMITTED IN PARTIAL FULFILLMENT OF THE REQUIREMENTS FOR THE DEGREE OF

MASTER OF APPLIED SCIENCE

in

The Faculty of Graduate Studies

(Mechanical Engineering)

THE UNIVERSITY OF BRITISH COLUMBIA
Vancouver

February 2009

Abstract

Reactive spray deposition technology (RSDT) is a method of depositing films or producing nanopowders through combustion of metal-organic compounds dissolved in a solvent. This technology produces powders of controllable size and quality by changing process parameters to control the stoichiometry of the final product. This results in a low-cost, continuous production method suitable for producing a wide range of fuel cell related catalyst films or powders. In this work, the system is modified for direct deposition of both unsupported and carbon supported layers on proton exchange membrane (PEM) fuel cells. The cell performance is investigated for platinum loadings of less than 0.15 mg/cm^2 using a heterogeneous bi-layer consisting of a layer of unsupported platinum followed by a composite layer of Nafion®, carbon and platinum. Comparison to more traditional composite cathode architectures is made at loadings of 0.12 and 0.05 $mg_{platinum}/cm^2$. The composition and phase of the platinum catalyst is confirmed by XPS and XRD analysis while the particle size is analyzed by TEM microscopy. Cell voltages of 0.60 V at 1 A/cm^2 using H_2/O_2 at a loading of 0.053 $mg_{platinum}/cm^2$ have been achieved.

Table of contents

List of tables

List of figures

Acknowledgements

This thesis is dedicated to my beautiful daughter Lily Roller and more broadly to the next generation of children who will inherit a world struggling to cope with climate change and the societal challenges of an energy constrained world.

I would like to thank Dave Ghosh and Maya Veljkovic at the National Research Council's Institute for Fuel Cell Innovation for flexibility in allowing me the opportunity to explore further educational pursuits while maintaining gainful employment. I would also like to specifically honor my manager and dear friend, Radenka Maric for her unwavering support. This support has extended far beyond issues of mundane technical discussion and has helped me to understand the meaning of happiness, the need for gratitude and importance of relationships.

This work in many ways represents a collaborative effort and would not have been possible without the assistance of Marius Dinu, Adam Tuck, Khalid Fatih and Makoto Adichi. However, I would like to individually express my gratitude and deep respect for the valuable knowledge, work, experience and friendship that Roberto Neagu has extended to me on this project. His generous sharing of himself, ability to make a great cappuccino and persistent dedication to excellence in scientific pursuit makes him a truly special colleague. Furthermore, we enjoyed many hours discussing the merits of fundamental scientific work versus science for profit and he always patiently lent an ear to hear my frustrations on the state of the environment.

Dr. Olivera Kesler deserves special recognition. I learned a great deal over the last three years both through coursework and through our interactions and

discussions. I appreciate your ability to motivate me to finish this work when at times I was too distracted by work and personal pursuits.

Dr. Walter Merida has been an excellent coach and has been my cheerleader throughout the last year of the project. His constant optimism and positive demeanor have helped me during the times I felt defeated.

Finally, I would like to thank my wife Osha Roller for her support and understanding during the last three years. There has been a great deal of family sacrifice and her unending love, encouragement and understanding are deeply appreciated.

1 Literature review

1.1.1 Introduction

Energy security and environmental concerns are projected to be a dominant theme in research and development in the next half century. Nobel prize winner Richard Smalley is quoted as saying “Energy is the single most important challenge facing humanity today…We should assume that by the middle of this century we will need to at least double world energy production from its current level, with most of this coming from some clean, sustainable, carbon dioxide–free source” (1). The 2006 World Energy Outlook predicts that global energy demand will grow by more than half over the next quarter of a century, with coal use rising most in absolute terms (2).

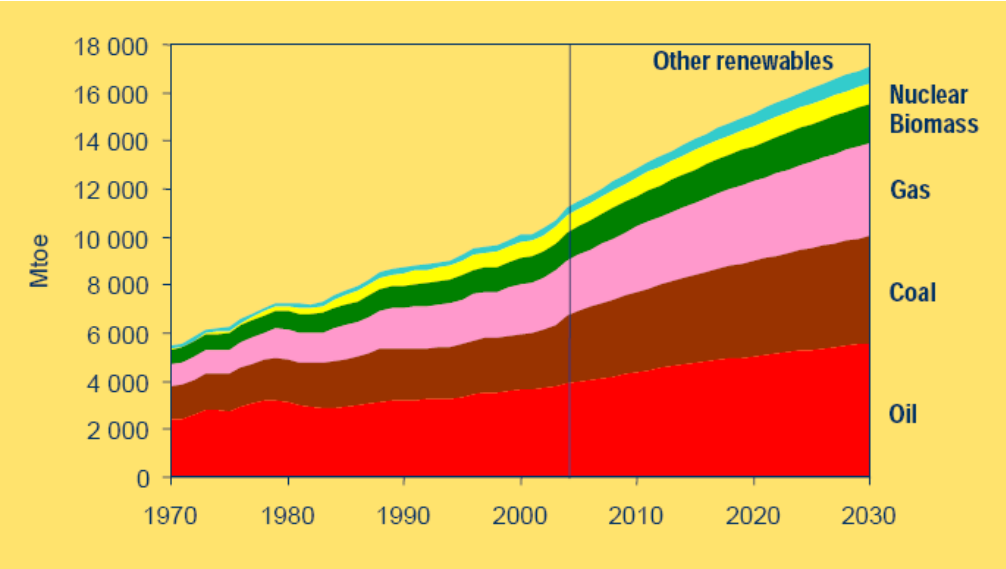

Figure 1: World energy demand to 2030 by primary energy source [© OECD/IEA, 2006, World Energy Outlook 2006] (2)

The report further states, “The need to curb growth in fossil-energy demand, to increase geographic and fuel-supply diversity and to mitigate climate-destabilizing emissions is more urgent than ever.”

The Polymer Electrolyte Fuel Cell (PEM) offers the possibility to address several pieces of the energy puzzle related to effective use of stored hydrogen from renewables and to provide transportation options with zero point of use emissions using zero-emission vehicles (ZEV). PEM fuel cells can also be utilized to provide power for stationary applications and for auxiliary power units and portable power. ZEV's can shift emissions due to fuel production to localized areas. Localization would be centered where the primary energy source used for hydrogen production is abundant and cheap. In general the transmission grid operates on a "use it or lose it" principle with regards to electrical generation. Since wind and solar are intermittent sources of electrical generation, the potential to store that excess capacity into a transportable fuel as hydrogen through a smart-grid and electrolysis is an exciting avenue of development. Though the process of energy transformation, storage and final use is inefficient, this drawback is partially negated by the fact that the energy would be lost if not collected in the first place.

Hydrogen can be derived from other primary energy sources such as nuclear and alternative technologies through electrolysis or by fossil fuels through steam methane reforming or multi-fuel gasification. While large quantities of hydrogen (>95% in North America) are currently produced at reasonable cost by steam reformation of methane, this source relies on a limited fossil resource (natural gas) and releases greenhouse gas (CO_2). Due to uncertainties in the regional long term supply and cost estimates of natural gas, investments in fuel flexible fuel cells that take inputs from a wide range of renewables makes business and supply security sense. Other primary energy sources hold the promise of producing hydrogen without carbon dioxide emissions, but all of these are still in early development phases or require dirty primary energy sources to produce the energy necessary for hydrogen manufacture. These include thermochemical water-splitting using nuclear and solar heat; photolytic (solar) processes using solid state techniques (photoelectrochemical electrolysis), fossil fuel hydrogen production with carbon sequestration, and biological techniques (algae and bacteria). Uncertainty in the policy outlook for CO_2 intensive industries

warrants an eventual move away from these sources as primary sources for hydrogen although the timescale for this transformation is hotly debated.

Due to the difficulty in committing long-term capital expenditures in an uncertain policy environment, several large companies including DuPont and General Electric have formed an alliance to demand action on CO_2 emissions(3). Additionally, PEM fuel cells with changes in catalyst composition can use bio-fuels such as methanol and formic acid for power generation. Methanol can be produced from biomass and offers another piece in the transitional move toward energy security, fuel flexibility and renewability. By-products of industrial processes also offer smaller scale applications for increased process efficiency. Using hydrogen as a by-product from the manufacture of ammonia and formic acid is an example aimed at closing the life cycle loop in the production cycle.

Future energy scenarios will be increasingly dependant upon local sources of primary energy and products that can capitalize on these regional solutions will be well placed for future markets. The overall energy efficiency in fuel cell operation serves to extend the use of existing resources, in certain applications, and thus has the win-win result of reducing air pollution and saving energy. The cost of carbon dioxide emissions will be subject to rigorous political debate but the Kyoto Protocol provides insight into the future cost structures of these emissions. Existing energy policies do not promote consideration of the external environmental and security costs of non-renewable energy that would encourage wider use of hydrogen, renewables and alternative fuels. Due to government policies related to oil and gas industry subsidies, hydrogen and alternative fuels have to compete with artificially cheap non-renewables(4). Proposed policy changes and the general public's attitude appear to be shifting toward changes in legislation that would internalize the costs of industrial activities that are carbon intensive. Positioning to account for these changes makes business sense in the long term and monetary sense in the short.

PEM technology offers, at the conversion stage, an electrical generation efficiency over that of traditional internal combustion engines. However, the well-to-wheel efficiency depends greatly on the primary source of energy for the

hydrogen. Hydrogen or methanol will be beneficially useful for storing energy from intermittent sources (i.e. wind, tidal and solar) that are not immediately available for direct input to the grid or in locations too remote for grid addition. The efficacy of this model is very promising if the hydrogen is also used locally. Transportation of the hydrogen over long distances correspondingly reduces the well-to-wheel efficiency. Methanol offers even better storage prospects than hydrogen due to an increased energy density, an existing liquid handling infrastructure and a lower leakage rate during storage. However, poor electrical efficiency compared to hydrogen, due to electrolyte crossover, and biological toxicity are hurdles to commercialization.

Cost, reliability of performance and durability are the major challenges to fuel cell commercialization. It must be stressed that hurdles vary according to the application in which the technology is employed. Depending on the application, requirements such as: cost, size, weight or water management are barriers to commercialization. In transportation applications, these technologies face more stringent cost and durability hurdles. Due to the monetary capitalization and volume of the auto industry this niche is seen as the ultimate goal in market penetration for the PEM industry. In stationary power applications, where cogeneration of heat and power is desired, use of PEM fuel cells would benefit from raising the operating temperatures to increase performance.

1.1.2 Economics and barriers to market penetration of fuel cells

Currently the costs for automotive internal combustion engines (ICE) are about $25-$35/kW; for transportation applications, a fuel cell system needs to cost $30/kW for the technology to be competitive with the internal combustion engine. For stationary systems, the acceptable price point is considerably higher ($400-$750/kW for widespread commercialization and as much as $1000/kW for initial applications).

In order to attain market penetration in the automotive field there must be a reduction in cost and a concurrent increase in lifetime of the membrane electrode assembly (MEA) itself. It is well known that upfront manufacturing and performance cost reductions cannot come at the expense of durability and vice versa. The electrodes make up almost half of the MEA cost and so increases in efficiency and manufacturing advances in this area are expected to have big impacts in the overall cost structure(5). Cost reduction through understanding the physical and microstructural makeup of carbon supported and non-supported platinum electrodes for oxygen reduction in proton exchange fuel cells (PEM) is the primary focus of this thesis.

Electrode cost is the combined price of several variables: catalyst mass, unrecyclable material losses during manufacturing, electrode manufacturing time (i.e. scalability) and scrap rate. Catalyst mass is itself a compounded cost variable which is a function of activity and composition. Many interesting and novel procedures for catalyst manufacture have demonstrated very promising results but languish in the realm of scientific curiosity due to lack of scalability; therefore, it is imperative that forethought be given to the design of any electrode manufacturing system in regards to scale-up from the beginning.

Ideally the optimal deposition methodology will: (i) increase utilization, (ii) result in very low catalyst loading, (iii) prevent excessive temperature exposure to the electrolyte, (iv) scale easily, and (v) exhibit acceptable reproducibility. A further benefit is versatility of the system to achieve wide ranges in desired characteristics of catalysts. However, this too can come at the expense of repeatability if the process parameters are not well understood or controlled.

The relative merits for a fabrication process are cost, performance, and reliability because the electrode structure (porosity, thickness, catalyst type and ionomer content) is not only a function of the electrocatalyst composition itself but also of the way in which it is formed or deposited. Raw material cost reduction takes the form of improved catalyst utilization and alternative formulations, while manufacturing costs are driven down by reducing the number of processing steps, using continuous processing, and avoiding energy- or time-intensive steps

such as vacuum environments. There is a distinct need for techniques capable of handling high fuel cell catalyst production volumes and achieving better consistency and quality control. Advancements in this area are one of the surest means to achieving the large cost reductions needed to move fuel cells from niche to mass markets.

The US DOE through its Hydrogen Fuel Initiative has proposed the following cost targets for fuel cell development. For the automotive sector develop a 60% peak efficient, durable, direct hydrogen fuel cell power system for transportation at a cost of $45/kW by 2010 and $30/kW by 2015. Automotive ICE power plants currently cost $25-35/kW, so a fuel cell system needs to come down in price to below $50/kW at current market conditions. It should be noted, however, that current market conditions are based on the assumption of cheap and plentiful fossil fuel as the primary energy input, and the long term prognosis for this situation has come under considerable doubt(6). For stationary applications the goal is to develop a distributed generation polymer electrolyte membrane fuel cell operating on natural gas or liquid petroleum gas that achieves 40% electrical efficiency and 40,000 hours durability at $400-750/kW by 2010.

A significant cost of the PEM fuel cell comes from the precious metal catalysts that are used on the anode and cathode for electrochemical reactions. Fuel cell power systems will be required to be as durable and reliable as current automotive engines with a 5,000 hr lifetime, which corresponds to a 150,000 mile equivalent, and be able to function over a full range of external environmental conditions (-40 to 40 ^{o}C). Platinum sintering and dissolution, especially under conditions of load-cycling and high electrode potentials, are the focus of durability improvements. Carbon support corrosion is another challenge at high electrode potentials and can worsen under load cycling and high temperature operations.

1.1.3 Platinum as a cost barrier

The most common and studied material for catalyzing the oxygen reduction reaction in PEMFCs is platinum metal. However, raw material costs, fabrication process limitations, knowledge gaps in structure/functionality relationships and processing time still limit broader PEM system appeal. Cost targets for PEM penetration into the automotive area are constrained by the price and supply of platinum (7). Over 50% of the cost of a fuel cell is dominated by the cost of the electrodes (8). Cost targets of $30/kW as expressed by the United States Department of Energy can be met if Pt-specific power density can be reduced to < $0.2 g_{Pt}$ /kW at cell voltages >0.65 V (>55% conversion efficiency)(9). This cost reduction can be achieved by increasing the power density to 0.8-0.9 W/cm^2_{mea} at >.65 V by reducing mass transport losses at higher current densities and by reducing Pt-loading in MEAs to ca. 0.15 mg_{Pt}/cm^2_{mea}. High power densities are needed to reduce the volumetric power density (kW/L) for automotive applications but also to reduce the cost of additional costly stack component materials. Cell voltages greater than .65 V are needed for high-energy conversion efficiency and to minimize heat rejection. However, achievement of these performance goals still correspond to a platinum cost of $15/kW as the cost of platinum is currently traded at $2000 USD/ounce. This leaves an almost unattainable remainder of $15/kW for the rest of the system to reach DOE targets.

As explained by Gasteiger in 2005, currently applied membrane/electrode assembly (MEA) loadings of ca. 0.6–0.8 $mgPt/cm^2$, with power densities up to 0.7 W/cm^2 at cell voltages as high as 0.68 V correspond to Pt-specific power densities of 0.85–1.1 g_{pt}/kW, translating into 72–94 g of platinum for a ca. 85 kW fuel cell stack in a 75 kW_{net} automotive fuel cell system. A lowering of cathode loadings from circa 0.4 $mg_{Pt}/cm^2_{cathode}$ is limited by the activity of platinum for the oxygen reduction reaction (ORR) at such small loadings. Reduction of loading to a critical lower threshold is an effective strategy for reducing platinum requirements in the cathode. However, below this threshold an optimization of

the electrode structure is crucial so that the effect of reducing the cathode platinum loading is limited to the purely Tafel predicted voltage loss over the entire current density range (i.e. 20 mV for lowering the loading from 0.4 – 0.2 mg_Pt/cm^2). The ORR kinetic loss is evaluated based on the oxygen pressure in the flow channel and increases as O_2 concentration decreases, which follows the O_2 pressure dependence of the ORR kinetics. Another strategy for cost reduction is implementation of Pt-alloy catalysts. Alloys often offer enhancement at lower current densities but at higher current densities issues, of leaching and low metal dispersion compared to Pt/C catalysts are evident. It should also be noted that the choice of alloy must meet increasingly stringent environmental regulations that may limit options such as chromium metals.

1.2 Proton exchange membrane cathodes

1.2.1 Oxygen reduction reaction as major limitation of PEM fuel cells

The performance of a PEM fuel cell is overwhelmingly limited by the slow oxygen reduction reaction (ORR) at the cathode. This reaction is the 'bottle-neck' at temperature ranges, 30-80^oC, commonly used for polymer electrolyte fuel cells and thus limits the choice of catalyst materials used in cell manufacture. The current architecture favored for oxygen reduction electrodes in proton exchange membrane (PEM) fuel cells is based on carbon supported platinum mixed with Nafion®. The relationship between the electrode structure and mass transfer properties in the electrodes is still an area of intense research, and many gaps in knowledge and disagreements over mechanisms exist. Oxygen reduction at the cathode requires both electron and proton transport, as shown in:

$$O_2 + 4\ e^- + 4\ H^+ \rightarrow 2H_2O \qquad (1)$$

Electron transport is provided by a carbon support, while Nafion® transports protons to the active platinum sites. Oxygen must diffuse through the pore network to reach the platinum. The complicated reaction pathway is believed to

only occur in areas where platinum is resting on carbon and is touched by both electrolyte-connected ionomer and pores for gas diffusion. These areas are known as three or triple phase boundaries owing to the requirement for a nexus of gas, liquid and solid.

1.2.2 Performance targets and state of MEA performance

Current state of the art single cell performance (with H_2/air at 80^{o}C) is 0.7 W/cm^2 at 0.68 V (58% energy conversion at 1.03 A/cm^2), corresponding to 0.85-1.1 g_{pt}/kW (0.59-0.77 mg_{Pt}/cm^2) (9). According to the DOE, market penetration will require platinum specific power density reduced to 0.2 g_{pt}/kW at >0.65 V (0.3 mg_{Pt}/cm^2)(10). It is envisioned that this decrease in platinum loading while maintaining sufficient performance will be achieved by increased Pt-utilization, lowering mass transport and ohmic losses, and increasing the inherent activity of the reaction zone by changing the nature of the conventional supported Pt electrocatalysts. Reduction in loading is being investigated via alloying, modification of the surface morphology, and extension of the reaction zone into the electrode. A thread common to each of these strategies is the manufacturing process used in the production of the catalyst and support.

1.3 Traditional low-platinum cathode manufacturing

1.3.1 Overview

A good overview of traditional fuel cell design and manufacturing techniques was published in the Journal of Power Sources in 2003 (11). Electrode fabrication falls into two distinct manufacturing methods: ex-situ electrocatalyst powder formation followed by ink formation and electrode manufacture or in-situ electrocatalyst formation, whereby the catalyst is formed

by the process and then directly impinged on a suitable substrate. The former technique requires two distinct steps with a concomitant price premium for catalyst manufacture. Powder formation is achieved either by more conventional solution precipitation/impregnation techniques or by newer spray-based methods such as spray pyrolysis and combustion chemical vapor deposition (CCVD). In-situ electrocatalyst formation involves forming either the supported, platinum/carbon (Pt/C), or unsupported catalyst directly onto either the proton exchange membrane (PEM) or gas diffusion layer (GDL). Common processing techniques that allow un-supported platinum deposition include physical vapor deposition (PVD), sputtering, chemical vapor deposition (CVD), combustion chemical vapor deposition (CCVD), reactive spray deposition technology (RSDT), and electrochemical deposition. The only known techniques that produce both supported and un-supported catalyst in one step are CCVD and RSDT.

Direct deposition techniques offer many advantages over bulk ink processing techniques by eliminating steps of impregnation, washing, drying, calcination and reduction. Most of the drawbacks of traditional synthesis such as redistribution of active sites during drying, surface poisoning during impregnation, and migration or agglomeration of particles during sintering are avoided.

Another promising avenue being explored is the ability to form electrodes that are thinner, 500 nm or less, than those traditionally available by screen-printing or traditional spraying methods. This is beneficial because a thin catalyst layer applied between the gas diffusion layer and electrolyte is in proximity to both the proton-conducting membrane and the incoming gas. At high cell current densities, gas permeability limits the effectiveness of thick electrode layers and this causes underutilized portions of the electrode and limits power density. Minimizing the electrode thickness, in this way, minimizes underutilized regions further away from the electrolyte (12). Modeling work at the NRC has shown that multi-objective optimization techniques can uncover Pareto optimal fronts and generate optimal design choices in catalyst layer development related to thickness and grading of electrode species (13, 14).

1.3.2 Direct and indirect techniques for low-platinum loading

Recently, Wee et al. performed a review of fabrication methods for low-Pt-loading electrocatalysts (15). Additionally, Saha et. al have discussed approaches for lowering platinum loading (16). These deposition techniques are shown in Table 1.

Table 1: Techniques and Institutions involved in low platinum loading electrodes

Technique & research institutions involved	Short description and variants	Pros & cons
Modified thin film – traditional printing	Decal transfer – catalyzed layer is cast onto a PTFE blank and then decaled onto a membrane CCM catalyst coated membrane – catalyst layer directly cast onto the electrolyte	Pros • Well established manufacturing technique • High volume manufacturing • Firmly explored in literature and modeling Cons • Controlling Pt particle size with Pt/C > 40% is difficult (loss of surface area) • Difficult uniformity of

Technique & research institutions involved	Short description and variants	Pros & cons
		deposition in large scale production • High cost due to several complex processes/steps • Limited by how thin electrode can be manufactured
Electrodeposition/pulsed electrodeposition *B. Popov – University of South Carolina(17)* *O. Antoine - Université de Genève(18)* *R. Durand - CNRS/ENSEEG(18)*	Platinum is electrodeposited onto a non-catalyzed carbon electrode in a commercial plating bath	<u>Pros</u> • Platinum is theoretically deposited at the most efficient contact zones for the ionic and electronic pathways of the substrate Pt/C wt. % to up 75%, without coarsening, near electrode surface, thereby achieving a 5 um thick catalyzed

Technique & research institutions involved	Short description and variants	Pros & cons
		layer with Pt preferentially near the electrolyte. <u>Cons</u> • Residual Cl^- ions from chloroplatinic acid may poison part of catalyst • Strongly diffusion limited by Pt-complex Concern over scalability
Sputter deposition – CCM and GDL substrates *A. Haug – University of South Carolina and UTC Power(19)* *R. O'Hayre - Stanford University Rapid Prototyping Laboratory(20)*	A vacuum evaporation process removes portions of a coating material and deposits a thin film onto an adjacent substrate Technique is well understood in integrated circuit manufacturing	<u>Pros</u> • Precise Pt content and thickness • wide range ot thickness available (<1nm to several microns) • Proven scalability

Technique & research institutions involved	Short description and variants	Pros & cons
P. Brault – CNRS Polytech Orleans(21)		• Cheap direct deposition method <u>Cons</u> • Performance falls behind conventional, ink based cells • Recognized poor durability • Poor adherence leading to greater probability of dissolution and sintering (22) – although this is disputed (23) • Smaller particle size of sputter deposited Pt hinders water management • Denser layers than traditional alternative evaporation methods

Technique & research institutions involved	Short description and variants	Pros & cons
Sputter deposition – organic whiskers *M.K. Debe – 3M(24)*	Thermal growth of a 'screw' dislocation non-conducting polymer pigment followed by platinum sputtering	Pros • High volume manufacturing • Good performance • Advanced stage of understanding Cons • Water management • High capital costs • Durability of electrodes
Dual ion beam assisted deposition *M. Saha – Northeastern University(16)* *A. Gulla – E-Tek(25)*	A combined physical vapor deposition (e-beam evaporation) and ion-beam bombardment process Direct metallization of GDL Low-density Pt deposits (mostly amorphous)	Pros • Thin layers of 25-75 nm thick • No need for support medium • Morphology can be controlled by ion-beam bombardment Cons • Requires vacuum

Technique & research institutions involved	Short description and variants	Pros & cons
Pulsed laser deposition *N. Cunningham - INRS-Énergie, Matériaux et Télécommunications(26)*	To date only performed on anode and no follow up work	<u>Cons</u> • Requires vacuum • No cathode performance data
Aerosol Assisted Deposition (AAD) *P. Haldar – College of Nanoscale Science and Engineering SUNY(27)*	Sonicate an aerosol of chloroplatinic acid and carry with argon to heated substrate in furnace	Pros • can grow a wide range of morphology from isolated islands of platinum to porous films • XPS shows no trace chlorine and well resolved metallic platinum peaks • Particle sizes range from 4-30 nm • Demonstrated on carbon nanotubes

Technique & research institutions involved	Short description and variants	Pros & cons
		Cons • Lab scale experiments only on 1” samples • No co-deposition option

1.3.3 Manufacturing process as a determinant of performance

The performance of an electrode depends on the physical characteristics of the final product, which in turn is affected by the processing techniques involved in manufacture (28),(29). The electrocatalytic activity of Pt/C catalysts is influenced by many factors, such as average particle size, relative crystallinity, presence of surface groups, surface morphology, and the nature of the platinum/carbon/ionomer interface. Therefore, when Pt/C catalysts are prepared using different methods or different brands of carbon support, many factors can influence their electrocatalytic activity and durability, leading to confusing results and erroneous conclusions(30). For example, research examining platinum particle size effects using Pt/C catalysts prepared by different methods, Attwood et al. found that the best average size of Pt particles in a Pt/C catalyst for methanol oxidation is approximately 3 nm (31). Frelink et al. indicate that the electrocatalytic activity of Pt/C catalysts for methanol oxidation decreases as the Pt particle size decreases in the range 4.5–1.2 nm (32). Takasu et al. came to a similar conclusion using a Pt catalyst supported on glassy carbon electrodes with Pt particle sizes from 7 to 2 nm (33). Watanabe et al. reported that no Pt particle size effect was observed when Pt/C catalysts with different sizes of Pt particles

on different carbon supports were prepared by the same method (34). Therefore, it is important to understand not only the physical attributes of the product but also the relative merits of each specific manufacturing technique and what processing factors may have net positive/negative impacts on the final product.

1.4 Open atmosphere thermal spraying

1.4.1 Overview

Thermal spraying techniques, which include plasma spraying, are common techniques used in the literature to produce films of SOFC electrode/electrolyte materials, but not for PEM type fuel cells. Plasma spraying usually involves passage of a solid powder to a DC or AC plasma, subsequent melting of the solid particles, and formation of splats of material on the substrate. The length of time in the plasma depends on the type of torch, gas flows and plasma shaping devices (i.e. cooling shrouds). Alternatively, lower energy technologies have been explored as possible alternate deposition techniques to plasma spraying. Worldwide research has led to the development of many similar techniques for open atmosphere lower energy flame depositions. These research developments include the Reactive spray deposition technology (RSDT) in Canada at the NRC-IFCI (35, 36), flame assisted vapor deposition (FAVD) in the UK at the Imperial College of London (37, 38), oxy-acetylene combustion assisted aerosol-chemical vapor deposition (OACAACD) in China at the University of Science and Technology of China (39) and combustion chemical vapor deposition (CCVD) in the United States at MicroCoating Technologies (40-42), Georgia Tech (43), and North Carolina State University (44). A doctoral thesis was also completed by Y. Liu at Georgia Tech examining the effects of CCVD processing parameters on nano-structured cathodes for SOFC applications (45). The different names are synonyms for a set of processes that involve pumping a dissolved metal-organic or metal-inorganic precursor through an atomizing nozzle and combusting the

atomized spray. Differences in the process occur by how atomization of the spray is accomplished and the method or direction of precursor introduction into the reactive zone. For instance, nozzles can atomize by ultrasonics, air shear, liquid pressure, and heat or a combination of energy inputs.

Precursor solutions containing dissolved metal-organic reactants required in the deposited film are generally pumped under pressure to the nozzle by use of a syringe or high-pressure liquid chromatography (HPLC) pump. In addition, some techniques feed the precursors to the nozzle as an aerosol and the nozzle is not used for atomization but rather for providing ignition energy to a flame. In yet another version of the technique, a dissolved liquefied gas is added to the precursor solution to aid in atomization through a technique known as supercritical fluid atomization. Regardless of the nozzle type, the atomized spray is then combusted by an ignition source such as a single pilot flame from a point source or a ring of pilots surrounding the exit of the nozzle. An optimal ignition point must be chosen, since igniting too close to the exit of the nozzle results in a fuel rich mixture that does not burn easily, while igniting too far away results in an oxidant rich mixture. Pilot gases consist of methane and oxygen or an oxy-acetylene type gas.

Depositions onto substrates usually occur by impinging the flame on the desired substrate and allowing the reaction to occur long enough for the desired thickness of film. If a nano-structured or dense film is desired, then the flame should penetrate the boundary layer of the substrate. Longer flames (i.e. distance from nozzle to substrate) and higher concentrations of precursor material favor nucleation of particles and agglomeration prior to the substrate rather than growth from the vapor phase directly on the substrate. This results in a powdery agglomeration of particles with poor adhesion. Care must be taken to prevent thermal shock to the substrate by controlling the heat up and cool down to deposition temperatures. This is generally done by heating the substrate from the back by resistive heaters or by another flame. Alternatively, the flame can be directed at a sheet of cooling air, water or a cooled metal surface for collection of powder particles instead of a growing film.

1.4.2 Open atmosphere flame based deposition systems

There is diversity of design in the systems developed separately around the world for open atmosphere flame spraying. Major differences include method of atomization, type of atomizer, solution injection geometry, and the fuel used in the flame. Xu and colleagues at NC State used a TQ-20-A2 Meinhard nebulizer for atomizing and a single point pilot flame for ignition of the atomized spray (46). In addition, a heating torch was applied to the back of the substrate holder to minimize the thermal gradient between the front and back of the substrate.

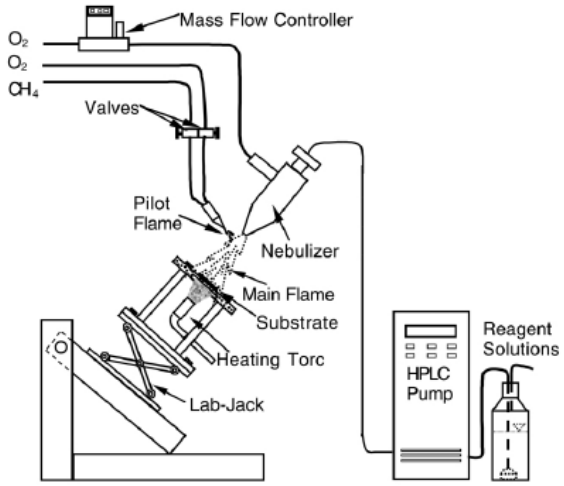

Figure 2: Experimental setup for liquid fuel combustion CCVD as reported by Xu et. Al (49) [© Surface and Coatings Technology, 2004, by permission]

Meng and researchers at the University of Science and Technology in China used a modified oxy-acetylene torch with a 2 mm diameter and fitted at an angle of 45^{o} to the substrate (39, 47-52). Precursors were supplied to the torch by means of an ultrasonic nebulizer injecting directly into the torch. The oxy-acetylene flame core reaches temperatures as high as 3000 C. Unlike other versions of this technology, the flame is not produced by the precursor solvent

but by an oxy-acetylene gas mixture. This process has been named oxy-acetylene combustion assisted aerosol-chemical vapor deposition (OACAACVD).

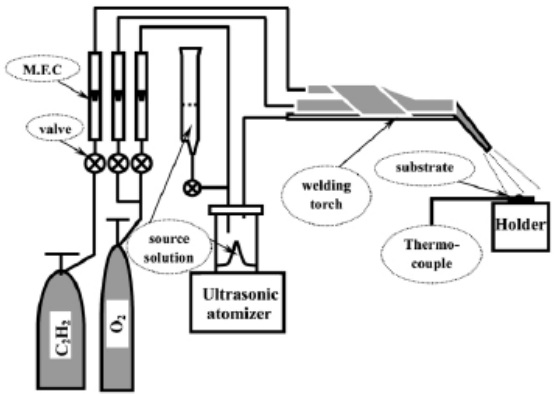

Figure 3: Diagram of oxy-acetylene combustion assisted aerosol-chemical vapor deposition as developed by Meng et al (56). [© Thin Solid Films, 2000, by permission]

Researchers at Georgia Tech and nGimat (formerly MicroCoating Technologies) are using the only known commercialized system for combustion chemical vapor deposition (42, 43, 53-55). The system consists of a proprietary spray/combustion nozzle, the Nanomiser®, that functions on pressure and heat input for formation of very small droplets that are then combusted by a ring of methane/oxygen pilot lights. The solution is delivered under pressure to the nozzle and heated prior to exit.

Steele and Choy at the Imperial College of London have been using a system of deposition named flame assisted vapor deposition (FAVD). The system was first reported in 1995 and work on SOFC cathode materials was published in 1997 (56-58). The process consists of an air atomizing nozzle and a separate flame. The air atomizer is directed at a substrate on a hotplate and a flame is arranged perpendicularly to the air atomizing spray jet. The atomized spray passes through the flame and onto the substrate.

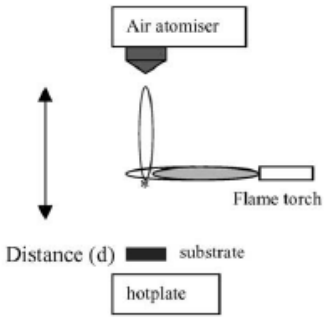

Figure 4: Diagram of flame assisted vapor deposition (FAVD) process as developed at the Imperial College of London (62). [© Journal of the European Ceramic Society, 2004, by permission]

Dr. Pratsinis developed flame Spray Pyrolysis at ETH in Switzerland. A variety of products have been synthesized by FSP, as for example, silica (59), bismuth oxide, ceria(60), zinc oxide, zinc oxide/silica composites, platinum/alumina. Figure 5 shows a 35 cm height HMDSO/EtOH spray flame producing 300 g/h of fumed silica using oxygen as dispersion gas. This material is called fumed silica because the traditional manufacturing process involves chemical gasification of silicon, oxidation of this gas to silicon dioxide, and thermal fusion of the resulting dust. The particles are collected in a baghouse filter unit.

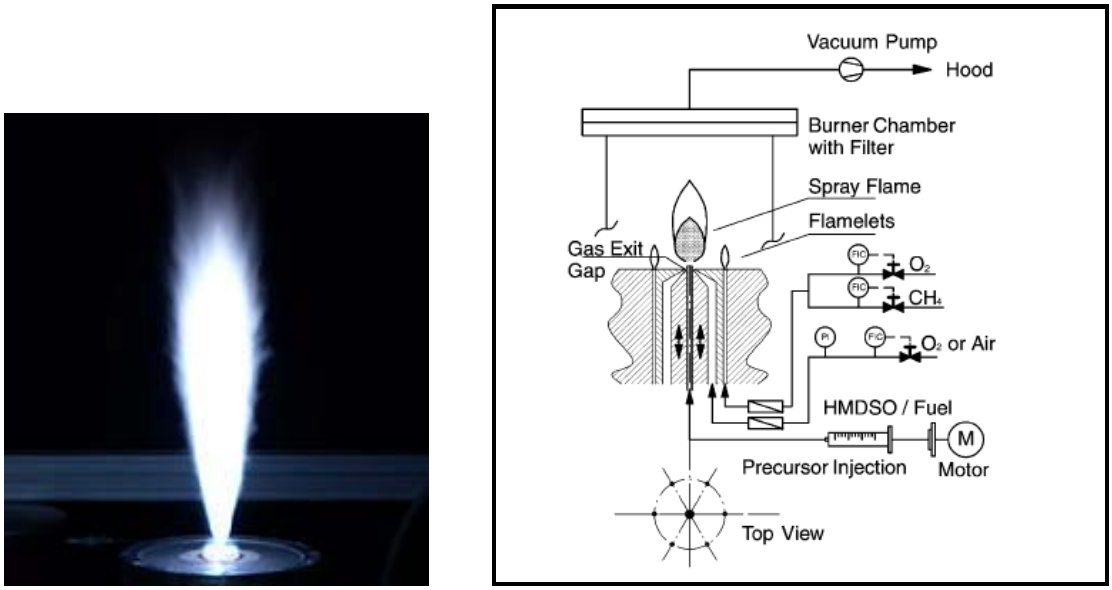

Figure 5: Flame Spray Pyrolysis (FSP) developed at ETH-Particle Technology Laboratory (61). [© Journal of Aerosol Science, 2002, by permission]

1.4.3 Flame processing process parameter identification

Examples of flame processing and parametric studies related to direct deposition of electrode materials for PEM electrodes are sparse. Therefore a review has been done of materials deposited by flame based processing for higher temperature direct deposition of SOFC components. Theoretical models describing combustion consider a double-film model for droplet combustion. In this model, an inner film separates the droplet surface from the flame front, and an outer one separates the flame front from the surrounding oxidizer (61). The rate of combustion and evaporation is dependant on the size of the generated droplet. As the droplet size decreases, the rate of evaporation of the droplet increases significantly. Therefore, generating smaller droplets in the atomizer can accelerate the combustion rate. The oxidant/fuel ratio results in different temperature profiles and determines the oxidative strength of the flame. It has been found that higher mixing ratios result in higher maximum temperatures in the flame and lower temperatures at a fixed point due to shortening of the flame length with increasing oxidant. Eventually, excess oxygen will serve to cool the

flame. The temperature profile of the flame will certainly affect the chemical reactions occurring and the ratio of products to reactants at a given distance from the nebulizer. Xu found that the YSZ (111) orientation was favored at oxygen flows of 2.0 L/min and 1.2 L/min but at intermediate flows of 1.6 L/min the YSZ (200) orientation was favored on single crystal MgO (100) substrates(62).

Substrate temperature is another important processing parameter that affects adsorption/desorption, reactivity and diffusivity on the substrate surface. According to the Movchan-Demchishin zone classification of thin film growth, there are three distinct morphological zones (63). These zones correspond to the ratio of substrate temperature to the melting point of the deposited film, in K (T/T_m). The three zones are zone I: (T/T_m) <0.3, zone II: 0.3<T/T_m<0.5, and zone III: 0.5< T/T_m<1. Zone I microstructure is characterized by low density tapered grains with domed tops. Zone II microstructure exhibits more columnar microstructures and the activation of surface diffusion. Zone III microstructure exhibits relatively large equiaxed grains and the activation of bulk diffusion. The model has since been refined to include a transition region (T_R) between zones I and II(64). Polly et. al studied the deposition of zinc oxide on amorphous quartz (65). They found that the nodular growth exhibited in zone I depositions was most likely due to localized shadowing of surrounding nodules. They further speculate that the deposition occurs preferentially at the tops of the tallest nodules and this depletes the reactants from the gas phase before reaching the underlying regions. This preferential growth means that atoms do not have sufficient mobility to move to a crystalline site and the films are amorphous. The transition from amorphous to crystalline depositions of zinc oxide on amorphous quartz occurred in the (T_R) region. It was further found that increasing the solution concentration from 2.5 mM to 40 mM shifted the transition temperature from $0.28T_m$ to $0.36\ T_m$.

1.4.4 Flame based processing for PEM manufacturing

Recent advances in aerosol and combustion science and engineering now allow scalable flame synthesis of mixed oxides, metal salts, and even pure metals in the form of nanoparticles and films with closely controlled characteristics. Flame processes are classified into vapor-fed and liquid-fed, depending on the phase of the metal precursor. Liquid-fed flame processes are distinguished by their flexibility in producing materials of various compositions and morphologies that result in unique product functionalities. The general principle behind flame synthesis of materials is the decomposition and oxidation of evaporated metal precursors in a flame, thereby forming stable gaseous metal or metal-oxide atoms followed by nucleation, aggregation/agglomeration and, to some extent, coalescence of aggregated nanoparticles. These flame-produced materials are in many cases attractive since they are formed directly in one step, and in the desired phase. For instance, in many wet-chemistry processing routes platinum catalyst is precipitated onto a carbon support and there is the need for a calcination step to obtain the desired crystal phase and to strengthen bonding. In contrast, the high temperature conditions in the flame allow platinum consolidation, bonding, and crystallization directly. Thus, flame synthesis is a flexible synthesis method where the product properties can be tuned by changing the composition of the precursor gas and the flame operating conditions. A quick quench-cooling of the product gas after a short residence time in the flame can to some extent control the specific surface area of particles. The main process variables are: flame peak-temperature, residence time at elevated temperature, and precursor loading/composition.

Large scale success stories of industrial manufacturing using flame based processing are best exemplified in the manufacture of titania and carbon black. Professor Pratsinis at ETH in Switzerland has produced many patents and papers in this area, but his work has been limited to flame processing in an enclosed chamber or fluidized bed for nanoparticle formation (66-69). In these processes, the product particles are collected on filters and packed for shipping.

However, flame processes can be applied directly to substrates to produce films with a single metallic phase or in conjunction with a secondary spray. In all cases, particles are formed once the volatile metal compounds are converted to stable metal oxide or metal nanoparticle in the high-temperature environment of the flame.

1.4.5 Reactive Spray Deposition Technology

The National Research Council of Canada's Institute for Fuel Cell Innovation (NRC-IFCI) has further developed the flame based deposition model and modified it for PEM fuel cell applications. Flame based PEM electrode direct deposition has only been pursued by a relatively small amount of researchers mostly through efforts at nGimat, formerly MicroCoating Technologies (70-73). The NRC-IFCI has also been active developing a proprietary version of the flame based deposition equipment, novel electrode compositions and improved processing methods for PEM cathode applications. The process developed at NRC-IFCI involves a thin-film catalyst layer directly deposited on an electrolyte membrane with a flame spraying process called the Reactive Spray Deposition Technology (RSDT). A formal patent for the equipment and processing methods is currently in prosecution (74). RSDT differs from CCVD in the method used to produce the heat necessary for atomization, the precursor solution storage and delivery, precursor solution formulation and equipment geometry. RSDT uses induction heating to elevate the temperature of the precursor liquid in the spray nozzle and components, which are commonly used in the supercritical HPLC (high performance liquid chromatography) and RESS (rapid expansion of supercritical spray) industries for storage and delivery of solutions. RSDT allows the possibility of actually passing a supercritical solution into an atomizer rather than having the atomizer take a solution to the supercritical point in the nozzle prior to exiting as a spray. The off the shelf components for RSDT allow extremely high injection pressures of up to 5,000 psi and temperatures up to 150

^{o}C to be reached prior to introduction into the nozzle. This expanded capacity allows the number of solvents and concentration of specific precursors used for solution preparation to be increased compared to only using the liquid state. A distinguishing feature of particle formation with supercritical fluids, versus using only liquid precursors, is the fast attainment of uniform conditions and of super-saturations in the carrier fluid, which favor the formation of small, monodisperse particles.

Previous incarnations of the RSDT process only allowed deposition onto substrates at temperatures greater than 500^{o}C or at very large distances between the flame and the substrate if temperature was a constraint. Method development at the NRC-IFCI has progressed to allow for direct catalyst coated membrane (CCM) depositions onto heat sensitive polymer electrolyte membranes. This has been accomplished by use of a quench gas incorporated into the flame zone of the process. The modified process also allows for introduction of carbon and Nafion® after the flame gasses have cooled to avoid thermal damage to the ionomer.

In flame synthesis, the residence time and temperature of the flame zone must be sufficient to transform the volatile precursors into metal particles and to reach the desired crystalline structure of particles formed by a collision/coalescence process. Further exposure to high temperature results in loss of valuable surface area by sintering, but this can be avoided using quench-cooling. After dissolving Pt precursors in appropriate solvents, a solution is sprayed through a nozzle to produce micron-sized droplets that burn out in a flame, resulting in metal atoms and/or metal oxide molecules in the gas phase. NGimat used a novel atomizing device, referred to as the Nanomiser®, because of its ability to produce an aerosol of controlled size down to the sub-micron range, from 0.002 to 4 L/min flow rates, without the need for any external atomizing gas(75). The ability to produce small-size droplets with narrow size distribution is of critical importance because precursor solutions are converted to an ultrafine mist that is then combusted into a vapor. The size of the aerosol influences the physical characteristics of the generated particles. In addition, the

process can be used without combustion of the aerosol, to spray polymers for oxygen barrier film applications or for powder formation(76, 77). Precursor preparation involves metal nitrates or metal organics (i.e., 2-ethylhexanoate or II,IV pentanetdionate), among others, that are dissolved in suitable solvents, which also act as a fuel for combustion. Water-soluble precursors may also be dissolved in water and then mixed with a miscible fuel and used in the process.

The nGimat method, referred to as NanoSpray^{SM} Combustion Processing, and the proprietary Nanomiser$^{®}$ were not used in this study due to patent protection and licensing restrictions(78). This nGimat method for platinum, carbon and ionomer deposition involves two Nanomiser® nozzles directed at 180^{o} to one another and parallel to a gas diffusion layer substrate. The setup is shown in Figure 6. The Nanomiser® nozzles generate platinum vapors which are quenched by a slurry stream introduced orthogonally to the substrate and Nanomiser® nozzles. The slurry consists of an isopropanol liquid base, Vulcan XC-72R carbon, and Nafion® ionomer(72).

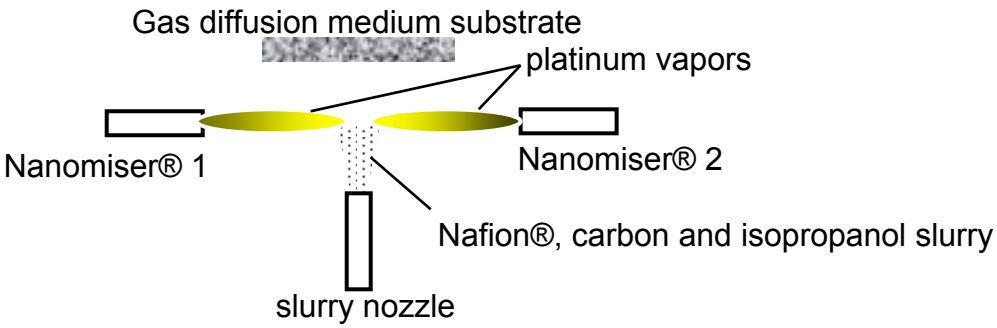

Figure 6: Microcoating Technologies, Inc. proton exchange fuel cell manufacturing technique (83).

The manufactured gas diffusion electrode is then pressed at an elevated temperature onto a suitable electrolyte for the final membrane electrode assembly.

1.5 Rational cathode design

1.5.1 Nafion content

High performance toward oxygen reduction requires good accessibility of reactant to the active sites of the cathode, fast interfacial electron transfer kinetics, fast electron transport through the hydrophobic carbon support, and proton transport through the hydrophilic Nafion-ionomer®. Electron transport resistance is normally negligible compared with proton transport resistance, so the limiting factors for oxygen reduction are the interfacial electron transfer kinetics, the oxygen mass transport resistances, and the proton transport resistance in the catalyst layer. If the Nafion® content is too low, there will be poor ionic conductivity and, conversely, too much Nafion® in the electrode will close the percolation path for the electron transfer between catalyst particles, resulting in worse electronic conduction and also hindering gas access to the reactive sites (79). It is believed that for a low amount of Nafion®, the electrolyte is preferentially located within the macro pores of the electrodes, and the ionic resistance decreases as the pores fill with Nafion® in a percolating network. Above a given threshold, due to the hydrophobic-hydrophilic properties of the Nafion structure, a further supply of electrolyte does not fill up the pores but forms films on the external surface of the electrodes, giving an additional contribution to the overall electrical resistance. Nafion will change the porosity, permeability, and hydrophobicity of the catalyst layer, and therefore, a proper balance of Nafion® is a necessary part of electrode optimization.

One of the most accepted models for the physical and electrochemical operation of the cathode is the so-called thin-film flooded agglomerate model. This model views the catalyzed carbon particles as flooded with electrolyte and forming agglomerates covered with a thin film of the electrolyte. The catalyst layer consists of a macro-micro porous interconnected hydrophobic region that

allows the reactant gas access to the surface of agglomerate regions, from where the reactant gas diffuses through the film to the catalyst where the redox reaction takes place (13).

Diagnostic criteria have been developed by Antolini et al. for measurement of electrode response in order to identify performance mechanisms, especially related to optimum Nafion® content in the electrode(79). In a comprehensive study using impedance spectroscopy and assuming a steady-state agglomeration model, his team was able to explain nicely the limitation mechanisms of polarization curves, taking into account Tafel kinetics, proton migration, and oxygen diffusion in electrodes with up to approximately 40 wt.% Nafion®. According to Gode, cathodes controlled by either Tafel kinetics and oxygen diffusion in the agglomerate regions or Tafel kinetics and proton transport in the catalyst layer result in a double Tafel slope, 120 mV/dec, at current densities >100 mA. If controlled by Tafel kinetics, oxygen diffusion, and proton transport together, a quadruple Tafel slope of 240 mV/dec will appear at current densities greater than 10 mA(80). It was further determined that the total current density considering Tafel kinetics and oxygen diffusion limitations was found to be proportional to the catalyst layer thickness and relatively insensitive to the humidity of the oxygen. However, the current density in regions dominated by Tafel kinetics and proton transport are found to be independent of the thickness and much more sensitive to humidity. He further concluded that the performance of cathodes with Nafion® content below 30 wt.% is limited by poor kinetics due to incomplete wetting of platinum by Nafion® and by limited proton migration and oxygen diffusion into the agglomerates. At medium Nafion® contents between 35-45% wt.%, the wetting of Pt by Nafion® is more or less complete and oxygen diffusion into the agglomerates is the mass-transport limitation. At large Nafion contents, > 45 wt.%, the overall porosity and average pore size decrease quickly. At this point, oxygen diffusion is limited not only in the agglomerates but also into the cathodes larger meso-pores as well, due to the decreasing percolation network of the pores.

In the same paper(80), Gode et al. experimentally performed gas and mercury porosimetry to examine different wt.% of Nafion® to examine the relation between pore size and pore volume. Gode confirmed a statistical maximum of the pore size at 50–100 nm. It increases from 65 to 100 nm when increasing the Nafion® content from 10 to 30 wt.%, and decreases back to 50 nm at 50 wt.%. The slight pore size increase corresponds to only a slight decrease in pore volume fraction in this region, as shown in Figure 7. Conversely, the pore volume decreases drastically from 30-50 wt.%. The increase of the pore size maximum indicates that the opening of the pores between the agglomerates is enlarged, even though the total porosity is slightly decreased, as shown in Figure 7. At higher Nafion loading (50 wt.%), the porosity has drastically decreased and the pore size maximum has become smaller (50 nm), leaving a cathode porosity of only 10% at Nafion contents above 70 wt.%(80).

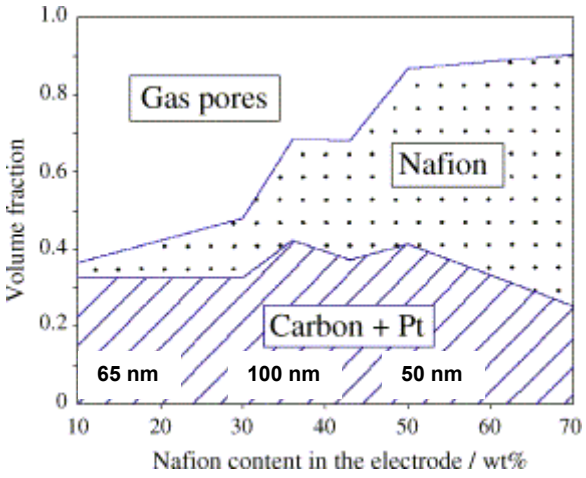

Figure 7: Volume fraction of gas pores, Nafion® and Pt/carbon as a function of Nafion® content in the electrode. Numbers above x-axis represent pore size (80). [© Electrochimica Acta, 2003, by permission]

Parallel work by Passalacqua et. al (79) reported on differences in the Tafel slope between 62-92 mV/dec depending on Nafion® loading but they did not analyze the change in slope at higher current densities as done by Gode et al. They attributed the different slopes to variations of the inter-phase conditions

and report that the influence of different rate determining steps for ORR is a function of Nafion® loading. A Tafel slope of 60 mV/dec has been explained by Srinivasan as a reaction pathway of oxygen reduction where the reaction involves an initial fast charge transfer step followed by a chemical step, which is rate limiting under Langmuir conditions (81). The Tafel slope assumes a higher value for low O_2 concentration, due to mixed activation/mass transport control; by increasing the O_2 concentration, the mass transport limitations are overcome. Li et al. found that the mechanism of oxygen reduction was not influenced by the Nafion® loading (82) and similar results by Passalacqua, contradicting his earlier work, were confirmed in a later paper (83).

Optimal Nafion® content has also been found to depend highly on the manufacturing technique. When Nafion is incorporated into the electrode by impregnation, the optimum value is lower than with techniques using mixing. This behavior is explained by the difficulty of the ionomer to reach the inner catalyst particles by impregnation. Above a certain amount, this fabrication technique tended to form a film of Nafion® and retard oxygen diffusion. Mixing the catalyst with polymer allows for a better distribution and penetration into the entire carbon/pore network. It was also found with the impregnation method that PTFE tended to coat the active sites and co-formulation with the Nafion®-ionomer required a lower optimum value(84).

Thin film and high dispersion techniques, which allocate platinum particles in a close proximity to the membrane surface to optimize the activity, are attractive avenues for electrode development. These techniques include electrospray, sputtering, and vapor deposition techniques. Using electrospray, Chaparro found that platinum particles land on the lowest resistance and most energetically favorable sites due to an applied voltage of several thousand volts(85). He used carbon monoxide (CO) stripping and found active areas of 101 m^2/g_{Pt} for electrospray using BEG as a solvent, but the others were in the 29-38 m^2/g_{Pt} range, indicating that the optimum Nafion® ionomer solutions containing both supported catalyst and Nafion® ionomer is highly dependant on the dispersion solvent. Work by Malek et. al. used molecular dynamics

simulations to perform a structural analysis of the microphase segregation occurring during the fabrication process of catalyst layers during ink formulation(86). Mesoscale simulations provided insights into the structural correlations and dynamic behavior of different phases in the catalyst layer composite. In these studies, they found that the solvent used in catalyst layer fabrication influences the evolution of stable agglomerated configurations.

Qi et al. experimented with Nafion® contents of 20-40% using Nafion® 112 membranes and 20 wt.% E-Tek catalysts applied to ELAT gas diffusion membranes (87) and found an optimum Nafion® content in the electrode of 30 wt.%, as seen in Figure 8 . For the electrodes prepared by Qi et al., an optimum of 30 wt.% Nafion® was found. However, the authors do not specify what platinum loading was used.

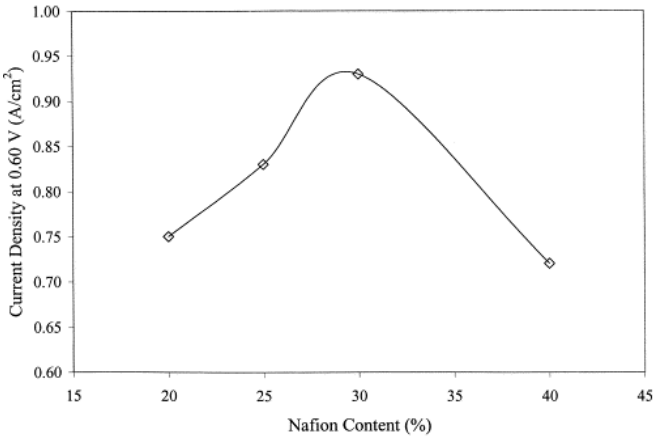

Figure 8: Effect of Nafion content in the catalyst layer on performance (E-Tek 20% Pt/C, 35/45/45 ^{o}C) (87). [© Journal of Power Sources, 2003, by permission]

Other researchers have found performances of ca. 1 A/cm^2 @ 0.7 V, 80 ^{o}C and 43.5 psi pressure without the need for hot-pressing on Nafion 112 (51 μm in thickness)(88). Their electrodes were 30 wt.% Nafion ® and 14 wt.% platinum and 56 wt.% (Pt/C = 20 wt.%). For loadings of 0.09 mg$_{Pt}$/cm^2 and 0.36 mg$_{Pt}$/cm^2, the porosity was measured as 84% and 77% (ratio of void volume to total), respectively. They report porosity values of 67% for air-brush spray techniques and 30% for GM's decal transfer technique. Tafel slopes were calculated as 72-

69 mV/dec, and are close to the theoretical value of 2.303 RT/F = 69.9 mV/dec at 80 ^{o}C.

1.5.2 Platinum optimization

Platinum has a face-centered cubic structure. Minimization of surface energy of individual crystallites is achieved in the cubo-octahedral structure. This structure has six cubic faces (100) and 8 octahedral faces (111). Structurally, there is a relationship between the size of the crystallized platinum particle and the number of platinum atoms exposed on the corresponding (111) and (100) faces. The cubo-octahedral structure also contains 36 edges and 24 corner sites.

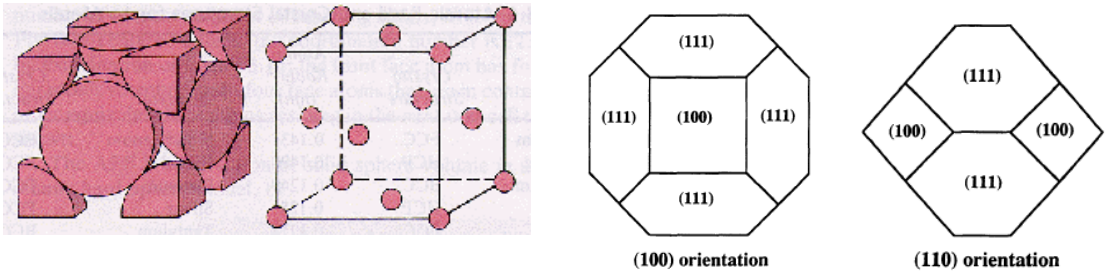

Figure 9: Face-centered cubic structure of platinum atoms and crystal of many platinum atoms into a particle(89). [© Journal of the Electrochemical Society, 1990, by permission]

Kinoshita was one of the early pioneers in determining particle size effects from contradicting data in the literature (89). He defined the platinum particle diameter by solving for the diameter of a sphere (d) whose volume is made up of the number of platinum atoms N(t) times the atomic volume of the platinum occupied in the unit cell, d_{at} (0.276 nm).

$$d = 1.11 d_{at} \sqrt[3]{N(t)} \qquad (2)$$

Figure 10 represents a view of the cubo-octahedral structure of a platinum particle with individual platinum atoms represented as spheres. It is easy to

envision the approximation of the entire crystal as a sphere when viewing Figure 10.

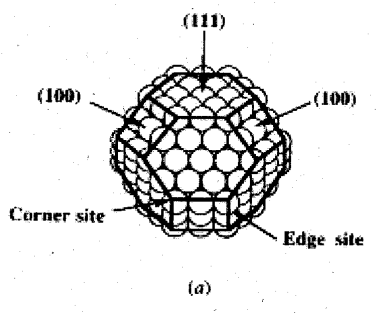

Figure 10: View of cubo-octahedral structure with platinum atoms represented as spheres(90). [© Wiley, 1992, by permission]

In order to simplify the calculations, Kinoshita further assumed that the cubic (100) and octahedral (111) faces contain the same number of edge atoms. With this assumption the atomic surface distribution on the faces and edges can be represented as shown in Figure 11.

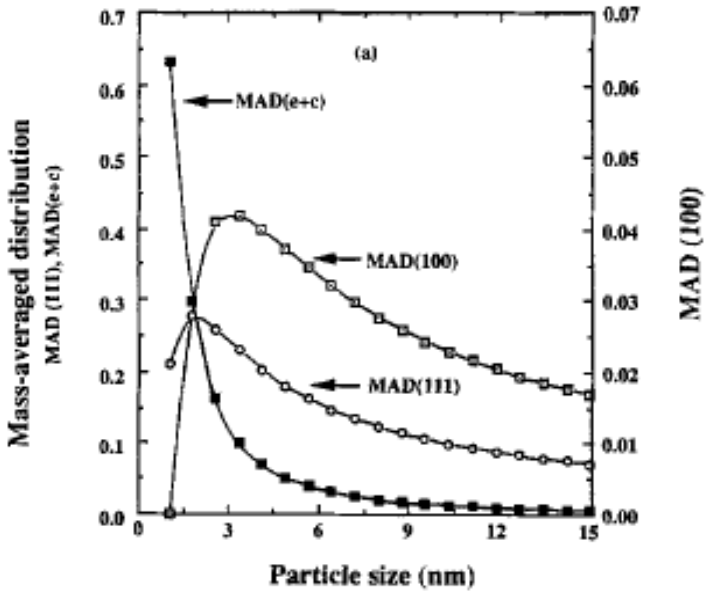

a)

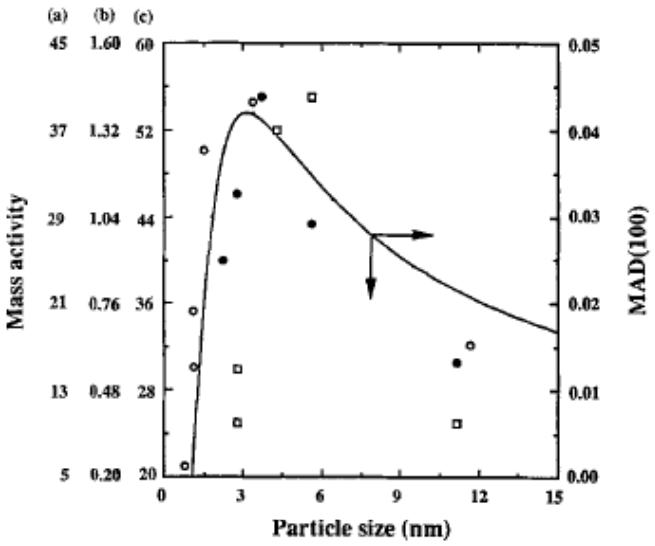

a) (●) 98% H_3PO_4, 180°C; (b) (○) 0.5M H_2SO_4, 25 °C and (c) (□) 97% H_3PO_4, 177 °C

b)

Figure 11: a) MAD (mass averaged distribution) of platinum atoms on the (111), (100) crystal faces and the sum of the edge plus corner (e + c) sites b) Superimposed plots for Mass activity toward oxygen reduction and MAD (100) (represented as a solid line) as a function of particle size in different acidic environments (102). [© Journal of the Electrochemical Society, 1990, by permission]

The distributions of surface platinum atoms for a given plane can be normalized according to the number of atoms occupying the entire surface. This is called the surface area distribution (SAD). Figure 11 shows that the octahedral (111) face has a mass averaged distribution (MAD) maximum at around 2 nm (28%) while the cubic (100) face has a mass averaged maximum at approximately 3.5 nm (4.2%).

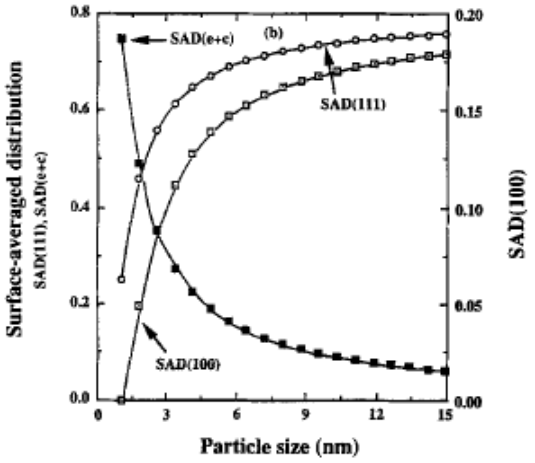

Figure 12: SAD (surface averaged distribution) of platinum atoms on the (111), (100) crystal faces and the sum of the edge plus corner (e + c) sites (102). [© Journal of the Electrochemical Society, 1990, by permission]

The proportion of edge and corner sites decreases rapidly as the size increases; in fact the edge and corner sites represent 65% of the total mass at approximately 1 nm in size, and for particles of 3 nm they are at approximately 10%. The distributions are quite different for the surface averaged distribution. Due to the fact that the surface area distributions are normalized to the total number of platinum particles on the surface and not to the total number of platinum particles within the volume, the distributions do not exhibit a maximum but rather rise to a limiting value.

The octahedral (111) atoms occupy most of the available surface area, and their proportion rises, from approximately 25% at 1 nm to roughly 70% at 6 nm. The cubic (100) faces rise in proportion from a value of near zero at 1.5 nm to 15% at 6 nm. The edge and corner sites again rapidly fall off but in this case the drop is less drastic. The surface area distribution of the edge and corner sites goes from roughly 75% at 1 nm to approximately 18% at 6 nm.

There are two ways of expressing catalytic activity. Activity can be expressed as mass activity, current per mass of catalyst, and specific activity, which is activity per unit surface area of catalyst. The mass activity of a surface in an electrochemical reaction is expressed in (A/g_{pt}). The current is normalized to

the mass of catalyst. This is especially important due to the high cost of the catalyst. The literature shows that there is disagreement between the electrocatalytic activity between single-crystal platinum surfaces and the corresponding crystal faces associated with supported platinum particles, suggesting that ideal surfaces may not be directly applicable to understanding electrocatalysis on small particles. Kinoshita collected mass activity versus particle size data from other researchers and superimposed the corresponding mass activity with the mass averaged distribution of the (100) face of the cubo-octahedral structure, as shown in Figure 11 b. The peak in mass activity data occurs between 3.5 and 5.5nm. This is in agreement with a maximum in MAD(100) at 3.5 nm. It should be noted that particle size is a somewhat simplistic treatment of the situation because in reality there is a distribution of sizes and the purely geometric treatment considers size without correspondingly accounting for the possibility of distributions. This may somewhat be rationalized by the generalization that small diameters in the nanometer range are known to contain much narrower distributions than those of larger particles.

A similar treatment of the surface area distribution of the cubic (100) plane versus the total surface area and the specific activity shows an increase in activity with increasing exposed (100) surface, as shown in Figure 13.

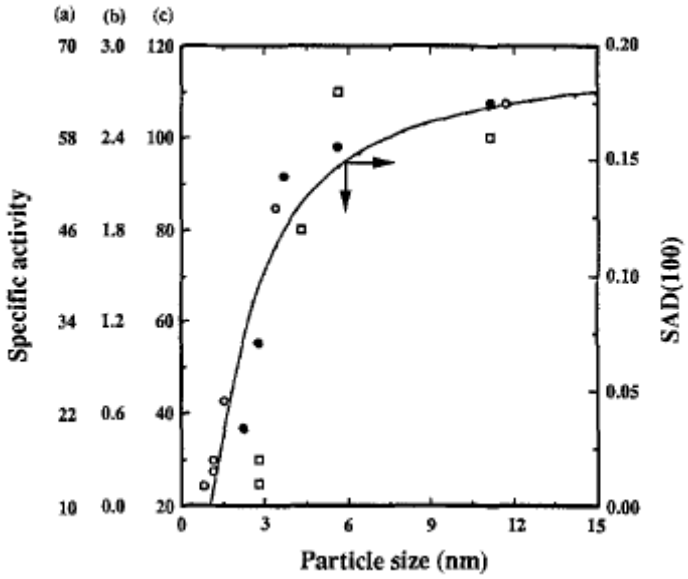

a) (●) 98% H_3PO_4, 180°C; (b) (○) 0.5M H_2SO_4, 25 °C and (c) (□) 97% H_3PO_4, 177 °C

Figure 13: Superimposed plots for Surface activity toward oxygen reduction and SAD (100) (represented as a solid line) as a function of particle size in different acidic environments (102). [© Journal of the Electrochemical Society, 1990, by permission]

The specific activity then reaches a limiting value, as does the surface area distribution. The close agreement in the trend of specific activity and SAD(100) suggests that oxygen reduction on platinum particles is a structure sensitive reaction. Similar treatments of the SAD(111) and MAD(111) show particle size dependence. It is worth noting that the MAD(111) is almost 7 times larger than the corresponding value for MAD(100) due to geometrical considerations. Therefore it is necessary to consider the contribution of the (111) face to the overall oxygen reduction rate.

Oxygen reduction on platinum surfaces is a structure-sensitive electrocatalytic reaction with a multi-electron transfer process that involves several steps in its reaction mechanism and the possible existence of several adsorption intermediates(91). Several mechanisms for the oxygen reduction reaction have been proposed in the literature. One proposed mechanism

involves simultaneous adsorption of the two oxygen atoms on two adjacent surface sites of the electrocatalyst. This type of interaction requires a dual site for dissociation of oxygen to occur. The (100) and (111) planes allow the oxygen molecules to approach laterally, whereas the edge and corner sites are not as favorable geometrically to allow this type of reaction pathway. Based on these arguments it is important to have a well-defined particle size. Particles that are too small will have a large portion of edge and corner sites that interfere with the oxygen reduction reaction while particles that are too large lead to underutilization of platinum and increased cost.

Determination of the Pt catalyst surface area $A_{Pt,\ cat}$ (also known as ECA – electrochemical area) can be performed ex-situ by cyclic voltammetry (CV)(92). The adsorption (cathodic current) and desorption (anodic current) peaks of hydrogen are integrated to obtain the total current between the rise from the capacitive double layer to vertex potential. Determination of the exact cut-off value for integration makes determination of the surface area somewhat difficult. CO stripping voltammetry can be carried out to determine the cathode surface area, and is technically a better method to use, since the peak onset is unambiguous and the shape of the CO molecule resembles the shape of oxygen. Figure 14 shows the result of an *ex-situ* cyclic voltammetry experiment of an electrode made with the Nafion®-ionomer component incorporated as a final processing step to a preformed electrode which contained carbon supported catalyst and polytetrafluoroethylene (PTFE) binder.

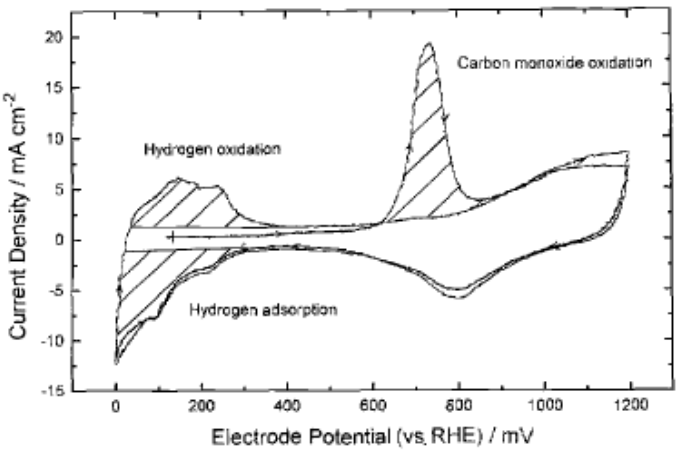

Figure 14: Ex situ cyclic voltammogram of a cathode in 1.0 mol/dm^3 H2SO4 at 25^{o}C, recorded at a potential sweep rate of 30 mV/s. The forward potential scan from +0.125 V (vs. RHE) shows the CO oxidation peak. The reverse potential scan from +1.2 V (vs. RHE), and the subsequent potential cycles, show the hydrogen adsorption and hydrogen oxidation currents (103). [© Journal of the Electrochemical Society, 1997, by permission]

Catalyst surface area, ($A_{pt,\ cathode}$) is reported in units of m^2/g_{Pt} and ranges from 35 m^2/g_{Pt} for 40% Pt/C (using E-TEK supported catalysts) to 86 m^2/g_{Pt} for 46% Pt/C (using Tanaka supported catalysts). A comparison of the $H_{2,\ abs}/H_{2,\ des}$ Pt-surface area by CV determined in-situ on an MEA electrode ($A_{Pt,\ MEA}$) tends to show lower active areas. The ratio of $A_{pt,\ cathode}$ /$A_{Pt,\ MEA}$ is referred to as MEA catalyst utilization, u_{Pt} and is a useful guide to determining optimum ionomer quantities in the electrode. Minimization to reduce covered/isolated platinum sites must be balanced with proton conductivity in the electrode. It should be noted that the term utilization is used differently throughout the discipline. An alternate definition of utilization is the electrochemically active surface area, determined by in-situ CV of the Pt catalyst, divided by the total surface area of the catalyst. Total surface area data can be determined from the catalyst manufacturer. In order to increase the mass specific power density the various loss terms must be determined and their impacts isolated. Losses occur from the following mechanisms:

1. sluggish ORR kinetics

2. ohmic losses
    a. electronic contact resistances between the flow field and diffusion media
    b. proton movement through the membrane
3. mass-transport-losses from poor oxygen transport through the diffusion media and electrode layer

Activities listed in the literature are often different under nominally identical conditions. Therefore Gasteiger et al. (9) have proposed thin film rotating disk electrode (TF-RDE) and MEA testing in O_2/H_2 cells as methodologies to determine mass activity (A/mg_{pt}) and specific activity (A/cm^2_{Pt}). In their study, CCMs of 50 cm^2 were made with carbon/ionomer ratios as shown in Table 2.

General Motors	***Pt loading Anode/cathode mg/cm²***	***Pt/C wt. ratio***	***Wt. % Nafion***	***Pt wt. ratio g_{Pt} / $g_{electrode}$***	***C wt. ratio g_C / $g_{electrode}$***
47% Pt/C (TKK)	0.4/0.4	0.47	35.2	0.20915	0.445
46% Pt/C (TKK)	0.5/0.51	0.46	35.4	0.207	0.45
20% Pt/Vu (ETEK)	0.15/0.17	0.2	45.5	0.091	0.455
40% Pt/Vu (ETEK)	0.37/0.38	0.4	41.7	0.17	0.425

TKK – Tanaka supported catalyst

ETEK – E-TEK supported catalyst

Table 2: Representative component weight ratios for determination of activity benchmarks (9).

The activity measurements were determined in pure oxygen to minimize mass-transport resistances. This is a necessary condition for determining mass activity. It is possible to determine if there are minimal mass-transport resistances if near theoretical Tafel slopes (70 mV/decade @ 80 C) as well as high Pt-utilization (>80%) in the MEA are present. The authors point out, however, that pure kinetically controlled H_2/O_2 polarization curves are not always obtained with non-optimized MEAs and diffusion media. In this case the mass-transport induced losses cannot be quantified, and determination of Pt catalyst activities is unreliable. According to Gasteiger:

1. The highest Pt surface area for the >40% Pt/C catalysts is ~85-90 m^2/g_{pt}
2. Specific activities indicate a negligible particle size affect in the region 2-4 nm
3. The highest mass activity is obtained for the catalyst with the highest Pt surface area

If mass-transport losses do not increase as Pt-loading is reduced then the effect of reduction in Pt-loading on an electrode has been proposed to be:

$$\left.\frac{\partial E}{\partial \log\left[L_{ca}\right]}\right|_{pO_2, pH_2, T} = -b \tag{3}$$

In (3), L_{ca} is the cathode platinum loading and b is the Tafel slope. This equation means that the change in cell voltage with the logarithm of the cathode Pt-loading is proportional to the Tafel slope. Therefore for a Tafel slope of 70 mV/decade at 80^{o}C, a loading reduction by a factor of 2 to 4 results in a predicted voltage loss across the entire current density range of 20-40 mV.

By analysis of the voltage loss terms for the electrodes discussed by Gasteiger et al., it was determined that a significant increase in performance could be achieved by reducing the mass-transport-induced voltage losses at high current densities. Reducing the mass-transport-induced voltage losses combined with a reduction of loadings to 0.05/0.1 mg_{pt} /cm^2 (anode/cathode) would result in power densities of 0.7 W/cm^2 at < 0.2 g_{pt}/kW while meeting the requirement for energy conversion efficiency. However, at low to medium power densities, improved cathodes with ~ 4 fold higher activity compared to Pt/C are required.

Qi et al. (87) investigated power curve performance at different platinum loadings using Pt/C ratios of 20 and 40%. For the 20 wt.% Pt/C catalyst, large increases were observed when the loading was increased from 0.022 to 0.083 mg/cm2. After 0.083 mg/cm^2, the change became much less pronounced, and a best performance was achieved at a loading of 0.138–0.253 mg/cm^2. Similarly, large increases were observed when the loading was increased from 0.074 to 0.217 mg/cm^2. After 0.217 mg/cm^2, the change became gradual, and the best

performance seemed to be reached at a loading of 0.306–0.387 mg/cm^2. A higher Pt loading is needed to achieve the best performance than when 20% Pt/C is used, because the Pt particle size of the 49 wt.% is almost twice as large as that of the latter (3.9 nm versus 2.0 nm).

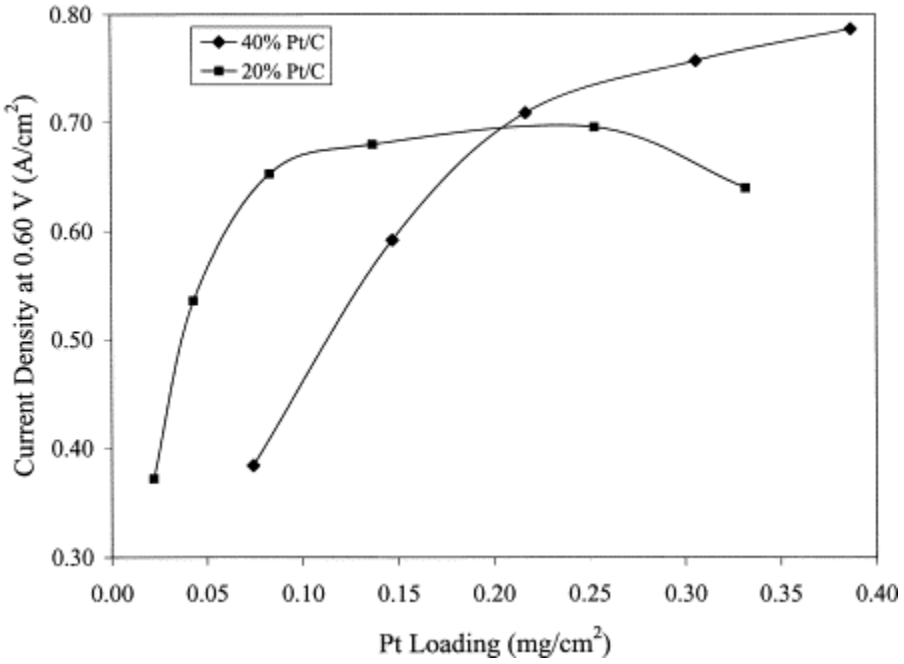

Figure 15: Effect of platinum loading on Nafion® 112 membranes using 20 wt.% and 40 wt.% E-Tek catalysts (87). [© Journal of the Power Sources, 2003, by permission]

Questions remain as to how much of a role the morphology of the platinum particles plays in determining the performance of the cathode, as shown in Figure 15. Qi et. al attribute this to the larger platinum particle size of the 40% Pt/C particles versus the 20% Pt/C, but it is unknown how the morphology of the deposited platinum, from different processes, plays into the shifting of this curve to lower loadings for a given performance.

1.5.3 Ultra-thin layers and compositional grading

The complexity of the concomitant physical phenomena that take place in a fuel cell electrode make models and simulations of the system very difficult to formulate and validate. Unlike better-established areas such as solid and fluid mechanics, there is still disagreement on the details of the electrochemical and transport mechanisms that result in the conversion of energy by combining hydrogen and oxygen. The reason for this disagreement resides, at least partially, in the non-trivial extension of the results from traditional electrochemistry (e.g. kinetics of rotating disk electrodes) to the much more complex multi-phase porous electrodes that constitute the fuel cell. In addition, the different structural components of fuel cell electrodes contribute to the overall cell performance in a very convoluted way, and it is very difficult to assess their individual effects because it is not possible to control the structure of each phase individually. RSDT is a fabrication tool that could be very useful for this kind of assessment, because of the independent control that the technique provides over the deposition of individual electrode constituents. One clear advantage that this capability provides is that these constituents may be graded following an optimization strategy, as reported by earlier work at the National Research Council, although this benefit may be increasingly marginal as the thickness of the electrode is diminished (93).

Carbon support and ionomer content greatly influence PEMFC behavior. Their role is to provide a percolating electrical network for the conduction of electrons and protons. Nonetheless, they are also the cause of technical problems still unresolved. One clear example is carbon corrosion, a degradation phenomenon that is especially promoted by near-OCV conditions (94). This issue is currently driving research efforts towards non-carbon supports such as indium tin oxide (95) or titanium nitrides/carbides (96), as well as unsupported platinum only electrodes (97). Ionomer in the catalyst layer is added as a compromise between adequate ionic conductivity and gas porosity. The influence of ionic conductivity on performance has also been the scope of research activity

(98). In common with the former case, there is also interest in developing ionomer-free electrodes, paving the way towards the use of very thin (< 1 micron) catalyst layers. Such catalyst layers are called ultrathin catalyst layers.

Although the benefits of reducing the catalyst layer thickness down to the submicron range are clear, the understanding of the underlying physics in very thin electrodes is limited. Transport phenomena in very thin catalyst coated layers (CCLs), for example, are likely different from their micron-range counterparts. The very low thickness results in a very large volumetric water production, implying that the CCL works virtually always in a flooded state. Consequently, the mechanism for proton transport, traditionally assumed to follow Ohm's law in the ionomer, is now believed to occur in liquid water due to the competitive interaction between concentration and electrostatic potential gradients, and is possible because of the very low thickness of the CCL. Since water cannot provide counter-ions for charge equilibration (like Nafion's SO^{-3} groups) electro-neutrality cannot be rationalized. This transport mode is known as Nernst-Plank transport without electro-neutrality.

Numerical simulation of such systems is relatively new, and IFCI's Modeling Group has pioneered the modeling work in this area (99), successfully reproducing experimental results from 3M. Unfortunately, the availability of experimental results in the open literature is scarce. The interdependence among cell fabrication, microstructure and performance is poorly understood within the fuel cell community. This lack of understanding and the lack of manufacturing options offering independent control of structure and thicknesses offers a unique opportunity for novel electrode manufacturing processes like RSDT. The RSDT process can be used to examine traditionally unattainable structures and physical electrode properties. The RSDT process can produce microstructural morphologies ranging from dense metallic films and dendrite fingers to island-clustered growth. This deposition flexibility coupled with the ability to produce an electrode thickness governed only by deposition time and further regulated by a precisely controlled catalyst flux allows for novelty in both thickness and morphology. While some researchers claim that the performance limit of random

electrode structures has been reached(100, 101), others think that there are still opportunities for improvement with a better understanding of the impact of microstructure on effective transport properties and performance(86, 102).

With the RSDT process, catalyst, ionomer and carbon composition are decoupled and independently controlled during the manufacturing process. This capability allows for several higher-level architectural designs to be examined with one process. Traditionally, a carbon-supported platinum ink mixed with a proton-conducting ionomer, Nafion®, is sprayed on a suitable electrolyte or porous gas diffusion medium. With this traditional approach, carbon/platinum ratios are fixed by the ink composition at the start of the process. Unfortunately, the traditionally available manufacturing processes only allow for either an unsupported catalyst deposition (i.e. platinum sputtering) or an ink-based process where the catalyst composition is predetermined and is already attached to a support. There is no process that allows for both types of approaches to be combined in a single process. RSDT allows for two types of separate deposition modes, supported and unsupported catalyst deposition. Some of the possible electrode architectures are platinum un-supported catalysts with microstructures such as dense films, island clustered growth and dendrite structures. Random phase ternary composites are also possible utilizing carbon, Nafion®, and platinum. Additionally, combinations of composite and catalyst only can be manufactured. Further flexibility in achieving a desired electrode thickness is factored in when considering that the growth rate can be intentionally set to be sufficiently small enough so that ultra-thin layers can be created. This is achieved by limiting the number of passes the substrate is subjected to in each experiment.

Minnesota Mining and Manufacturing (3M) is currently the leader in structured ultra thin-film platinum and alloy catalysts deposited by vacuum coating onto electrically inert whiskers (24, 103). The whiskers are grown from the organic pigment N,N-di(3,5-xylyl)perylene-3,4:9,10bis(dicarboximide) referred to as PR149. Vacuum sublimation is used to form thin films of PR149. The PR149 vacuum deposited thin films convert by heating in vacuum a monolayer

film of oriented crystalline whiskers by a screw dislocation growth process. A crystalline whisker's morphology is determined by the ratios of surface free energy of its side planes (Wulff's Theorem). The grown whiskers are then coated with platinum by a vacuum coating process. The whiskers are then compressed in the MEA manufacturing process to a thickness of ~200 nm. The vacuum physical vapor deposition process has been scaled by 3M and exists in large manufacturing capacity for applications related to glass tinting. A good example of the extent their technology has been developed in terms of manufacturability and scalability is evident at their Menomonie plant in Wisconsin(104).

Gasteiger et al. at General Motors conclude that diffusion limitations can be addressed by reduction in thickness of the catalyst layer, and this can be accomplished by switching to higher platinum loadings(105). Traditional processing techniques using ink based tape casting, ink spraying or screen printing are limited in the minimum thickness (with uniformity) attainable and therefore new processing techniques such as RSDT show promise in the area of novel thin electrode development.

1.5.4 Support free electrodes

Much research has been done in recent years on support free electrodes using only platinum. Due to cost constraints this type of electrode must necessarily be thin and yet effective at balancing the mass transport needs of the electrode. Cell performance in the literature has been quite poor but manufacturing has been mostly limited to vacuum based sputtering techniques. Sputtering has been performed onto gas diffusion based electrodes and then these catalyzed electrodes are pressed into the electrolyte layer (21, 97, 106-108). Alternatively the catalyst has been applied directly to the electrolyte layer(19, 20).

1.6 Literature review summary

Societal problems related to both the production and use of energy are poised to represent a significant challenge to humanity over the next several decades. Climate change threatens to quickly destabilize many of the ecosystems that have adapted to a relatively stable state in the history of the Earth's climate. Simultaneously, the economic concerns of society and the need for stable governance require continuous growth in economic output. That growth, at least in the current incarnation of the economic system, is invariably linked to the consumption of ever increasing amounts of energy and the throughput of material goods. The chances for long term prosperity and human health will largely be determined by how those two competing needs are reconciled. Coupled to this predicament is the uncertainty in supply linked to depletion of traditional petroleum resources and society's overreliance on this one source of energy for over 95% of its transportation needs.

One thing seems clear and that is that a multi-faceted approach to diversification of supply, more efficient uses of existing supplies and innovative ways to store excess electrical capacity from renewables are crucial to any energy system of the future. While there is no one techno-fix "answer" to these complex issues there are pieces to the puzzle. Proton exchange fuel cells offer the potential to provide zero emissions at the point of use and coupled to electrolysis fueled by excess capacity generated by wind and solar offer, the potential to offset some of the current need for a convenient transportable energy vector.

Proton exchange fuel cell commercialization is stymied from penetration into the market by both cost and durability. The majority of the cost associated with the fuel cell is the platinum catalyst used in converting oxygen and hydrogen to water and electricity. The electrodes that house the catalyst account for over 50% of the cost of the cell. The past four years have seen the prices of platinum, and commodities in general, increase from $400 USD per troy ounce to in excess of $2200 USD per troy ounce. The recent troubles in the credit markets and the

specter of a slowdown in the international economy has seen those prices plummet, and platinum was recently trading less than $1150 USD per troy ounce. In order to meet the targets set out by the Department of Energy for transportation applications, market penetration will require platinum specific power density reduced to 0.2 g_{pt}/kW at >0.65 V (0.3 mg_{Pt}/cm^2) total loading for both the cathode and anode.

Platinum particle size, effective catalyst placement in the electrode and resistance to agglomeration under OCV conditions is crucial to address cost effectiveness and durability of next generation electrodes. A particle size of 3-5 nm is optimal with smaller particles interfering with the rate of the structure sensitive reaction due to the edge and corner effects of the cubo-octahedral shape of the particle. Particles larger than 5 nm suffer from ineffective use of platinum atoms not located on the surface and thus represent underutilization of the expensive catalyst. Current manufacturing techniques suffer from the unwanted growth in platinum particle size with increased weight percent on the support. An optimum balance must be struck between the need for a percolating network of Nafion® for proton transport and pores for gas and water transport. The method of electrode manufacture appears to have a large impact on where this balance is struck but the optimum appears to be near 30 wt.% Nafion® in the electrode. The platinum loading must be reduced while still providing an acceptable level of performance. The platinum particle size effects of this relationship are understood. Less understood is the optimal positioning of the platinum in the electrode layer, catalyst grading and catalyst microstructure on this relationship. A clear thread toward thinner electrode thickness is evident in the literature. Development of reduced thickness electrodes requires higher weight percent catalyst on carbon supports. Unfortunately, existing manufacturing techniques encourage platinum particle coarsening as the weight percent moves from 20 wt.% to 40 wt. % and higher(109). This manufacturing gap is one area that can be addressed by Reactive Spray Deposition Technology.

New manufacturing techniques that offer independent and real-time control of composition and morphology while offering simultaneous support free and supported catalyst architecture are exciting avenues for fuel cell development. The move to thinner layers and optimized placement of catalyst in the layer where it is most active render many traditional processing techniques inadequate or lacking. This is especially true as electrode layers become increasingly thinner and uniformity becomes problematic. Reactive Spray Deposition Technology (RSDT) offers the possibility of addressing many of the manufacturing issues stated in a continuous process that is amenable to roll-to-roll direct catalyst coated membrane (CCM) processing. This method of open atmosphere combustion deposition has been reported sparsely in the literature for ceramic and cermet oxides but aside from industrial work done by Microcoating Technologies, as Combustion Chemical Vapor Deposition (CCVD), and a few preceeding summaries, this technique remains underdeveloped in the peer reviewed literature. Knowledge gaps clearly exist in determination of optimal processing parameters, microstructural characterization, surface characterization, and cell testing to begin vetting the full potential of this technique for polymer electrolyte membrane catalyst development.

2 Reactive spray deposition system description and experimental setup

The open atmosphere flame based deposition system used in this project is a novel deposition system fabricated at the National Research Council Institute for Fuel Cell Innovation (Vancouver, BC). In its most basic embodiment the system consists of a reservoir for holding a liquid, a pumping mechanism, a combustion nozzle to provide atomization of said liquid and a means of combustion for the atomized spray. The combusted spray is then directed at a substrate for deposition of a film or directed at a collection means such as an electrostatic precipitator or filter for powder collection.

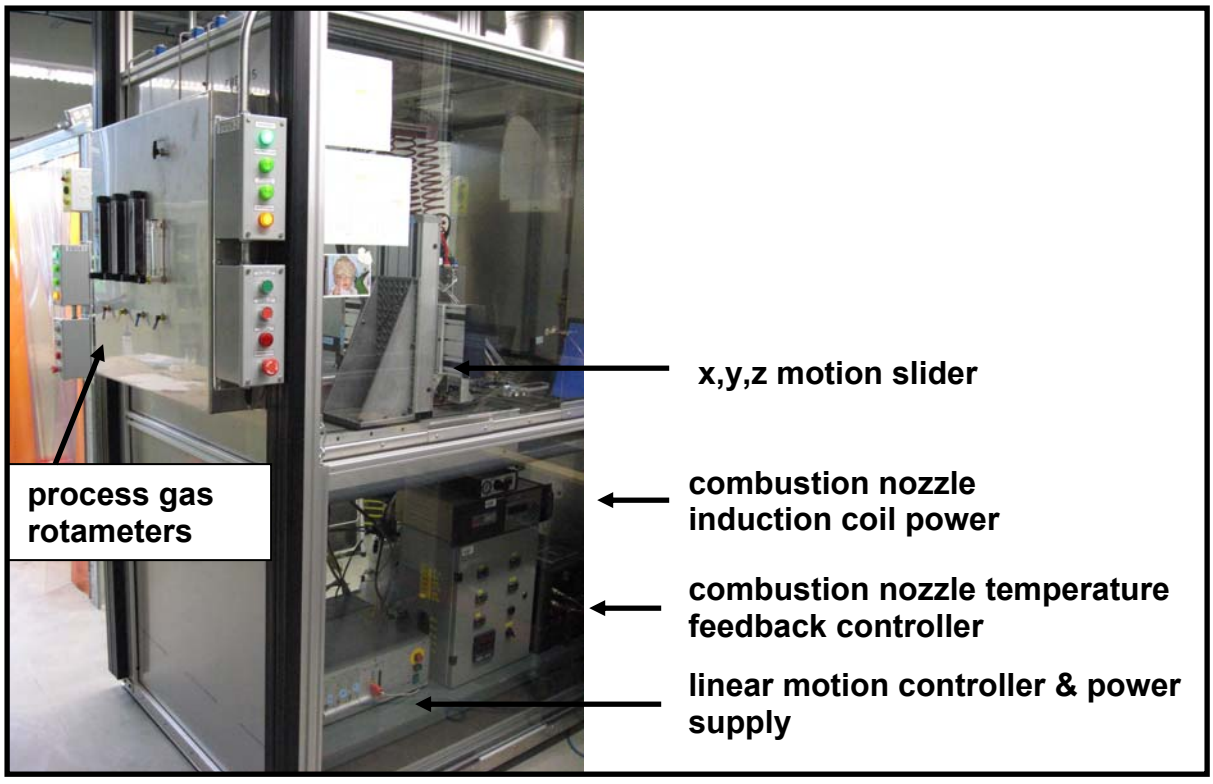

Figure 16: RSDT hood enclosure and peripheral controls

The pumping equipment used in this work consists of a Teledyne Isco 500D syringe pump (Teledyne Isco, Inc., Lincoln, NE). The precursor solutions are contained in a modified sanitary sight glass Tee assembly available from Rodger Industries (Blenheim, Ontario), herein referred to as a pressure vessel.

Figure 17: A) Precursor pressure vessel B) Isco 500D syringe pump, backside of gas panel rotameters and HPLC pump for cleaning

Two viewing ports and two cap plates were also added. The top cap plate contains two ports, one for filling and the other for discharging a liquefied gas such as propane. Liquefied gas, in this thesis, refers to a substance that is gas at room temperature and pressure but liquefies with applied pressures of less than 300 psi at room temperature. One port contains a drilled-through fitting in which a length of tubing acting as a dipstick is inserted to the very bottom of the pressure vessel. The other port consists of a two-way valve for venting the liquefied gas. This vessel is used to contain precursor solutions. The solutions are made by dissolving platinum II, IV pentanedionate into an appropriate solvent and then

capping the vessel. The chemical structure of platinum II, IV pentanedionate (commonly called platinum acetylacetonate) is shown in Figure 18.

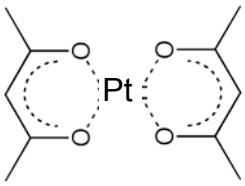

Figure 18: Chemical structure of platinum II, IV pentanedionate

Once the vessel is capped and tightened the vessel is filled with a liquefied gas. Platinum precursor solutions are made in concentrations below 0.1 M.

A novel nozzle to spray and combust the precursor solution was fabricated to include three distinct sections. These sections include a replaceable tubular insert, an induction coil wrapped around the back two thirds of the tubular insert and a gas routing head into which the front one third of the insert was positioned. The replaceable tubular insert consists of two lengths of stainless 316 tubing soldered together. The two lengths of stainless steel have different inner and outer diameters. A thinner tube is inserted into the thicker tube, soldered with argon flowing through the two lengths to prevent excessive oxidation inside the tubing. Once soldered together, these two pieces are referred to as the needle. Wrapped around the back two thirds of the needle is an induction coil. The induction coil is placed directly behind the gas routing head and electrically insulated with a piece of alumina. The circular gas routing head consists of a central port for insertion of the needle, two ports for introduction of burner gases, and a fourth inlet port for a spray shaping gas. The RSDT nozzle is attached to an Isel® three axis motion controller which is controlled by an Isel® Schrittmotor C142-4 controller (Techno, Inc., New Hyde Park, NY).

After the burner nozzle, an air quench system is aligned with the main burner. It consists of two air knives angled at 56° from centerline of the nozzle and supplied by compressed air. They sit atop a positioning system to precisely

control their linear distance from the nozzle exit, their distance between each other, and angle from the centerline. Immediately following the quench system is a set of secondary spray nozzles. The pair of slurry nozzles also sit atop a linear positioning system that also controls distance between nozzles and distance from quench nozzles and also the angle to spray centerline. The liquid to the secondary spray nozzles is supplied by a model NE1600 syringe pump (New Era Pump Systems, Inc., Wantagh, NY) using two 60 ml syringes.

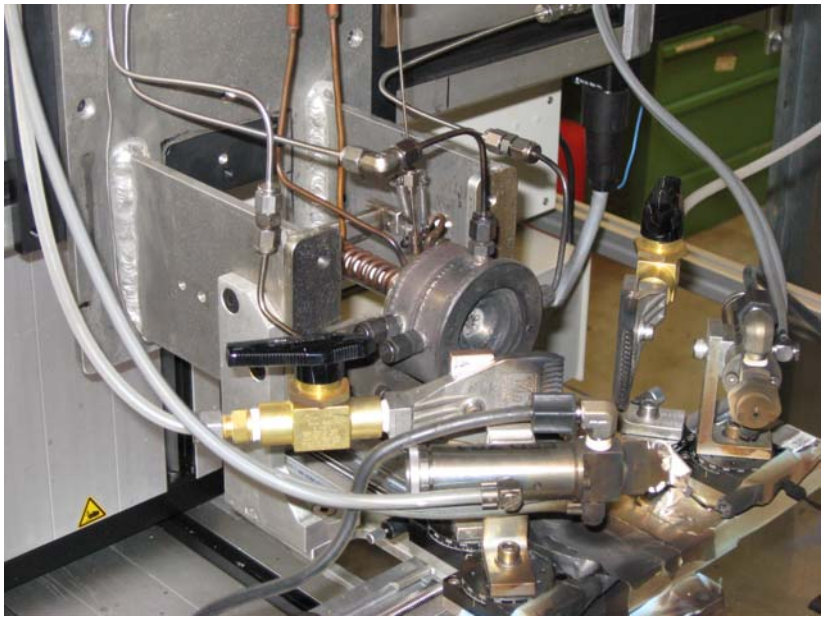

Figure 19: Side view of reactive spray combustion nozzle, pair of air quench nozzles and pair of slurry nozzles

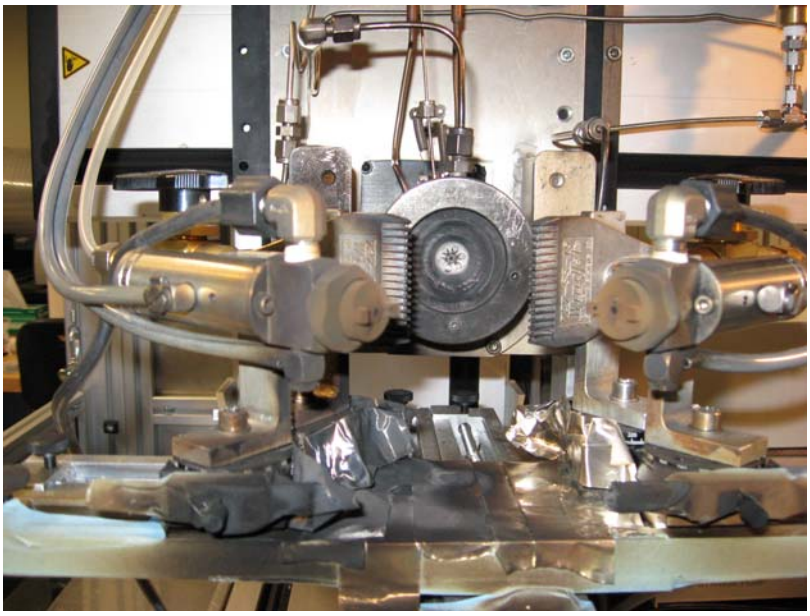

Figure 20: Front view of - reactive spray combustion nozzle, pair of air quench nozzles, and pair of slurry nozzles

A carbon/ Nafion® ionomer slurry solution is prepared by carefully weighing Vulcan XC-72R (Cabot Corp., Billerica, MA), adding the desired amount of solvent and then stirring the solution for ~10 minutes on a stir plate. To this solution is added the required Nafion® perfluorinated resin solution (Sigma-Aldrich, St Louis, MO); consisting of 5 wt.% in a mixture of lower aliphatic alcohols and water. The solution is then sonicated, while being stirred, using a Misonix 3000 sonicator (Misonix, Inc., Farmingdale, NY).

Samples were mounted to a specially fabricated aluminum backplane with 3 - 5 X 5 cm mask sections spaced 3 cm apart and 3 cm from each edge side as shown in Figure 21. The sample holder is 27 X 10 cm in dimension and can simultaneously hold 3 samples at one time. Temperature is monitored by use of a thermocouple placed just above the upper right hand corner of the third sample that is hooked up to a LabView monitoring system. Pump pressure, flow rate, and temperature are recorded and logged.

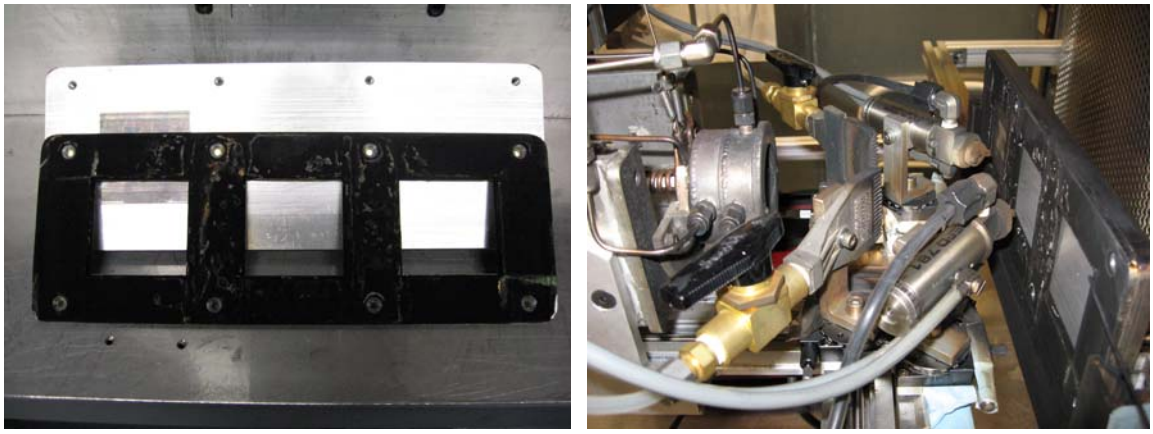

Figure 21: Mask used for 5 cm X 5 cm sample deposition area

The parameter inputs for the RSDT nozzle, quench nozzle and slurry nozzles are listed in Table 3.

independent RSDT nozzle parameters		
	unit	***area of interaction***
platinum metal solution flow rate	mL/min	metal deposition rate, platinum morphology, droplet size and back pressure
nozzle temperature	^{o}C	droplet size, dryness of droplets, back pressure and spray stability
collimating gas	SLPM	spray angle, flame velocity, laminar or turbulent flame, oxidizing potential of flame and substrate temperature
pilot oxygen	SLPM	maintain combustion of spray
pilot methane	SLPM	maintain combustion of spray
independent quench nozzle parameters		
quench air flow rate	SLPM	stops reaction in flame, cools reaction zone, cools substrate, rate of deposition and determines deposition pattern
quench angle	θ from centerline	deposition pattern, substrate temperature and causes eddys
independent slurry nozzle parameters		
slurry solution flow rate	mL/min	substrate temperature, ratio of metal to ionomer and carbon
slurry nozzle air pressure	psi	droplet size
slurry nozzle angle	θ from centerline	spray pattern and splatting

Table 3: Independent variables and common values for RSDT nozzle, quench nozzles and slurry nozzles

The exact values of these parameters are not listed due to intellectual property restrictions covered United States Patent Application 20080280056. Many of these variables require further optimization to increase deposition efficiency, improve repeatability and reduce process material costs. Clearly, an enclosed shroud system to confine process gas, manage heat and direct the expensive catalyst to the substrate is warranted. Slurry flow rates were chosen to prevent solvent drips on the substrates and the carbon concentration was chosen to match platinum deposition rates for the required Pt/C weight ratio. The liquefied gas to solvent ratio was chosen so that the platinum II, IV pentanedionate remained in solution while still providing a steady non-pulsating flame. The stability of the flame was also a function of the operating temperature of the nozzle. If the nozzle temperature is too high for a given flow rate and solvent/liquefied-gas ratio, then pulsation in the spray would occur. Further increases in temperature caused precipitation of the solute and blockage of the nozzle assembly. A pressure transducer in the pump head monitored the presence of clogging in the nozzle needle.

System optimization requires defined product specifications such as catalyst particle size and distribution, positional catalyst loading variation, thickness variation, contamination and composition to monitor changes in input parameters. This thesis lays the groundwork for a follow-up with a more detailed set of experimental design tests related to PEM catalyst layer optimization.

3 Preliminary compositional, structural and chemical analysis of RSDT sprayed electrodes

3.1 Introduction

Initial experiments were performed using the RSDT spraying system as described in Section 2. It was important to verify that metallic platinum and not unreacted, decomposition or oxide products of the metal-organic ligand were produced. It was also necessary to verify the size of platinum particles being generated, the deposition rates, and electrode thickness using the un-optimized RSDT system.

3.2 Experimental procedure

In order to check the size of the platinum particles being generated a specially coated 3mm Cu 200 mesh TEM grid (SPI, West Chester, PA) was placed in the path of the combustion zone at 15 cm from the nozzle face. Samples were held in the axis of the flames path for 45 seconds. Analysis was performed on a Hitachi H7600 transmission electron microscope with a 120kV tungsten filament.

It was also prudent to examine cross-sections of platinum-only unsupported catalysts as well as supported catalyst cathode layers to determine the thickness of the sprayed layers. Preparation of cross-sections required cutting samples into a triangular shape and encasing the samples into a resin. The resin formulation used is generically known as Spurr's (SPI Supplies, West Chester, PA) and is formulated according to needed viscosity. The very soft recipe was initially used for preparation but it was later found that the medium and hard formulations yielded better sections.

viscosity	ERL 4221 (g)	NSA *(hardner)* (g)	DER 736 (*plasticizer*) (g)	DMAE *(accelerator)* (g)	ERL/NSA wt. ratio	ERL/DER736 wt. ratio
Very Soft	5	12.5	4	0.15	0.40	1.25
Soft	4.1	5.9	1.9	0.1	0.69	2.16
Medium	4.1	5.9	1.43	0.1	0.69	2.87
Hard	4.1	5.9	0.95	0.1	0.69	4.32

ERL 4221 - Vinylcyclophene Dioxide
NSA - Nonenyl Succinic Anhydride
DER-736 Diglycidyl Ether of Polypropylene Glycol
DMAE - Dimethylaminoethanol

Table 4: Spurr's resin formulation used in preparation for the Ultra-cut Microtome

Once encased in the resin, the samples were then taken to the UBC Bioimaging facility and cut on a Reichert Ultracut E microtome. Sectioning required the use of a diamond knife as the cheaper glass knives were not straight enough over the length of the sample to evenly section the required thickness of 60-90 nm. Since the samples are hydrophobic, insufficient adherence of the resin to the samples presented a challenge during sectioning. Often the resin would detach from the sample once the cut was made. Cut pieces of the aligned and trimmed samples were collected by floating the cut piece into de-ionized water held in a reservoir behind the diamond knife. TEM grids were then either dipped into the reservoir at a 45^0 angle near a sample to attach it to the grid or a loop was used to isolate a floating sample. Using the loop technique, the TEM grid was placed on an absorbent cloth and the loop was placed over the grid and pressed down until the water held in the loop flowed over and around the grid while depositing the sample on the grid. This technique was the easiest, but if the water flowed too fast then the cross section would wrinkle on the grid.

To confirm that the phase of the sprayed material was metallic platinum and not the partial or fully decomposed precursor, a series of x-ray diffraction investigations was performed on glass and silicon wafer substrates. The first test involved placing a glass substrate and a silicon wafer axially into the reaction plume at a distance of 20 cm from the nozzle face. The samples were then

analyzed on a D8 Advance x-ray diffractometer (Bruker-AXS, Madison, WI) using a Cu-anode at wavelength 0.154 nm at power settings of 40 kV and 40 mA.

Since powder x-ray diffraction is a technique for bulk phase analysis and is not suited to understanding surface phenomena or for trace analysis, samples were analyzed by x-ray photoelectron spectroscopy. The samples were analyzed on a Leybold MAX 200 X-ray Photoelectron Spectrometer at the Interfacial Analysis & Reactivity Laboratory (IARL) located in the Advanced Materials & Process Engineering Laboratory (AMPEL) at UBC by Dr. Phillip Wong. Reference materials from commercially available sources were first analyzed to compare and contrast the platinum formed by the RSDT method. These references were platinum foil (American Elements), platinum black product #183003 (Johnson Matthey, London, UK), platinum II,IV pentanedionate (Colonial Metals, Elkton, MD) and E-Tek's 40 wt.% platinum on Vulcan XC72-R carbon (BASF Fuel Cell GmbH, Frankfurt, Germany). Platinum foil was examined because the platinum is in the bulk phase and particle size effects on the XPS spectrum are absent. Platinum black was chosen because particle size effects are present, platinum II,IV pentanedionate was chosen to examine how un-reacted precursor behaves, and the E-Tek supported catalyst was chosen to reference a commercially available carbon supported platinum catalyst.

3.3 Results and discussion

3.3.1 Transmission electron microscopy

An average of 26 measurements in 5 different areas of the grid gave an average particle size of 5.4 nm (σ = 2.8 nm). This method is only semi-quantitative as it is difficult to measure the very small particles and serves only as a rough guide. As discussed in the literature review section of this thesis, an optimum particle size appears to be 2-3 nm with larger particles having a larger

percentage of the platinum in the interior of the particle unable to participate in the oxygen reduction reaction.

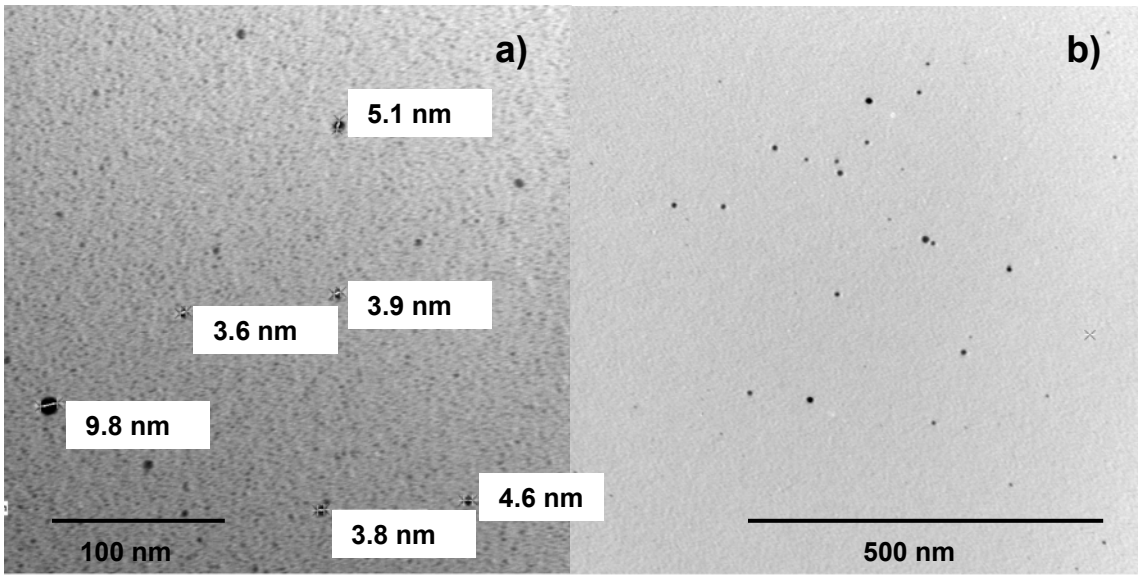

Figure 22: Particle size of platinum particles collected 15 cm from RSDT nozzle face a) 500 kX b) 200 kX

The first TEM section of a deposition directed at a polypropylene substrate was of a coating formed by 40 minutes of deposition with the secondary spray nozzle turned off (no carbon or ionomer). This type of electrode architecture is referred to as unsupported platinum. The motion program was 9 cm by 17 cm (153 cm^2 deposition area).

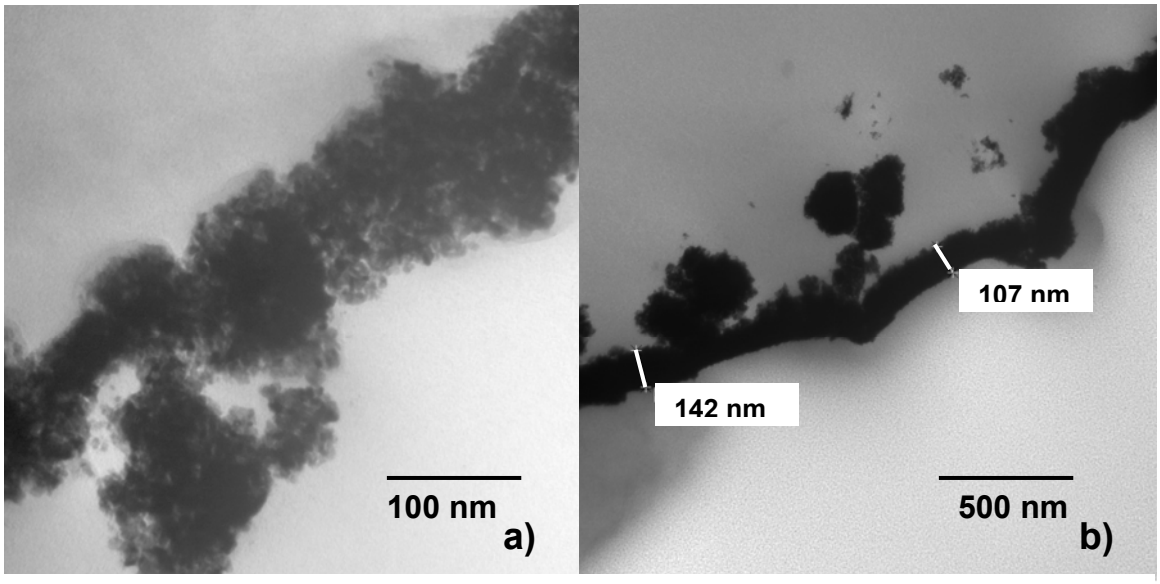

Figure 23: Cross-section of platinum only depositions 70-100 nm thick onto a Nafion NRE-211® membrane, 80 minute deposition with secondary nozzles turned off a) 400 kX b) 120 kX

The resulting micrographs show a microstructure that appears 100-150 nm thick with nodes of similar thickness dispersed at intervals along the length of the film. The nodes of 100-200 nm in diameter could be sections that have come undone from other areas or could be the result of an uneven growth mechanism. The resulting deposition rate is 1.2 – 1.9 nm/min based on these micrographs. It is also important to note that the resulting film does not appear dense but rather as a collection of closely packed aggregates of platinum 10-20 nm in diameter. Inductively coupled mass spectrometry was performed on the sample and the platinum loading was 0.067 mg/cm^2.

A ternary phase composite electrode made of carbon, Nafion®, and platinum sample was then prepared to examine the microstructure and thickness. The motion program was 9 cm by 9 cm (81 cm^2 deposition area) and the carbon slurry concentration was 1.6x10^{-3} g/mL. Figure 24 shows the results of the deposition. It is evident that there is a ~400 nm darker interfacial region between the NRE-211 membrane and the sprayed electrode. The reason for the darker

region is not clear. The platinum appears to be well distributed in the layer, with most platinum particles well below 10 nm. The darker grayish outlines represent the carbon support and the lighter grey the ionomer or where resin has penetrated the electrode. The white areas appear to be tears in the thin sections but may possibly be pores. Distinguishing the exact location of the ionomer from the pores requires staining but this avenue was not explored due to time constraints(110). The carbon support appears to form clusters or aggregates in the 100-200 nm range.

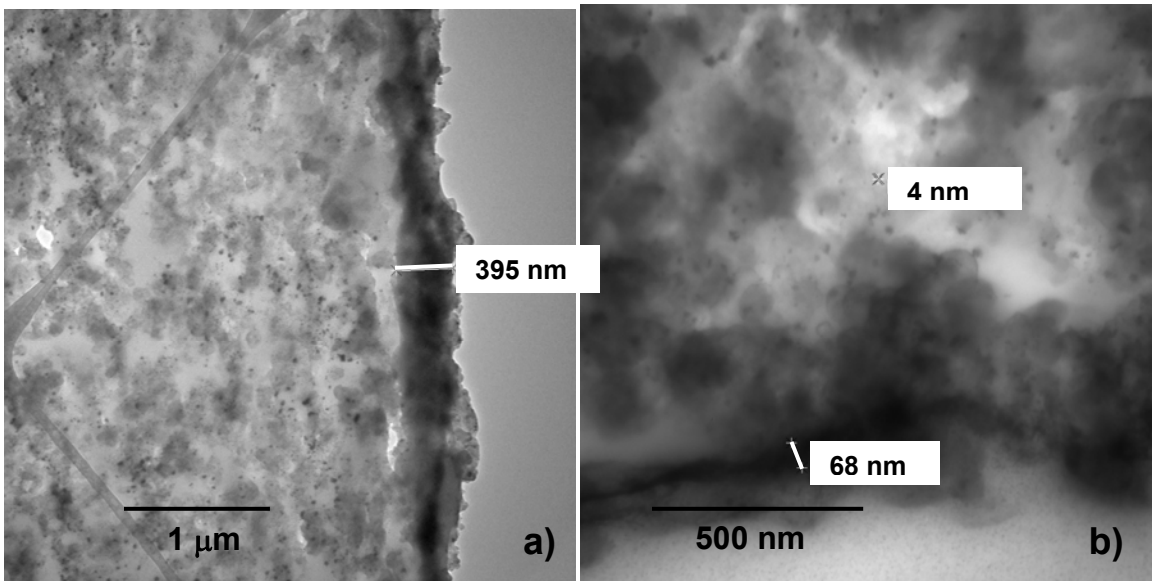

Figure 24: Cross-section of ternary component electrode showing a darker ~400 nm interfacial region between the electrode and the substrate a) 40 kX b) 120 kX

A lower magnification image was taken to examine the total electrode thickness as shown in Figure 25. The thickness is 5.5 microns and the deposition time was 100 minutes, leading to a deposition thickness rate of 55 nm/min. This is a much higher rate than recorded above for platinum only samples because the carbon in the spray (absent in the platinum only deposition) forms the bulk of the ternary phase.

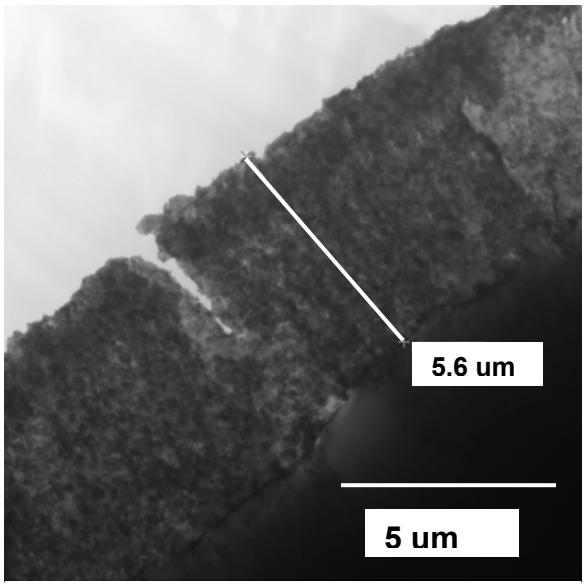

Figure 25: Cross-section of ternary component electrode showing an overall electrode thickness of 5.5 microns.

In addition to unsupported platinum and supported platinum samples, a hybrid bi-layer sample containing a platinum base layer followed by a ternary layer was produced and sectioned, as shown in Figure 26. The motion program was 9 cm by 9 cm (81 cm^2 deposition area) and the carbon slurry concentration was $3.2x10^{-3}$ g/mL.

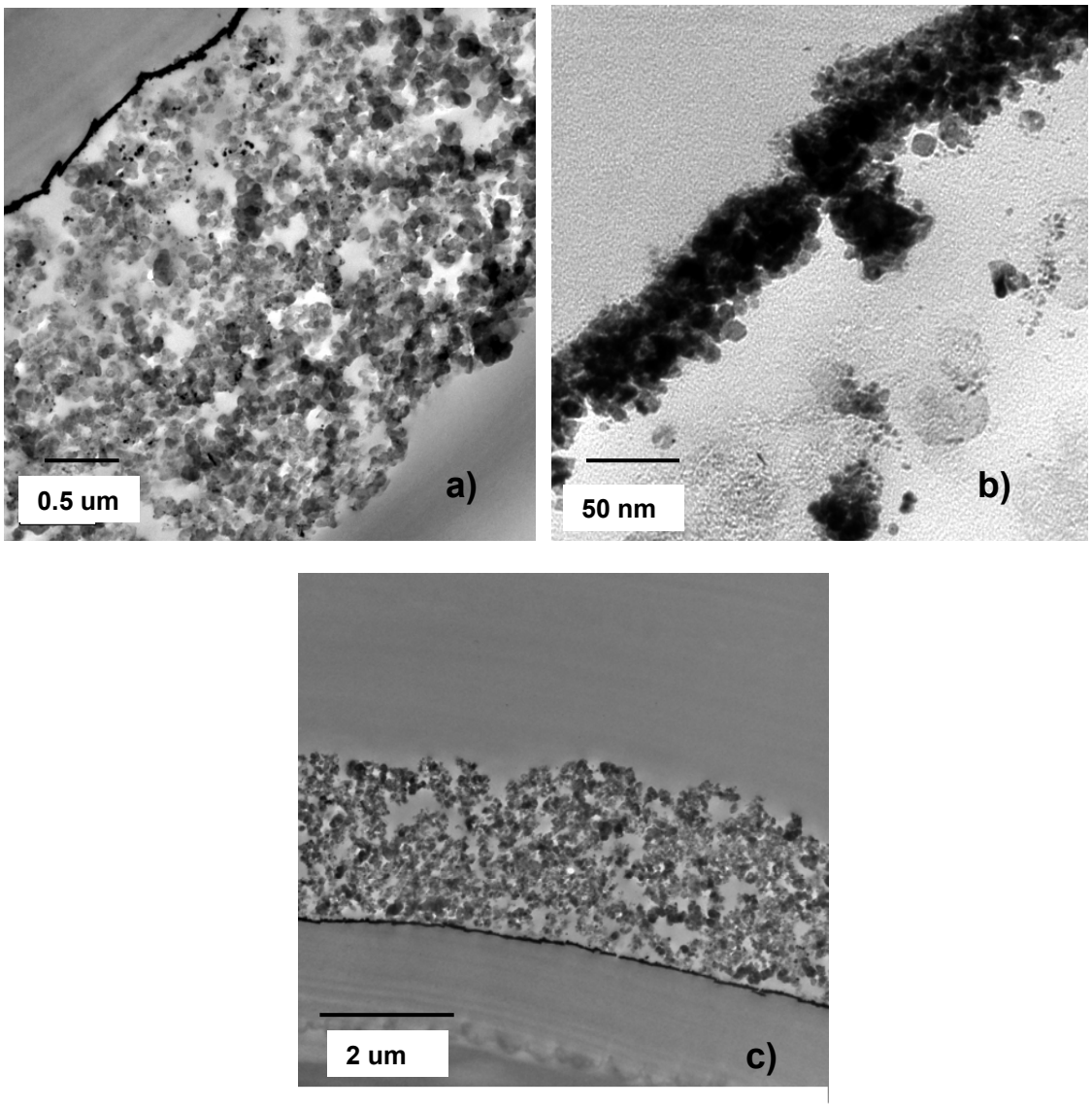

Figure 26: Cross-section of a hybrid platinum sub-layer and ternary composite electrode showing a ternary composite thickness of 3.5-4 microns thick and a sub-layer of 50 nm thick.

The thickness of the platinum only sub-layer is 50 nm, and it was deposited in 20 minutes, giving a thickness deposition rate of ~2.5 nm/min. The ternary layer was deposited in 15 minutes, corresponding to a thickness deposition rate of 230-260 nm/min. The thickness data for the three architectures are displayed in Table 5.

deposition area (cm^2)	*platinum time (minutes)*	*sub-layer thickness (nm)*	*platinum thickness rate (nm/min)*	*carbon conc. (g/mL)*	*time (minute)*	*tertiary thickness (μm)*	*tertiary thickness rate (nm/min)*
153	40	100-150	1.2-1.9	NA	NA	NA	NA
81	NA	NA	NA	1.60E-03	100	5.5	55
81	20	50	2.5	3.20E-03	15	3.5-4	230-260

Table 5: Thickness and thickness rates for three different RSDT fabricated electrode architectures – unsupported platinum, carbon supported platinum, and bi-layer.

The use of different rastering programs and deposition times can explain the discrepancies in the deposition rate of the platinum sub-layers. One program covered an area of 153 cm^2 for 40 minutes (1.2-1.9 nm/min), while the other an area of 81 cm^2 for 20 minutes (2.5 nm/min). The area covered was almost double but so was the deposition time for the larger area sample. The slight difference in thickness measurements can be somewhat rationalized because the actual spray area formed by the plume volume is a circle between 4-5 cm wide, and this overlap of 2-2.5 cm allows for much less overspray on the smaller deposition area. The difference in the deposition thickness rate of the two ternary layers is almost 4 times (230-260 nm/min versus 55 nm/min). Half of the difference in deposition thickness rate is due to a more concentrated carbon slurry ($3.2x10^{-3}$ $g_{carbon}/mL_{isopropanol}$ versus $1.6X10^{-3}$ $g_{carbon}/mL_{isopropanol}$). The rest of the difference can be attributed to using a passive pressurized vessel to pump the slurry versus putting the slurry into a syringe pump and actively pumping the slurry into the nozzle. Additionally, there could be settling of the slurry over time that could be affecting the flux over time.

3.3.2 X-ray diffraction

The reactive spray deposition equipment was operated according to the values in Table 3. Sample substrates of a silicon wafer and float glass were held in the reaction plume for 45 seconds. After removing the samples from the flame zone, a shiny reflective metallic coating was visible on the substrates. Figure 27

shows a diffraction pattern collected from these specimens superimposed on the pattern for metallic platinum in the ICDD database (card# 00-004-0802).

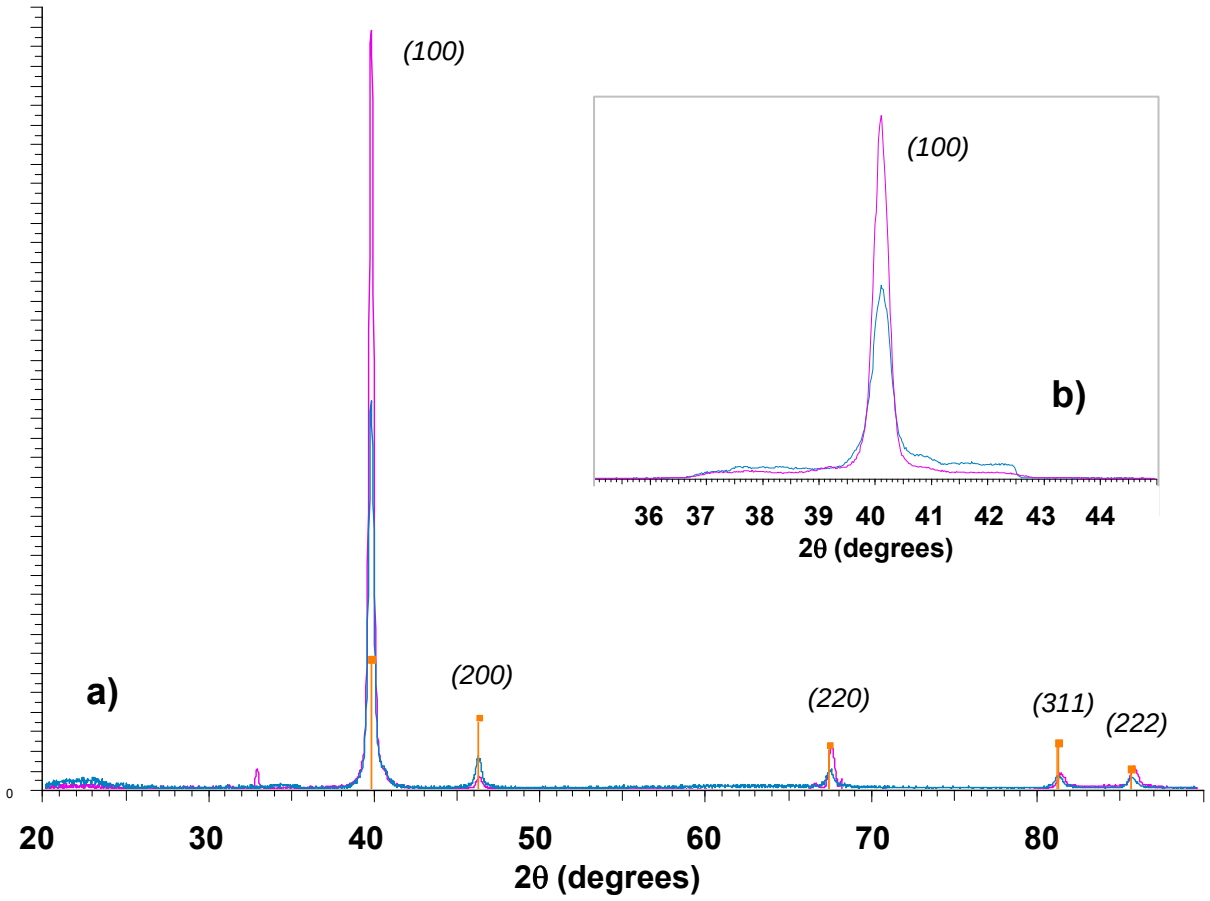

Figure 27: a) Unquenched shiny, metallic Pt coating collected at 20 cm (T_{gas} ~550°C) Pt on glass (blue) and on Si wafer (magenta) b) The inlay shows a zoom of the (100) peak.

Considering the ratio between the peaks, the coatings show a preferential (100) orientation compared to the reference Pt pattern.

The quench gas was then turned on and the samples were held at distances of 9 cm and 15 cm, at which the gas temperatures were 220°C and 130°C, respectively.

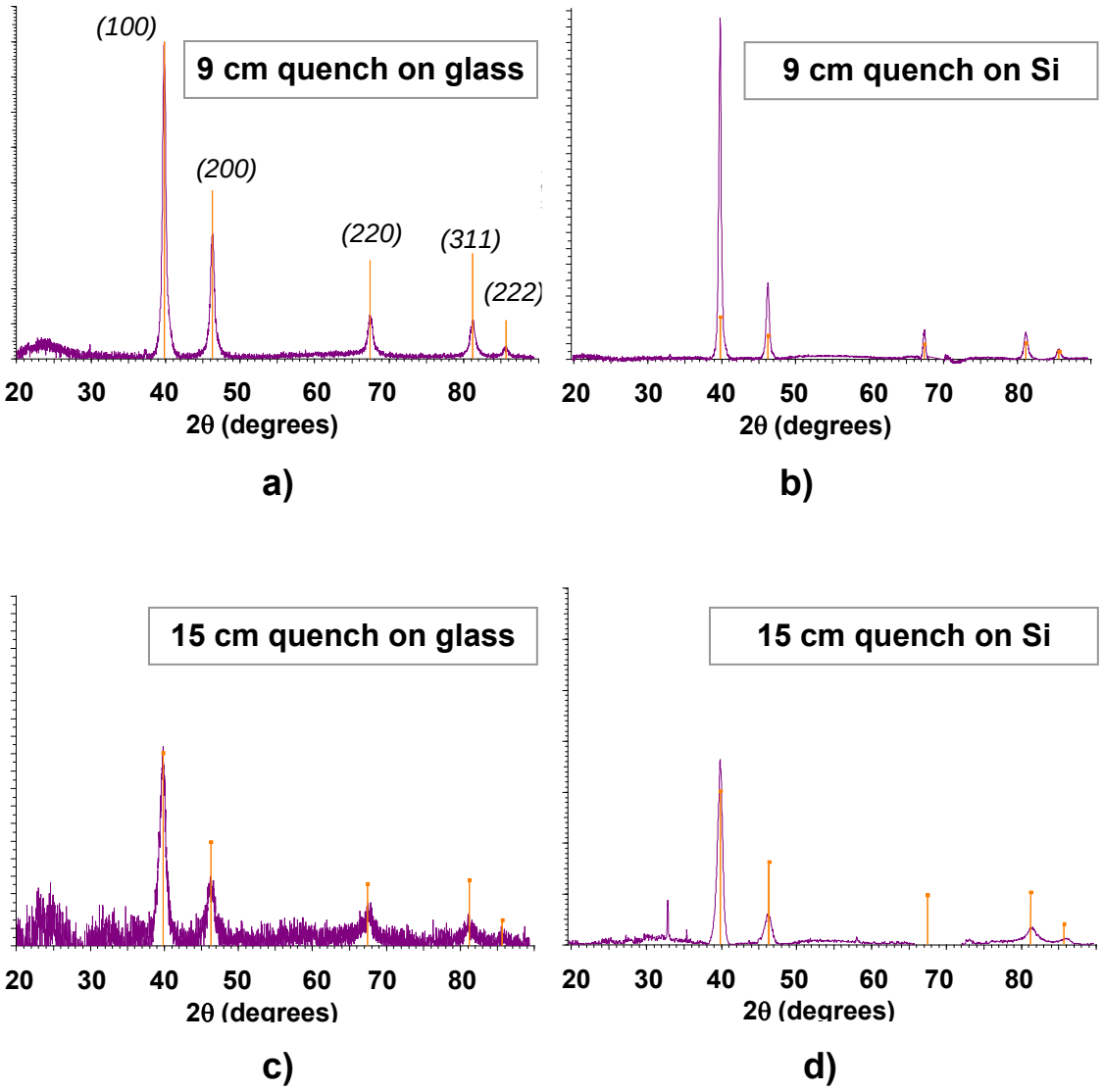

Figure 28: XRD patterns of quenched Pt depositions at 9 cm (T_{gas} ~220°C) and 15 cm (T_{gas} ~130°C). a, c - glass; b, d - Si wafer. Pt pattern ICDD# 00-004-0802 in orange.

As shown in Figure 27, on the unquenched samples the pattern for face-centered cubic platinum is present. The (220) peak of sample d) in Figure 28 has been lost during background subtraction because it superposes on the very strong (040) peak of the Si mono-crystal substrate used. The Si mono-crystal substrate gives less scattering than the corresponding glass substrate. On all the substrates a slightly preferential (100) growth is present.

In Figure 29, depositions on glass (blue) and Si (magenta) substrate are directly compared. The glass coating's peak height has been scaled up to match the intensity of the Si wafer coating's (100) peak so that comparison of preferential orientation of crystal growth between the two substrates can be more easily viewed. Only the (100) and (200) peaks are shown since they are the two strongest peaks, and this allows for ease in comparison across a more narrow 2θ range.

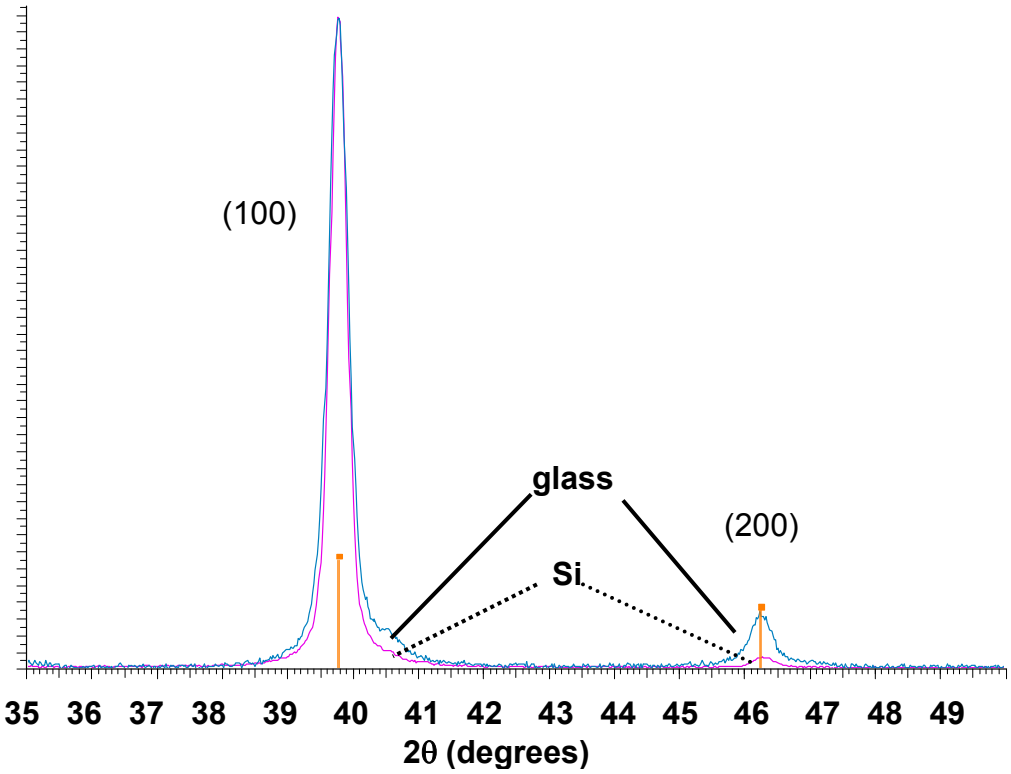

a) – 20 cm, no quench

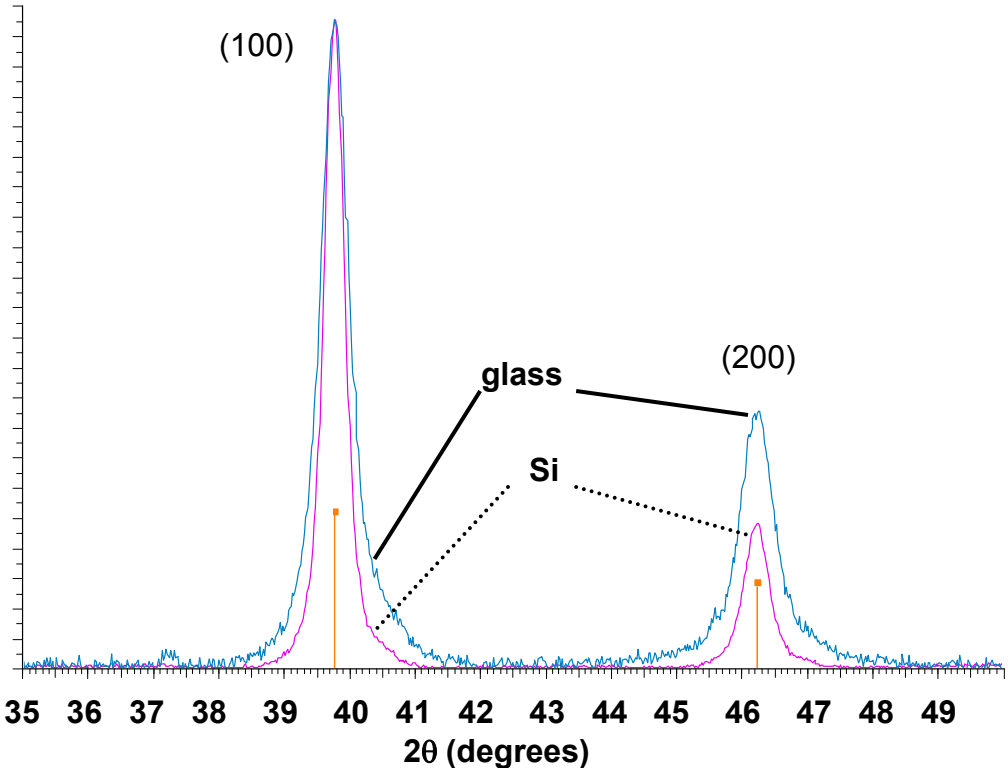

b) – 9 cm deposition distance, quenched

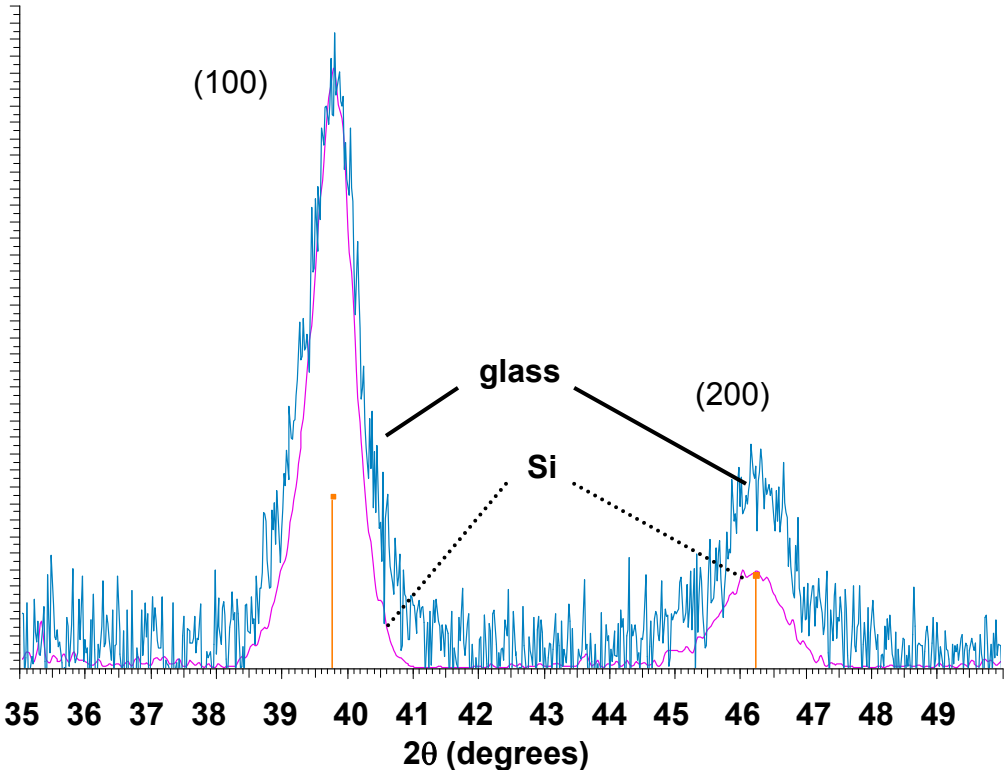

c) – 15 cm deposition distance, quenched

Figure 29: Direct comparison of scaled patterns of coatings on glass (blue) and Si wafer (magenta) at a) **– 20 cm, no quench;** b) **– 9 cm, quenched and** c) **– 15 cm quenched. (100) – (200) peaks region.**

A comparison of scans in Figure 29 shows that the crystallite size as evidenced by the peak width at half maximum height (FWHM) is close for both substrates but is slightly smaller for the Si samples. This indicates that under these deposition conditions the substrate is not a big factor in determining platinum crystallization. An apparent decrease of the crystallite size can be observed between un-quenched and quenched depositions. This effect can be explained by the mechanism of particle growth in the flame and the substrate temperature. The unquenched deposition occurs directly from sublimation as shown in Figure 29 a, while in Figure 29 b and Figure 29 c the platinum vapors nucleate and are then rapidly cooled. This causes the vapors to crystallize rapidly and deposit as solids striking the substrate. Although slightly smaller, the crystallite size of the 9

cm coating is very close to that of the unquenched 20 cm coating and larger than the 15 cm coating crystallite size (FWHM of the 20 cm coating is ~0.35°, for the 9 cm coating FWHM is ~0.4° while FWHM of the 15 cm coating is ~0.7°). This trend shows that the particles may have a tendency to re-crystallize and grow on the hotter substrates (220°C and 550°C). This does not happen during the relatively longer flight in the gas stream, for the 15 cm sample. This might eventually be an issue for the long-term stability of the catalyst. The (100)/(200) peak intensity ratio decreases on both the glass and silicon when the quench is applied.

Next a comparison of RSDT produced platinum particles to commercially available products was made. High surface area 24.4 - 29.2 m^2/g platinum black product #183003 (Johnson Matthey, London, UK) and E-Tek's 40 wt.% platinum on Vulcan XC72-R carbon (BASF Fuel Cell GmbH, Frankfurt, Germany) were analyzed by XRD. E-Tek lists the surface area of the carbon and platinum as 250 and 100 m^2/g, respectively. The platinum particle size is listed as 2.8 nm. Figure 30 shows a direct comparison of the RSDT powder catalyst deposited at 15 cm on glass and Si wafer to the E-Tek's C-supported Pt catalyst and to the Pt black powder.

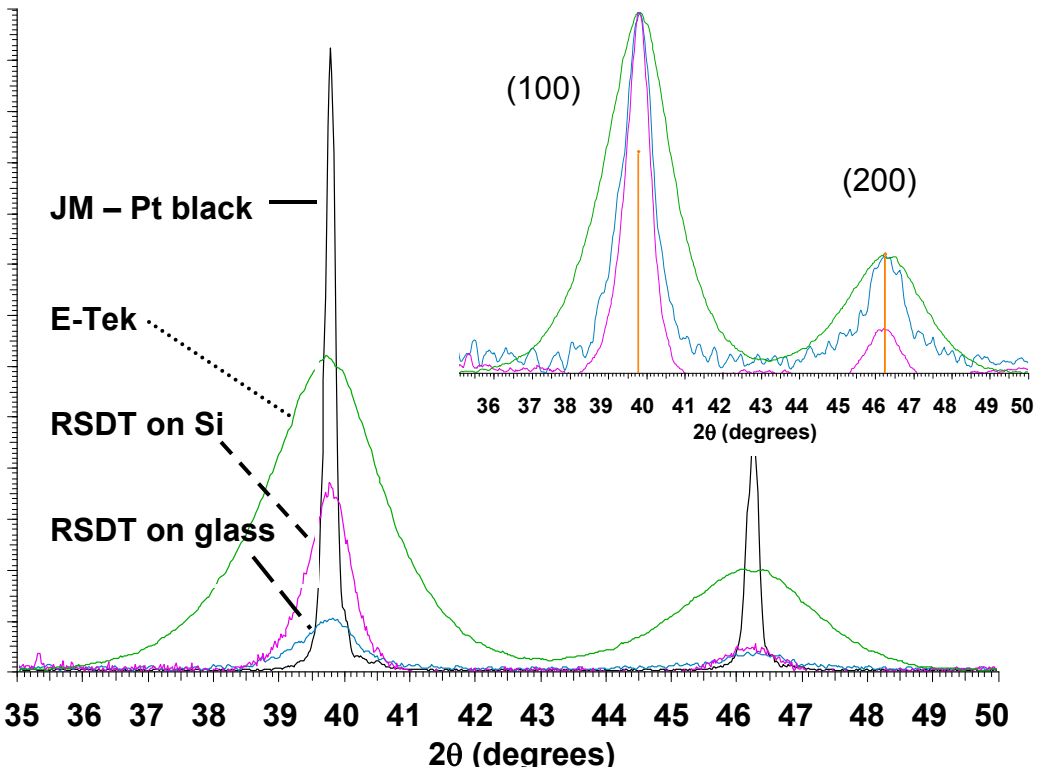

Figure 30: XRD patterns of RSDT catalysts and reference materials, (100) and (200) peaks region. Black – Pt black powder (Johnson Matthey), green – E-Tek C-supported Pt, blue – RSDT Pt powder on glass, magenta – RSDT powder on Si wafer. Inlay – patterns have been scaled to fit (100) peak.

The average crystallite size of the RSDT produced catalyst is smaller than the platinum black powder. However, it is larger compared to E-Tek's catalyst – see inlay in Figure 30. This confirms the TEM images in Figure 22 that show an average particle size of 5.4 nm (σ = 2.8 nm).

One roadblock encountered in method development was the need for a quick and inexpensive check of platinum loading. Depositing platinum only (without carbon or ionomer) for a given amount of time and then weighing the difference is an easy way to quickly check the loading. However, this method requires that the substrate mass not change during deposition. Unfortunately during deposition conditions the hydration and thus mass of the Nafion® electrolyte changes and so gravimetric methods of loading determination are not possible using Nafion®. Additionally, Nafion® is expensive and a suitable

substrate blank was needed for non-electrochemical analysis, so samples of high-density polypropylene (Office Depot) were examined by XRD as a suitable substrate material.

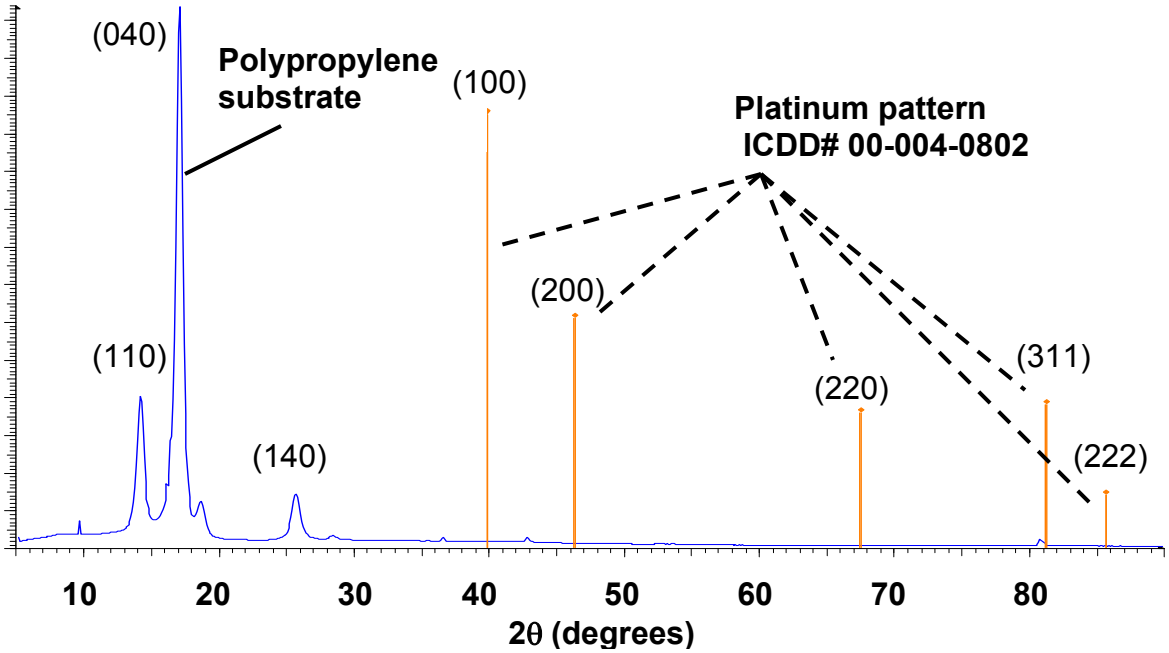

a)

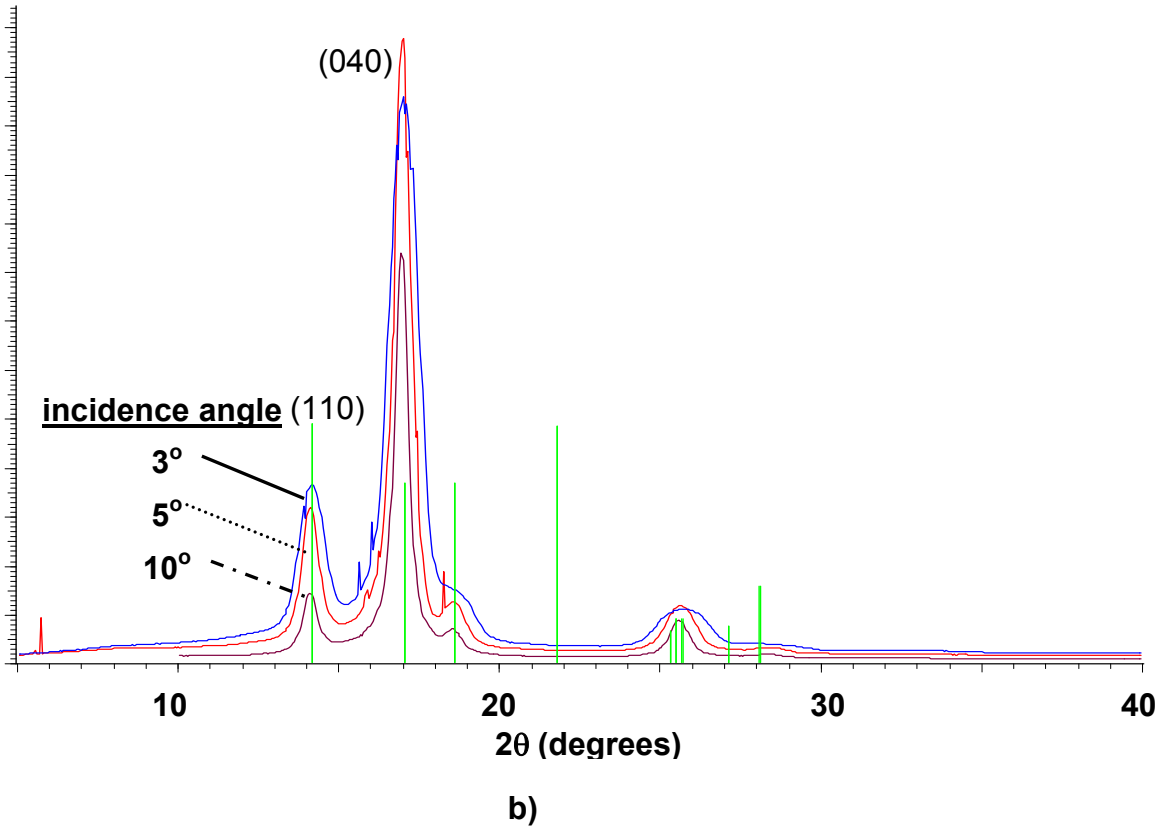

Figure 31: HD polypropylene $(C_3H_6)_n$. a) – polypropylene film (blue) and platinum ICDD# 00-004-0802 pattern (orange). b) – polypropylene at different incidence angles (3° – blue, 5° – red and 10° – maroon) and polypropylene ICDD# 00-054-1936 pattern (green).

High-density polypropylene is a (semi) crystalline polymer, as can be seen in Figure 31. The preferential orientation into the *(040)* plane may be caused by the film lamination. The low angle peaks do not superimpose on those of platinum and therefore polypropylene is a good substrate for ex-situ characterization.

To determine if there was substantial quantity of platinum II, IV pentanedionate (see Figure 18) in the product, a diffraction pattern was obtained for the precursor material.

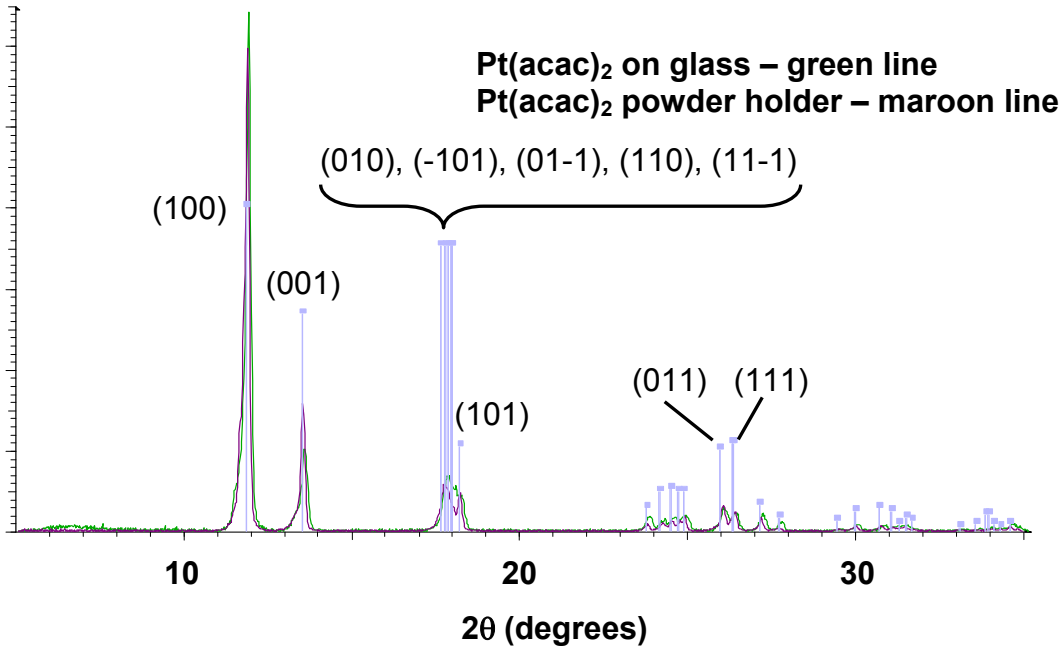

Figure 32: $Pt(acac)_2$ on glass slide (green), $Pt(acac)_2$ in powder holder (maroon), and $Pt(acac)_2$ ICDD# 00-050-2288 pattern (purple).

Pt $(acac)_2$ has the strongest peaks at ~12°, 13.5° and ~18° and no peaks above 37°. Therefore, it can be distinguished from crystalline Pt. However, it has main peaks that almost superpose on the high-density polypropylene peaks. X-ray diffraction is not a good analytical tool for trace analysis. Therefore, x-ray photoelectron spectroscopy will be used to search for surface contamination related to un-reacted or partially decomposed precursor.

The x-ray diffraction data show that the bulk phase of the deposited catalyst is platinum with a slight (100) preferred orientation. Considering that the FWHM of the (100) peak of platinum by RSDT on Si sample is 3/8ths that of the E-Tek catalyst with a stated size of 2.8 nm suggests that the RSDT crystallite size is 6.7 nm. Calculating the crystallite size directly by the Scherrer equation yields 3.5 nm for the E-Tek sample and 8.0 nm for the RSDT sample. A higher deposition temperature seems to encourage larger particle sizes and grain growth at temperatures of 220^{o}C and above. The grain growth and surface diffusion are common phenomena at elevated temperatures. While this aspect of

the deposition process would be interesting to pursue, it is not immediately useful since the catalyst coated membrane (CCM) direct deposition method requires temperatures to be below 150^{o}C. A full study of temperature related effects of the RSDT process on electrolyte conductivity and hydrogen cross over should be carried out to determine the processing limits of various electrolyte materials. From a practical point of view, a membrane that can withstand a higher temperature allows the process flame to be brought closer to the substrate, which facilitates a better deposition efficiency.

3.3.3 X-ray photoelectron spectroscopy

Platinum metal exhibits a certain degree of oxidation, even in the open atmosphere at standard temperature and pressure. This oxidation level can exist through physical interactions such as adsorption or can be chemical/electrical in nature. An XPS spectrum of a platinum foil that has been etched using a combination of thermal treatment, Ar^{+} ion bombardment, and high vacuum is shown in Figure 33(111). Two prominent peaks related to the platinum $4f_{5/2}$ and $4f_{7/2}$ electron orbitals occur at binding energies of 74.6 and 71.3 eV, respectively.

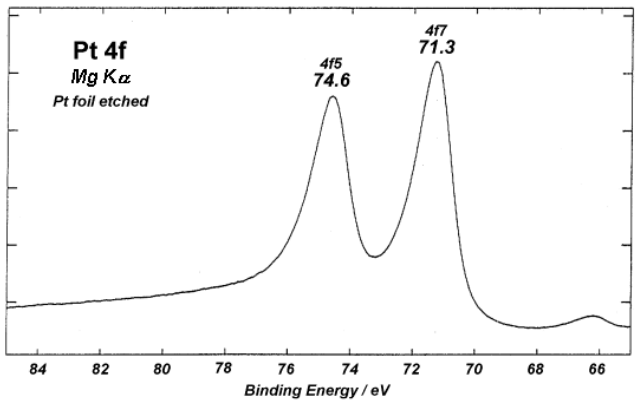

Figure 33: XPS spectrum from the literature of the Pt 4f5 and 4f7 peaks of an etched platinum foil sample using magnesium x-rays(111).

An XPS spectrum of a platinum surface (111) is shown in Figure 34 to illustrate how various degrees of oxidation affect the platinum $4f_{5/2}$ and $4f_{7/2}$ peaks, as well as the appearance of a peak at 76.9 eV (112).

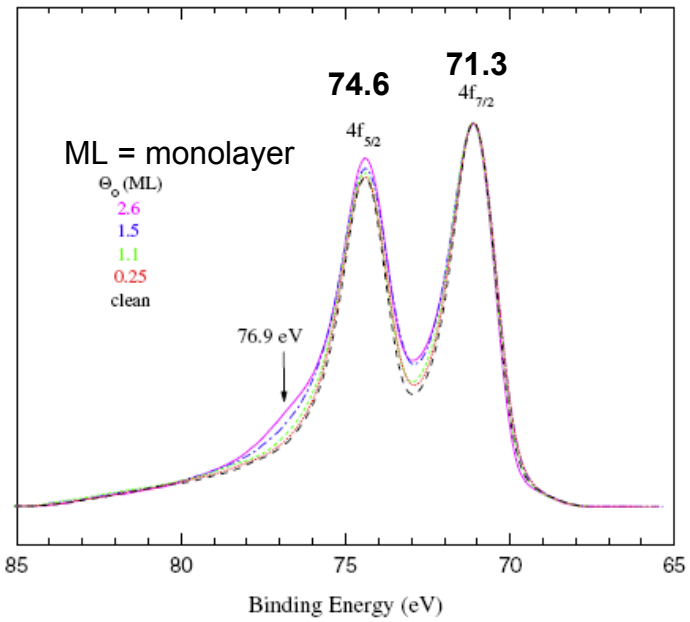

Figure 34: Pt(111) etched foil clean surface from the literature and increasing adsorbed oxygen evidenced by Pt4+ at 76.9 eV(112). [© Surface Science, 2005, by permission]

A high concentration of adsorbed oxygen on the surface of platinum metal is possible only by the formation of a chemical bond. Lower surface concentrations of oxygen atoms occur when intermediate oxidation states of the surface platinum atoms occur. Valence electrons are progressively transferred from Pt to O and the electrostatic interaction between the nucleus and the 4f electron becomes stronger. Such a modification of the interaction from physically adsorbed O to chemically adsorbed O can be observed in Figure 34. The minimum between the two Pt peaks increases at 72.9 eV, the $4f_{5/2}$ peak becomes higher, and a shoulder becomes visible at 76.9 eV. The observed XPS spectra represent the superposition of electron emission from the unique chemical environment of elemental species present on the top 1-10 nm. Therefore,

changes in the spectra in Figure 34 suggest the appearance of a second pair of peaks formed by a superficial layer of partially oxidized platinum. Since the occurrence of multiple peaks causes overlap, a method of peak deconvolution is necessary to estimate the contribution of each peak to the acquired spectra. Under conditions of standard temperature and pressure the surface of the platinum sample consists of an interfacial layer of Pt atoms to which oxygen atoms are bound, and below this is a layer of unaltered Pt atoms. In order to separate the contribution of each Pt species, a deconvolution procedure has been applied to the raw spectra using XPS Peak 4.1, developed by Raymond Kwok. The partially oxidized platinum is generically noted as Pt^{+} and Pt^{++} (indicating a lesser or greater degree of oxidation) and the unaltered atoms as Pt^{0} in the deconvoluted spectra.

Platinum foil and platinum black were analyzed at the UBC IARL to examine how the difference between a low planar surface area and high surface area particle affects the XPS spectra. Figure 35 and Figure 36 both exhibit a similar high-energy tail from the $4f_{5/2}$ peak and a higher valley close to the point where the two peaks start superimposing compared to the etched sample in Figure 33. The results of the deconvolution for the Pt foil reference sample show a combination of bulk, polycrystalline Pt atoms ($4f_{7/2}$ peak at 71.12 eV) and an oxidized phase whose binding energy corresponds to Pt^{2+} in PtO ($4f_{7/2}$ peak at 72.43 eV).

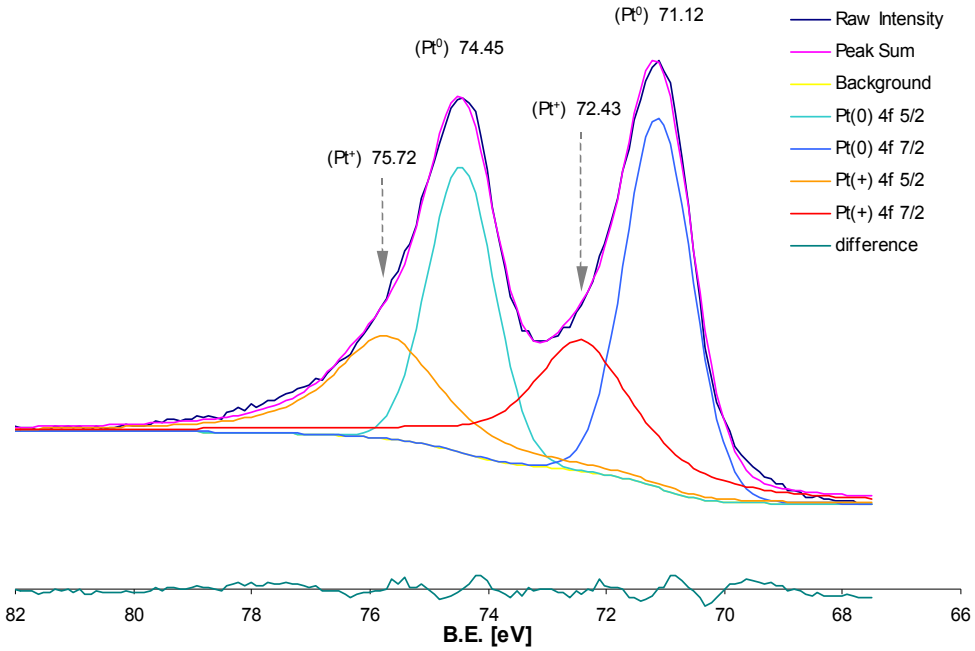

Figure 35: XPS spectrum of platinum foil with peak deconvolution.

The presence of an oxidized species is even more visible in the spectrum of the Pt black powder sample, as seen in Figure 36.

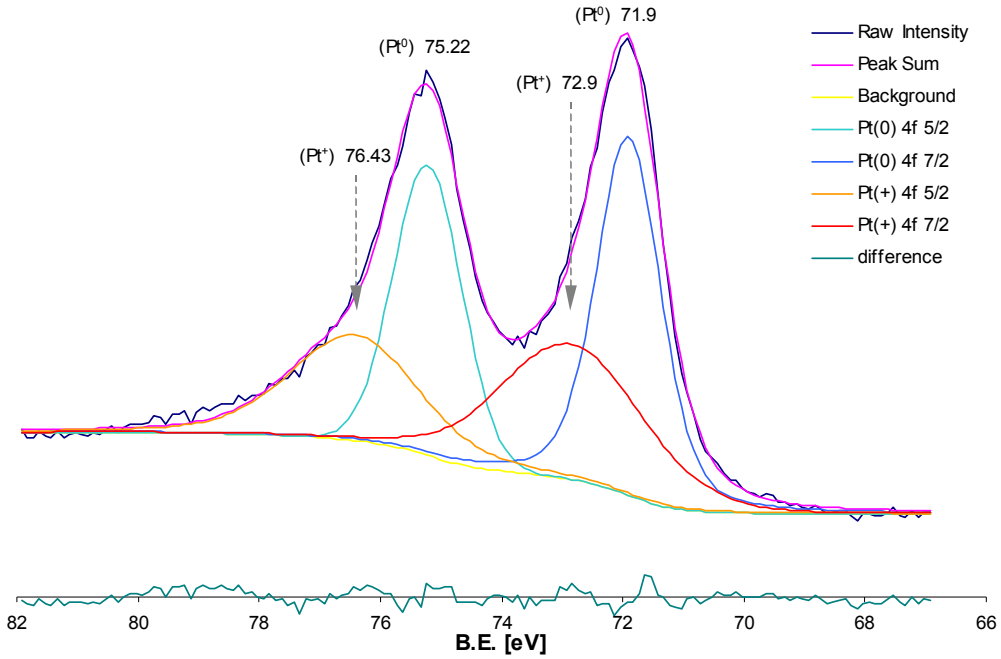

Figure 36: XPS spectrum of platinum black with peak deconvolution.

The same high energy tail and higher valley are present in the Pt black powder, with the distinction that all the peaks are shifted slightly towards higher binding energies. This shift, compared to the foil is approximately 0.7 eV for all peaks save the Pt^{+} $4f_{7/2}$, which is only 0.47 eV higher. Shifting may be attributable to sample charging and/or to the small particle size of the platinum black powder. XPS studies by Rambabu et al. suggest that the platinum 4f energy level of the lower binding energy of the doublet is found to increase from 71.1 eV in platinum metal to 71.64 eV for platinum black and this 0.54 eV shift can be attributed to small-cluster-size effects(113).

Platinum II, IV pentanedionate has the chemical structure shown in Figure 18. In this organo-metallic compound, platinum is expected to be in an intermediate oxidation state between Pt(II) and Pt(IV). As an example, the literature suggests two oxidation states of Pt species present in PtO_2, also known as Adam's catalyst. Those species are Pt(IV) (PtO_2, $Pt4f_{7/2}$=73.9 eV), and Pt(II) (PtO, $Pt4f_{7/2}$=72.3 eV)(111, 114). Therefore, the XPS spectrum of platinum II, IV

pentanedionate should have two peaks at energies slightly lower than those corresponding to the Pt(IV) species in PtO_2 – 72.3 eV.

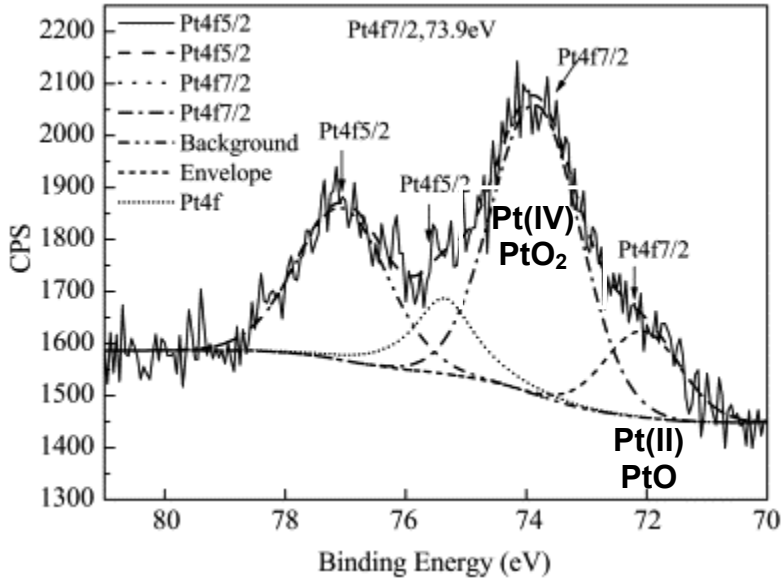

Figure 37: XPS spectrograms for platinum oxide nanoparticles, Pt4f region(114). [© Journal of Colloid and Interface Science, 2007, by permission]

The deconvoluted spectrum in Figure 38 shows the peaks corresponding to Pt^{2+} at 72.13 and 75.46 eV and a second species with a higher oxidation state, in between Pt^{2+} and Pt^{4+}. This suggests that platinum is mostly in a lower oxidation state such as 2^{+}, but some of the atoms might be in a hybrid state similar to Pt^{4+}, while sharing two valence electrons with four O atoms.

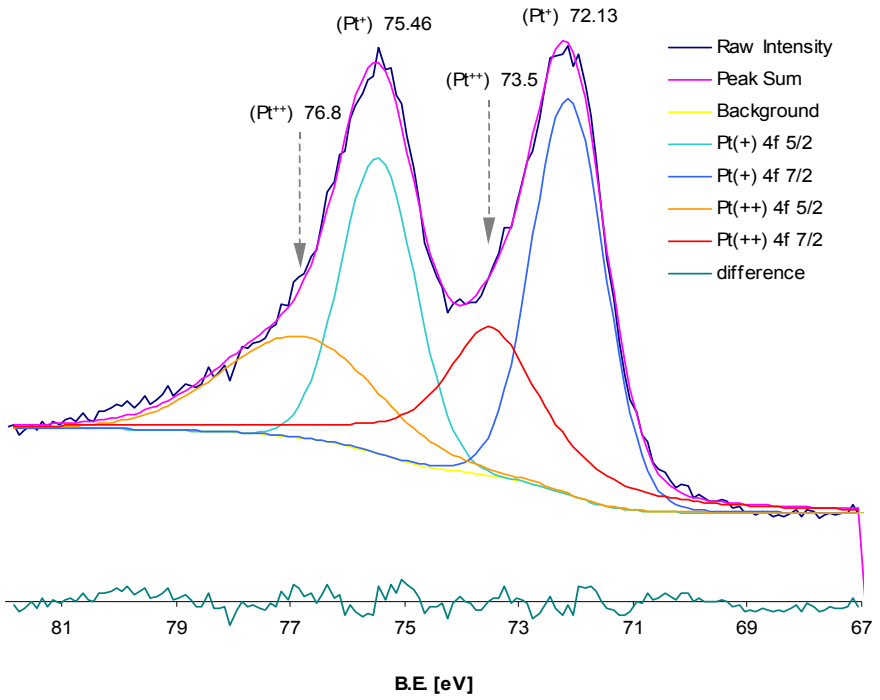

Figure 38: XPS spectrum of platinum II, IV pentanedionate.

The E-Tek carbon supported platinum catalyst sample exhibits almost exclusively one platinum oxidation state. However, this oxidation state has a very high binding energy (in between that of Pt^{2+} and Pt^{4+}. The small contribution of a second species is evident at lower BE values. The energies of this species are close to those of Pt^{0}.

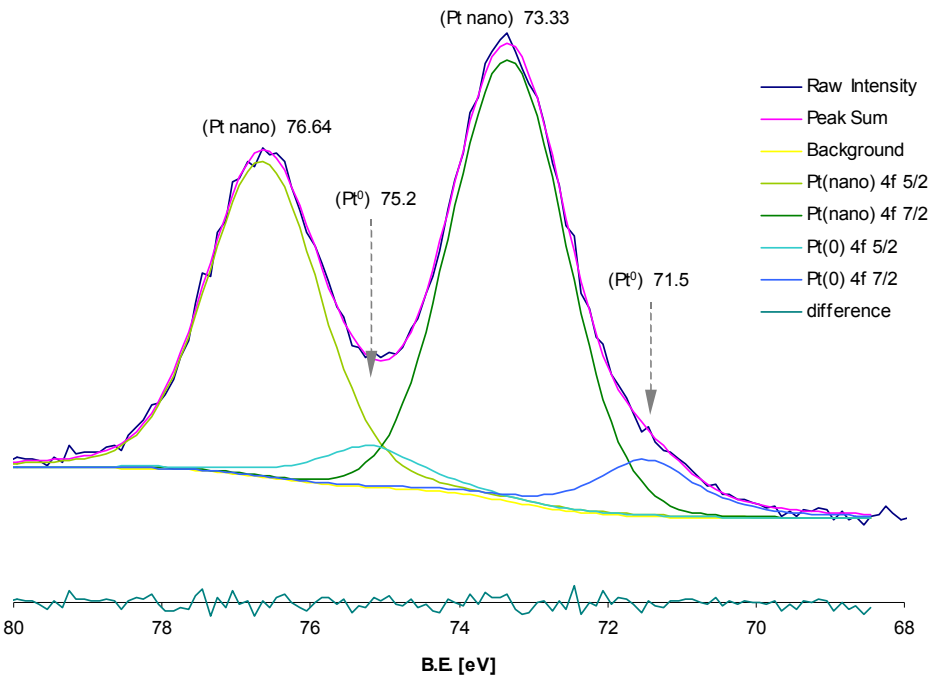

Figure 39: XPS spectrum of E-Tek 40 wt. % platinum on carbon.

The XRD spectrum in Figure 30 showed that platinum metal forms the bulk phase of this sample. The manufacturer reports a particle size of ~ 3 nm for the catalyst. Therefore the ~0.4 eV shift of the Pt^0 might be due to particle size effects. The high energy species present on the surface might be associated with a mixture of strongly chemisorbed O atoms and interstitial O atoms. The energies are high enough to suppose that most of the Pt atoms have transferred at least two valence electrons to the oxygen atoms (> 72.3 eV), but not high enough for the Pt atoms to be in the Pt^{4+} state (< 74.1 eV). Rambabu et al. found that the introduction of a carbon support onto a platinum black decreases the chemical shift by about 0.4 eV, suggesting that there is metal–support interaction between Pt and carbon(113).

The XPS spectra of RSDT synthesized platinum exhibits peak shifting, presence of a shoulder, and a set of secondary doublet peaks as shown in Figure 40. The first distinguishing feature of the RSDT spectrum, a strong 2 eV shift towards higher BE, is also seen with the E-Tek sample. Also, a clear contribution of a higher BE species is evidenced by a visible shoulder and highly

superposed 5/2 and 7/2 peaks. We know from TEM measurements that RSDT particles are 2-7 nm in size, as seen in Figure 22. Therefore, a size-induced shift of ~0.4 eV can be considered. As with the E-Tek catalyst, the main Pt species contributing to the XPS spectrum correspond to Pt atoms with at least 2 electrons transferred to other atoms, probably oxygen. The peaks of the higher BE species, corrected for the size-induced shift, are at ~74.5 eV for the $4f_{7/2}$ and ~77.8 eV for the $4f_{5/2}$. They correspond to the occurrence of the Pt^{4+} state (which has $4f_{7/2}$ BE of approximately 74.1 eV). In our deconvolution, no lower energy species are visible. This suggests that a superficial oxidized platinum layer exists in greater abundance on the surface of RSDT generated catalyst than compared to E-Tek particles. Both catalysts show the main Pt $4f_{7/2}$ contribution at ~72.7 eV (corrected for the particle size induced shift). This energy is higher than the same Pt $4f_{7/2}$ in $Pt(acac)_2$ – 72.1 eV. This confirms that Pt atoms on the surface of the catalysts are in a higher oxidation state than 2+.

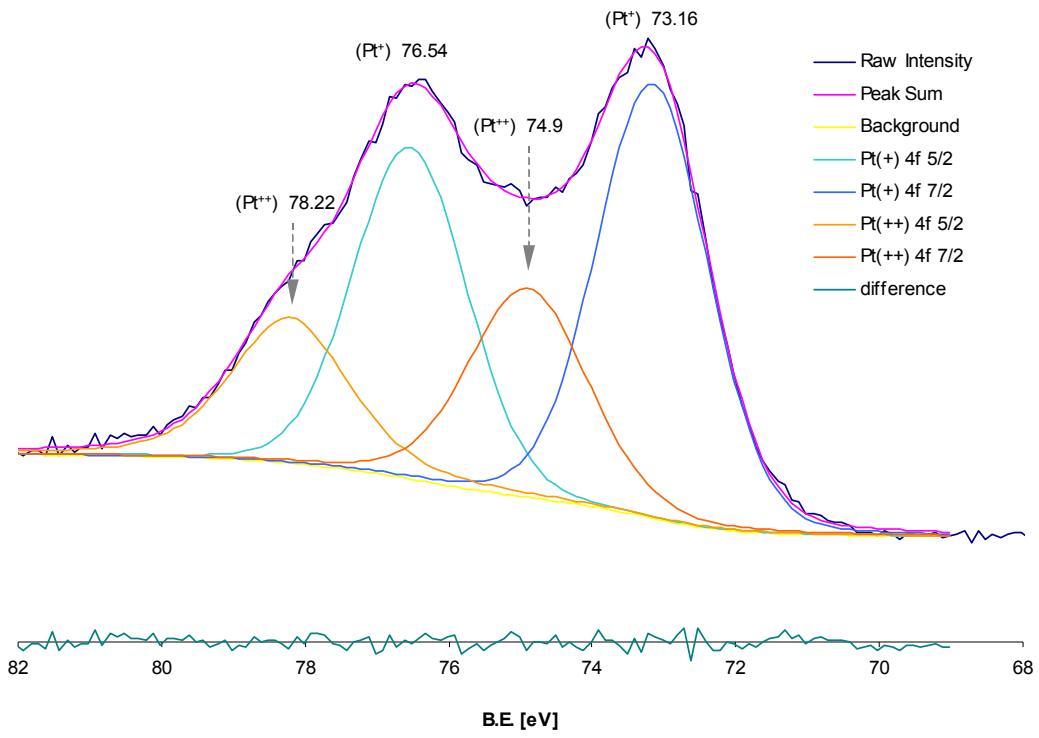

Figure 40: XPS spectrum of RSDT synthesized platinum catalyst on polyethylene.

Table 6 lists the binding energy of the $4f_{5/2}$ and $4f_{7/2}$ peaks and of the associated peaks resulting from deconvolution of individual spectra in Figure 33 - Figure 40.

	main platinum metal peak energies					***deconvoluted peak energies***			
sample	***$4f_{5/2}$ (eV)***	***$4f_{7/2}$ (eV)***	***$4f_{5/2}$ shift etched (eV)***	***$4f_{7/2}$ shift etched (eV)***		***$4f_{5/2}$ (eV)***	***$4f_{7/2}$ (eV)***	***$4f_{5/2}$ shift foil - clean (eV)***	***$4f_{7/2}$ shift foil - clean (eV)***
etched (111)	74.6	71.30							
foil - clean	74.45	71.20	-0.15	-0.1		75.72	72.43		
platinum black	75.22	71.90	0.62	0.6		76.43	72.90	0.71	0.47
40 wt.% Pt/C	75.2	71.50	0.6	0.2		76.64	73.33	0.92	0.9
platinum (acac)	75.46	72.13	0.86	0.83		76.80	73.50	1.08	1.07
PtO_2	75.3	72.30	0.7	1		77.20	73.90	1.48	1.47
RSDT	76.54	73.16	1.94	1.86		78.22	74.90	2.5	2.47

Table 6: Binding energy for electrons in the $4f_{5/2}$ and $4f_{7/2}$ of platinum on different surfaces and under different degrees of oxidation with nanoparticle samples listed in bold italic.

Examination of Table 6 shows that the effect of increased surface area leads to shifts of ~0.5-.9 eV for the high surface area platinum black and E-Tek 40 wt.% platinum on carbon samples. A meager 0.2 eV shift for the Pt $4f_{7/2}$ E-Tek 40 wt.% platinum on carbon peak appears to be the exception to this trend. The platinum (acac) shows solid shifting of 0.8-1 eV for both peak sets, while the platinum(IV) oxide shows shifting of 0.7-1.5 eV for both peak sets. The RSDT sample clearly shows the greatest amount of chemical shifting, at 1.9 eV for the main peaks and 2.5 eV for the deconvoluted set. If the 0.6 eV shifting is assumed to be related to particle size effects, and this phenomena is removed from the main peaks, and a 0.9 eV shift is compensated in the secondary peak set, then the chemical shifts become ~1.3 eV for the primary peak set and ~1.6 eV for the secondary set. This would place the chemical environment at the surface of the RSDT generated sample very near the 0.7-1 eV shift for the primary peaks and ~1.5eV deconvoluted peaks of platinum(IV) oxide. This would seem to contradict the bulk phase data obtained by x-ray diffraction, but the interaction volume of XPS is on the order of 10 nm, while the interaction volume for powder diffraction is orders of magnitude larger. The high temperature environment and oxidizing flame

conditions found in the RSDT process could conceivably oxidize the outer layers of the condensed platinum atoms as they aggregate and grow into particles. Residence time in the flame and point of quench would be interesting avenues for further research on limiting the extent of this surface oxidation.

4 Electrochemical and full cell testing of RSDT manufactured electrodes

4.1 Introduction

Ex-situ cyclic voltammetry measurements were performed on a glassy carbon electrode with platinum coated by the RSDT process in order to examine the electrochemical nature of the platinum being produced. Following this experiment a series of single cell performance tests of a traditional ternary composite electrode were performed to examine the in-cell behavior of the produced catalysts. The initial compositional and architectural design of the electrodes was chosen based on electrode development work done by the MEA Group at the NRC-IFCI.

Following the testing of more traditional electrodes a set of experiments was performed to examine how a bi-layered architecture would affect single cell performance. In these experiments, a sub-layer of platinum was deposited followed by a ternary composite layer. The thickness of each layer was varied while the other was held constant, and the samples were examined by a series of single cell tests.

4.2 Experimental procedure

A reference CV electrode made entirely of platinum was also measured. The RSDT electrode was cycled in a 0.5M solution of sulfuric acid. The voltage of the electrode was cycled from 0.04 V to 0.7 V for 10 cycles. Then the voltage was increased in 100 mV increments and the cycling was repeated until reaching a voltage of 1.5 V (the oxygen desorption limit).

Single cell testing was performed on a testing station that consists of a straight flow field geometry with a rib to channel ratio of 1.2 and an active area of 25cm^2. Sigracet SGL-24BC (SGL Group, Wiesbaden, Germany) was used as the gas diffusion medium in all experiments. SGL-24BC is a nonwoven carbon fiber 235 μm thick with one side coated with a microporous layer and treated with a 5 wt.% PTFE layer. The pre-conditioning of the cell consisted of two steps. First, the cells were heated to 80^{o}C and 100% relative humidity with hydrogen on the anode and nitrogen on the cathode at flow rates of 500 ml/min each. The cell potential was then swept from 0.05-1.2 V vs. RHE for 100 cycles at a sweep rate of 100 mV/s. Second, the cells were conditioned at 80^{o}C and100% relative humidity using hydrogen and oxygen at 1000 ml/min while the load was varied as needed to maintain as closely as possible a voltage of 0.6V for four hours. Following this break-in period the oxygen was turned off and replaced with nitrogen flowing at 500 mL/min for 15 minutes. The cathode gas circuit was then shut off and the cathode was bathed in a nitrogen atmosphere at 0 ml/min. The voltage was then swept from 0.04-0.9V at 50 mV/s. Following the cyclic voltammetry, the oxygen flow was turned back on and allowed to continue for 10 minutes. A power curve was then obtained at 80^{o}C and 100% relative humidity using hydrogen at 261 ml/min on the anode and oxygen at 625 ml/min on the cathode. Cell resistances as a function of current density (i.e., the sum of the proton-conduction resistance in the membrane and the various electronic resistances (bulk and contact resistances)) were determined using an AC perturbation of 1 kHz with a Tsuruga Model 3566 ohm-meter. The testing sequence is listed in Table 7.

Step 1 - potentiodynamic sweeps (conditioning)				
	gas	flow rate (mL/min)	relative humidity (%)	Temperature (^{o}C)
anode	H_2	500	100	80
cathode	N_2	500	100	80
	range (volts)	rate (mV/s)	# of cycles	
sweep	0.05-1.2	100	100	
Step 2 - Steady state power generation (conditioning)				
	gas	flow rate (mL/min)	relative humidity (%)	Temperature (^{o}C)
anode	H_2	1000	100	80
cathode	O_2	1000	100	80
	voltage	time (hours)	load (A/cm^2)	
conditioning	0.6	4	varied	
Step 3 - cyclic voltammetry				
	gas	flow rate (mL/min)	relative humidity (%)	Temperature (^{o}C)
anode	H_2	500	100	80
cathode	N_2	0	100	80
	range (volts)	rate (mV/s)	# of cycles	
sweep	0.04-0.9	50	3	
Step 4 - power curve				
	gas	flow rate (mL/min)	relative humidity (%)	Temperature (^{o}C)
anode	H_2	261	100	80
cathode	O_2	625	100	80
	current (A/cm^2)	time/step (min)		
power curve	0-1.2	5		

Table 7: MEA pre-conditioning protocol and testing conditions for cyclic voltammetry and power curve data generation

4.3 Results and discussion

The results of a cyclic voltammetry experiment are shown in Figure 41.

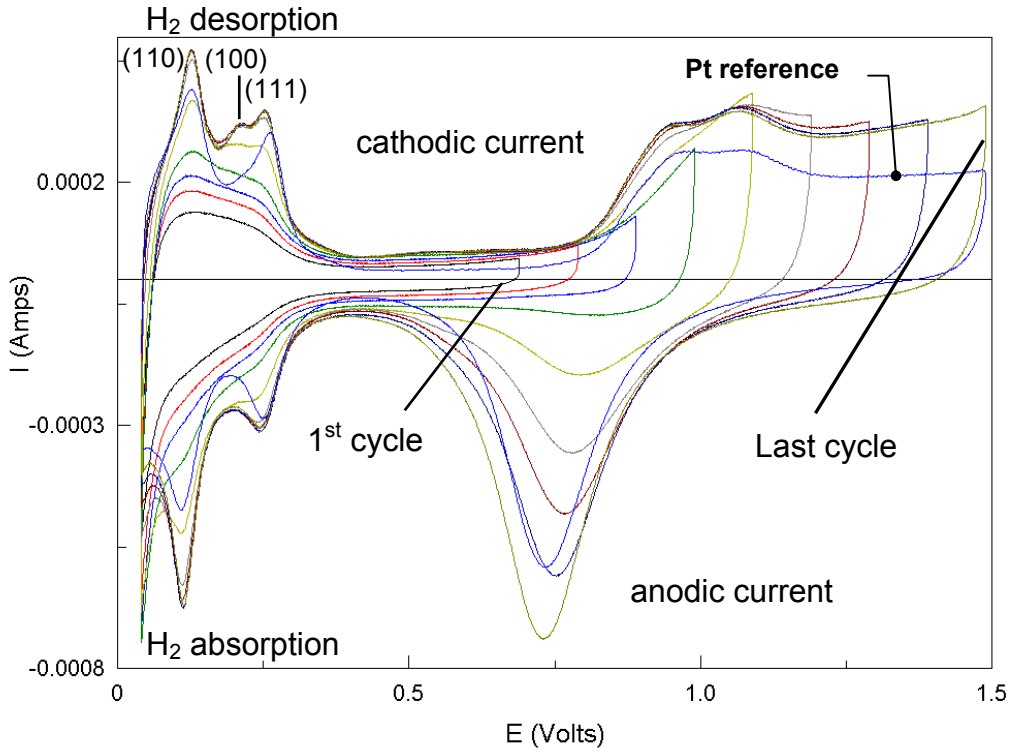

Figure 41: Ex-situ cyclic voltammetry of an RSDT generated platinum layer in 0.5 M H_2SO_4. The blue line represents the platinum reference electrode, while the black and dark yellow lines mark the 1st and last increment, respectively.

The voltage was changed in 0.1 V increments to determine if changes in the CV curve were simply due to increased wetting of the surface or if restructuring of the surface was necessary to obtain a fully active layer. If hydrophilicity is a concern, then it is expected that increased cycling would produce higher peak current between the 1st and 10th cycle of a given voltage range (i.e. overall current would increase between the 1st and 10th cycle using a range of 0.04 V – 0.7V). On the other hand, if surface restructuring is present, then the energy required would necessitate a higher peak voltage potential to achieve the

minimum activation energy required to enable physical movement of the catalyst atoms. Examination of Figure 41 reveals desorption peaks located at about 125 mV (100 plane), 200 mV (100 plane) and approximately 250 mV (111 plane). These peaks are associated with the desorption of weakly and strongly adsorbed hydrogen atoms, respectively(115).

It can be seen that a much higher preferred (100) orientation appears for hydrogen absorption on the RSDT sprayed platinum as compared to the flat platinum surface reference (shown in blue)(116, 117). The voltammogram shows that the individual features of the peaks for the RSDT sprayed sample become prominent after increasing the voltage above 1 V and this trend continues up to the 1.2 V set of cycles. Further increases in the voltage, examined to 1.5 V, in each cycling set do not appreciably increase the peak current.

Examination of individual scans between the 1^{st} and 10^{th} cycle for each voltage range did not reveal any change in the peak current values. Thus it is concluded that some type of surface restructuring is taking place with an increased energy maximum corresponding to the final voltage limit. Considering that the XPS data show evidence of a highly oxidized Pt-O interaction on the surface of RSDT sprayed samples, while the bulk phase analysis from powder diffraction exhibits the cubo-octahedral structure of platinum metal, it is possible that some restructuring of the surface is occurring to realign the surface of the catalyst particles with the underlying bulk phase. This observation suggests that a certain amount of surface conditioning is required to prime the catalyst for optimal cell performance. This requirement is accounted for in the potentiodynamic sweeps prior to steady state cell operation, listed in step 1 of Table 8. Further optimization of the cycling process is an avenue for further exploration as it is known that potential cycling causes agglomeration of the active platinum particles and thus a loss in active surface area(118).

4.3.1 Full cell testing of homogenous ternary composite electrodes made by RSDT

The composition and thickness of the first cell tested was decided upon based on internal NRC-IFCI discussions and the chosen values represent an average value of compositions commonly used at the NRC-IFCI using more traditional ink based fabrication techniques. The one exception is that the ionomer content is 18 wt.%, and this is considered at the lower end of the values needed to maintain a percolation threshold for ionic conductivity in the electrode. This low value was decided upon because mixing the ionomer and carbon together without the platinum already being supported on the carbon could effectively insulate the platinum particles from contact with carbon once introduced in the reaction plume. Deposition of platinum onto the ionomer film encased carbon support would electrically insulate the catalyst from the carbon support and this would decrease activity.

The first full cell tests of manufactured electrodes were performed using Nafion® NRE-211 electrolytes. The electrolytes are 25.4 microns thick, have a total acid capacity of >0.95 meq/g and a hydrogen crossover of <0.02 ml/(min*cm^2). The applied anodes for these tests consisted of a proprietary formulation by an industrial partner and were chosen on the basis of ease of comparison with existing data, quality control and availability. The anodes are composed of carbon, Nafion® and platinum and their formulation is listed in Table 8. The platinum loading is 0.05 mg/cm^2. The anodes were made by first screen-printing an ink onto an inert substrate such as Teflon® and then hot pressing to the Nafion® NRE-211 at 130^{o}C for 10 minutes and 2 MPa (290 psi) of pressure. The anode is 25 cm^2 (3.87 in^2) in area, so a force of 1122 lbs was applied.

Industrial partner anode specifications			
function	***material***	***Brand***	***loading (mg/cm^2)***
catalyst support material	carbon	Ketjen Black (EC-300J)	?
catalyst	platinum	proprietary	0.05
proton-conductor	perfluorosulfonic acid	proprietary	?

Table 8: Anode compositional specifications supplied by industrial collaborator.

The anode-coated electrolyte was then coated with a cathode applied by the RSDT method described in Section 2 of this thesis. The first samples to be tested were made and tested in duplicate. The composition of the cathode is shown in Table 9.

RSDT cathode composite specifications		
function	***Brand or method***	***loading (mg/cm^2)***
carbon support material	Vulcan XC-72R	0.75
platinum catalyst	RSDT	0.12
perfluorosulfonic acid	Nafion® resin	0.19
RSDT cathode composition	***unit***	***value***
total electrode area specific mass	mg/cm^2	1.06
Nafion®	wt. %	18
Vulcan XC72R	wt. %	71
platinum	wt. %	11
platinum/carbon	mass ratio	0.16
ionomer/carbon	mass ratio	0.25

Table 9: RSDT cathode specifications and composition for ternary composite electrode.

In order to examine the performance characteristics of a traditional electrode architecture manufactured by RSDT technology, a set of samples was made in duplicate with an electrode thickness of 15-20 μm, a platinum/carbon mass ratio of 0.16, and a Nafion®/carbon mass ratio of .25. The total deposition time was 100 minutes. The power curves obtained for these samples are shown in Figure 42. The sample loading was determined by inductively coupled plasma spectroscopy (ICP).

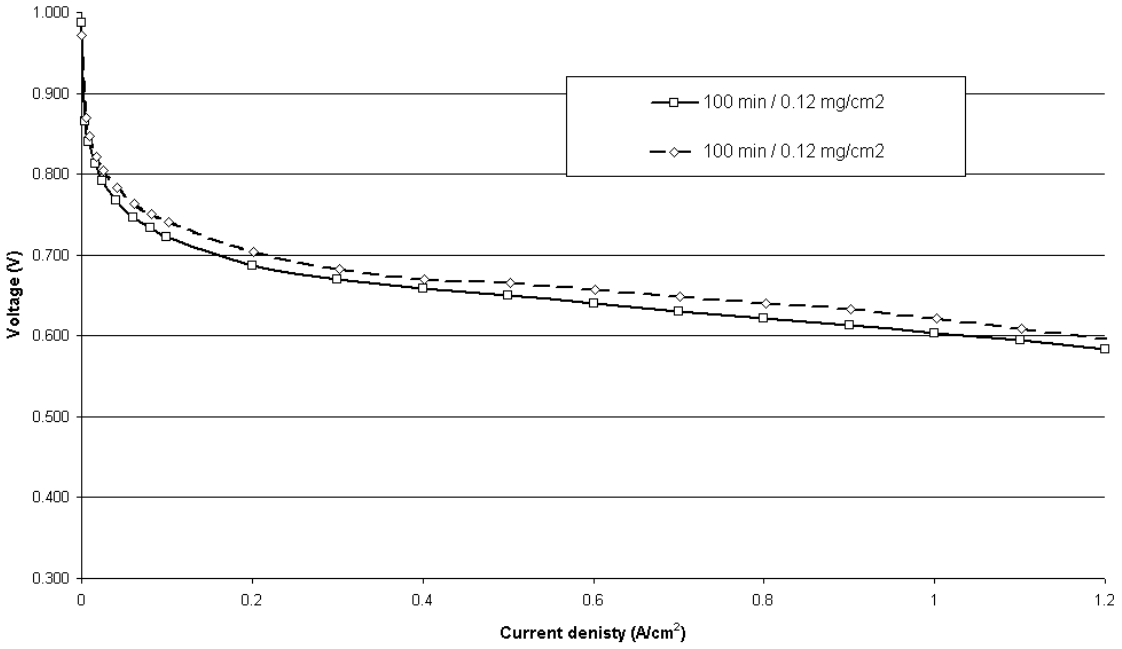

Figure 42: Power curve for 15-20 um thick ternary composite cell with a platinum/carbon mass ratio of .16, a Nafion®/carbon mass ratio of .25, and platinum loading of 0.12 mg/cm^2.

The power curves exhibit very promising performance, with OCV values near 1 V and current densities of 1.0 A/cm^2 and 1.1 A/cm^2 at 0.6 V at a platinum loading of only 0.12 mg/cm^2. It is also a very exciting considering that the performance curve represents an un-optimized deposition process. The Tafel slopes are 95.8 and 98.6 mV/dec, representing slower electrode kinetics compared to the expected 69 mV/dec value for carbon supported platinum catalysts. State-of-the-art ternary composites published by Gasteiger et al. are compared to the RSDT samples in Table 10(9).

	RSDT sample 1	*RSDT sample 2*	*GM benchmark*	*20% Pt/Vu E-Tek*	*40% Pt/Vu E-Tek*	*47% Pt/C (TKK)*	*46% Pt/C (TKK)*
Voltage at 1 A/cm^2 iR-free	0.68	0.7	0.67	0.73	0.74	0.81	0.82
Voltage at 1 A/cm^2	0.6	0.62	N/A	N/A	N/A	N/A	N/A
anode gas / cathode gas	H_2 / O_2	H_2 / O_2	H_2 / air	H_2 / O_2	H_2 / O_2	H_2 / O_2	H_2 / O_2
anode/cathode platinum loading (mg/cm^2)	0.05 / 0.12	0.05 / 0.12	0.4 / 0.4	0.15 / 0.17	0.37 / 0.38	0.4 / 0.4	0.50 / 0.51
□$_{anode}$ /□$_{cathode}$	1.4 / 5.9	1.4 / 5.9	2.0 / 2.0	2.0 / 9.5	2.0 / 9.5	2.0 / 9.5	2.0 / 9.5
pressure (psi)	ambient	ambient	21.7	21.7	21.7	21.7	21.7
platinum/carbon (mass ratio)	0.16	0.16	50	20	40	47	46
ionomer/carbon (mass ratio)	0.25	0.25	0.8	1	1	1	1
cell area (cm^2)	25	25	50	50	50	50	50

Table 10: Power curve and compositional comparisons for RSDT ternary composite cathodes, GM benchmark sample and several slot coated and hot-pressed samples using commercially available components made by Gasteiger et al. (9).

Setting aside the GM benchmark sample, the RSDT iR-free voltages at 1 A/cm^2 of 0.68 and 0.70 represent performance on par with the other four samples. However, the testing conditions for the RSDT samples are much less favorable since the data for the RSDT samples was taken at atmospheric pressure, the anode was only 0.05 mg/cm^2, the flow field for the RSDT samples was straight channel compared to serpentine channels for the others, and the cathode stoichiometry is 40% lower.

The GM benchmark, on the other hand, represents a sample with a highly optimized MEA using gas-diffusion layers (GDL) treated in-house and based on carbon fiber paper substrates (Toray, Inc., Japan). Additionally both anode and cathode GDLs were teflonated and processed using a proprietary surface treatment. The proprietary carbon-supported Pt catalysts and ionomer solutions (ca. 900 EW (equivalent weight in $g_{polymer}/mol_{H+}$) perfluorosulfonic acid (PFSA) ionomers) were used to fabricate thin-layer electrodes which were transferred via

a decal method onto 25–50 mm thick PFSA membranes with various EWs. It should be further noted that the low loading of the RSDT sample represents a 4X decrease in platinum loading over the GM benchmark. Further development related to optimization of the mass transport mechanisms is required. Testing in air to understand the loss mechanisms in the RSDT catalyst layer and MEA component selection also warrant further investigation.

4.3.2 Full cell testing of heterogeneous bi-layer electrodes

It is widely believed that one direction for electrode design is toward ultra-thin layers, meaning layers less than 500 nm(102). This serves to cut down on platinum loading and also to minimize gas diffusion and proton conduction losses. It is also believed that platinum is most active and has the highest utilization closest to the electrolyte(14). In order to investigate the possibility of improved utilization and activity, a series of electrodes were manufactured with a base layer of platinum only, onto which a ternary layer of platinum, carbon and Nafion® was added. Platinum loading was determined by spraying platinum with the secondary spray turned off onto a previously weighed blank polypropylene sample and then weighing at the conclusion of the experiment. Depositions were performed for 10, 20 and 40 minutes. The deposition rate for platinum was 8×10^{-3} mg/(cm^2-min).

platinum sub-layer deposition time (min)	*platinum - carbon - Nafion® tertiary composite deposition time (min)*			
	5	***10***	***15***	***20***
5				25 / .018 / 15
15		25 / 0.018 / 45	30 / 0.022 / 45	35 / .026 / 45
20				40 / .030 / 60
40	45 / .034 / 119	50 / .038 / 119	55 / .042 / 119	60 / .046 / 119
cell content = total time for sublayer and composite (min) / loading (mg_{Pt}/cm^2) / sub-layer thickness (nm)				

Table 11: Composition of bi-layered cathodes manufactured by reactive spray deposition, varying the thickness of the homogeneous platinum only sub-layer and the heterogeneous ternary composite layer.

Moving vertically down the columns in Table 11 represents an increasingly thicker sub-layer of platinum from 15 nm to 119 nm and a corresponding increase in loading of 0.018-0.046 mg_{Pt}/cm^2. Moving from left to right in the table holds the sub-layer thickness constant and increases the thickness of the ternary composite layer. Power curves for each sample are graphed in Figure 43-Figure 45. The testing conditions are listed in Table 7. Figure 43 represents the relationship between platinum sub-layer thickness and performance holding the ternary composite layer thickness constant. Figure 44 represents the relationship between the ternary composite layer thickness and performance holding the platinum sub-layer thickness constant at 45 nm. Figure 45 represents the relationship between the ternary composite layer thickness and performance holding the platinum sub-layer thickness constant at 119 nm.

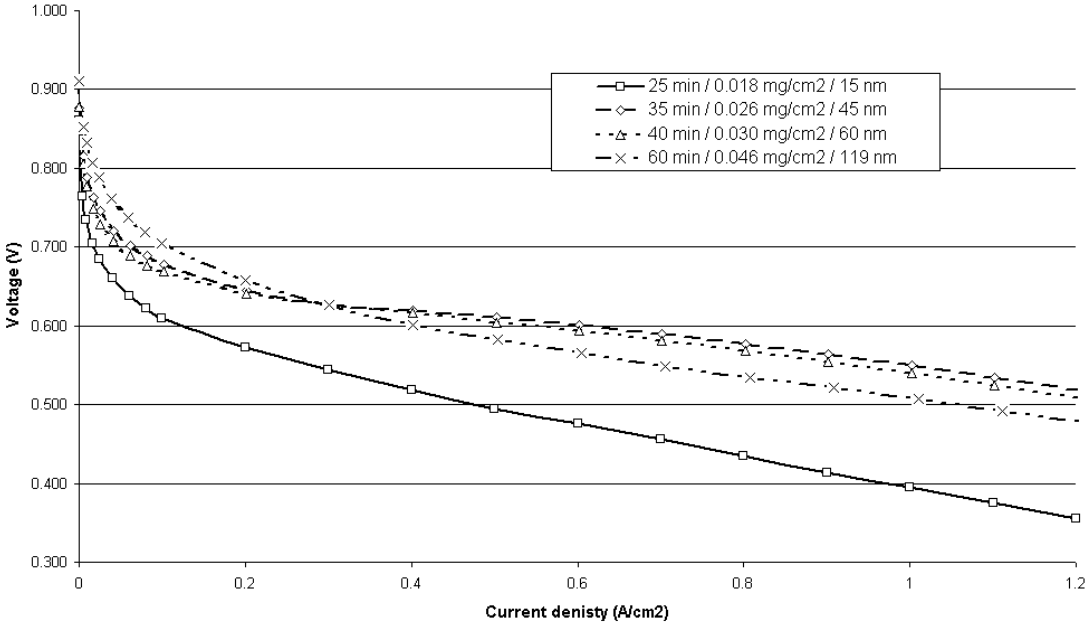

Figure 43: Power curve showing platinum sub-layer thickness effects from 15-119 nm while holding the ternary composite layer thickness constant. Legend values are total deposition time in minutes / total platinum loading in mg/cm^2 /sub-layer thickness.

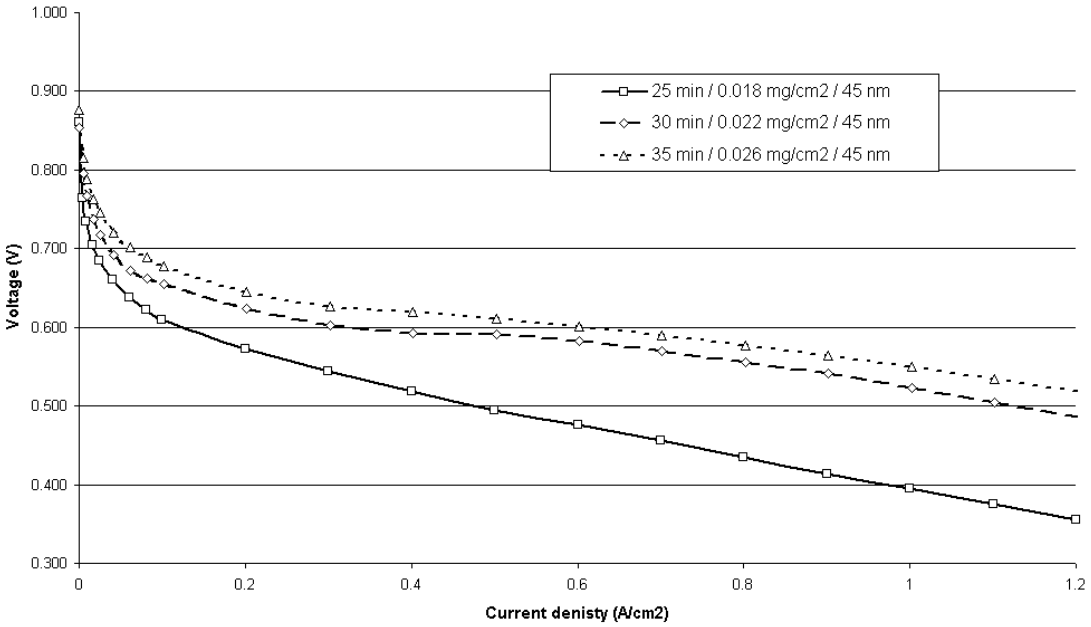

Figure 44: Power curve showing composite ternary layer thickness effects at composite deposition times of 10-20 minutes while holding the platinum sub-layer layer at 45nm. Legend values are total deposition time in minutes / total platinum loading in mg/cm^2 / sub-layer thickness.

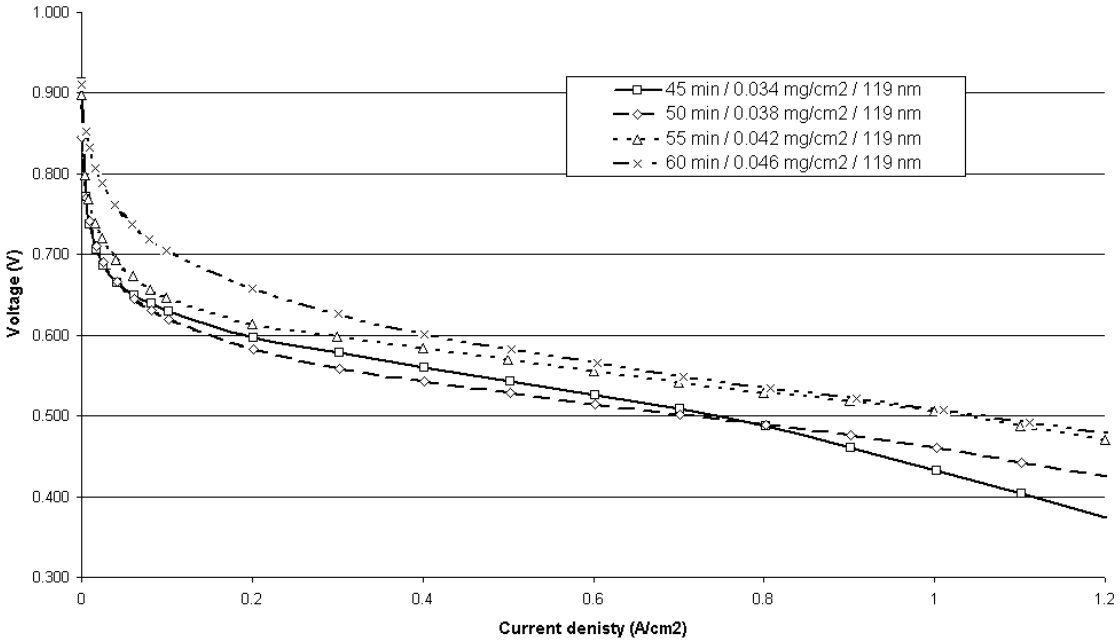

Figure 45: Power curve showing composite ternary layer thickness effects at composite deposition times of 10-20 minutes while holding the platinum sub-layer layer at 119nm. Legend values are total deposition time in minutes / total platinum loading in mg/cm^2 and sub-layer thickness.

The power curves from Figure 42 to Figure 45 have been analyzed to determine Tafel slope, current density at 0.6 V, open circuit voltage, and exchange current density. The results are listed in Table 12.

	Composite deposition time (min)	*total platinum loading (mg/cm^2)*	*open circuit voltage (V)*	*current density at 0.6 V (A/cm^2)*	*voltage at 1 A/cm^2 (V)*	*iR-free voltage at 1 A/cm^2 (V)*	*Tafel slope (mV/dec)*	*exchange current density (A/cm^2)*
	100	0.12	0.987	1.000	0.604	0.679	95.8	0.639
no platinum sub-layer	100	0.12	0.972	1.100	0.621	0.701	98.6	0.651
45 nm thick platinum sub-layer (15 min deposition time)	10	0.018	0.861	0.150	0.395	0.532	97.4	0.532
	15	0.022	0.853	0.302	0.523	0.626	115.4	0.539
	20	0.026	0.876	0.602	0.550	0.647	105.5	0.580
119 nm thick platinum sub-layer (40 min deposition time)	5	0.034	0.913	0.202	0.432	0.541	120.9	0.501
	10	0.038	0.845	0.150	0.460	0.600	116.8	0.511
	15	0.042	0.898	0.300	0.506	0.672	97.0	0.567
	20	0.046	0.910	0.402	0.507	0.670	71.2	0.684
15-119 nm thick platinum sub-layer (5-40 min deposition time)	20	0.018	0.948	0.080	0.369	0.447	131.7	0.477
	20	0.026	0.876	0.602	0.550	0.639	105.5	0.580
	20	0.030	0.879	0.502	0.540	0.631	111.0	0.558
	20	0.046	0.910	0.402	0.507	0.670	71.2	0.684

Table 12: Power curve, Tafel slope analysis, OCV and exchange current density for several RSDT electrode architectures.

The data in Table 12 show several important trends. First, the Tafel slope is reduced by an increase in composite layer loading for the 119 nm thick sub-layer, and the slope approaches the theoretical value of 69.9 mV/dec at a total loading of 0.046 mg/cm^2. The same trend holds true for the 20 min composite when increasing the sub-layer from 15-119 nm (loading 0.018 – 0.046 mg/cm^2). No linear trend is seen with the 45 nm sub-layer followed by 10-20 min composite; however, the loading values remain below 0.026 mg/cm^2. More data at loadings up to 0.05 mg/cm^2 would have been more informative for this data set. Interestingly enough, the ternary composite without any platinum sub-layer exhibits a higher Tafel slope (~98 mV/dec), even though the loading is over 2x that of the other samples. This seems to suggest that a minimum amount of platinum should be present in a sub-layer to reduce kinetic losses, and for the sub-layer architectures studied this amount appears to be approximately 0.05 mg/cm^2.

The open circuit voltages for the samples with a platinum sub-layer are also much lower (0.85 – 0.94 V) than the expected values of ~1 V. No clear trend

exists relating OCV to deposition time or loading. However, the ternary composite layers have OCVs approaching 0.97- 0.99 V. It is instructive to graph current density at 0.6 V as a function of thickness and loading values as shown in Figure 46.

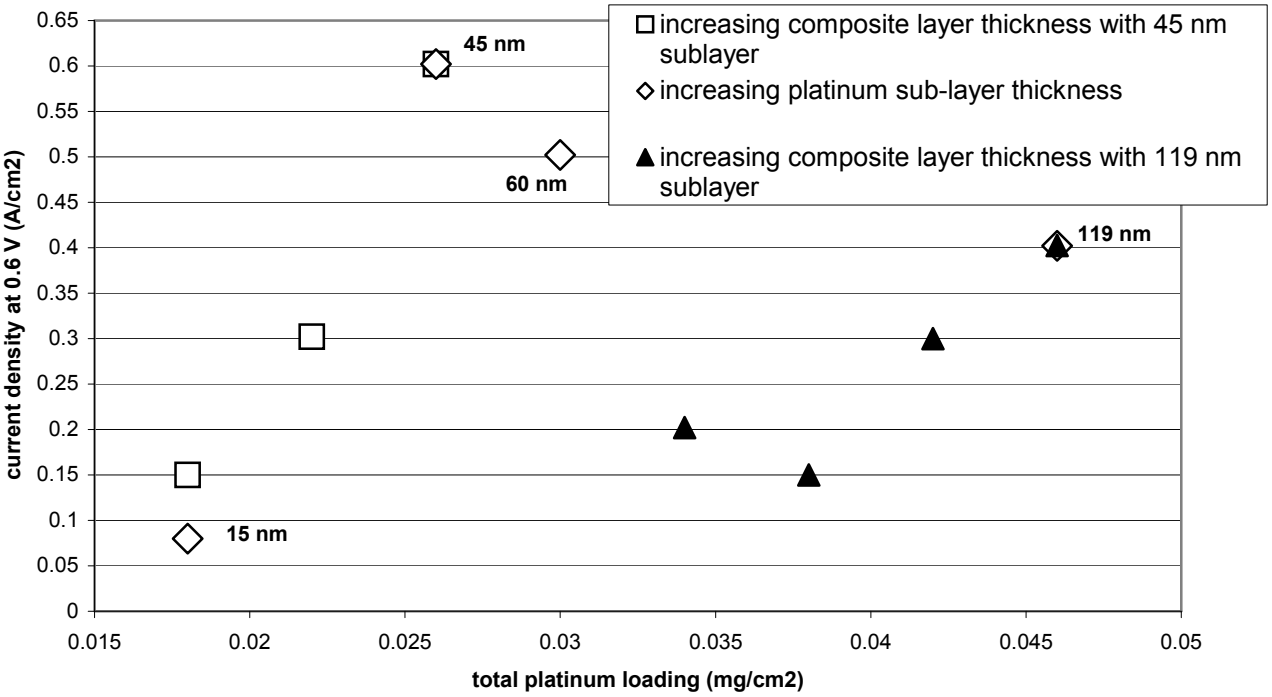

Figure 46: Current density at 0.6 V for several RSDT electrode architectures highlighting the effect of the sub-layer thickness on maximum current density.

Examination of the 45 nm sub-layer, represented as squares (□), reveals that there is a positive correlation between loading and current density up to the final data value of 0.602 V at 0.026 mg/cm^2. The same trend is appears to be present for the 119 nm thick sub-layer, represented as triangles (▲), except that a dip of 0.05 A/cm^2 is present between 0.034 and 0.038 mg/cm^2. The current density at 0.6 V is lower for the 119 nm thick sub-layer than those of the 45 nm sub-layer, irrespective of the higher loading values. It is plausible that the thicker sub-layer acts to hinder the diffusion of gasses and protons. The data for increasing the sub-layer thickness (15 – 119 nm), while holding the ternary composite layer constant (20 min) is represented by diamond shapes (◊). A very clear peak in

performance, 0.62 A/cm^2 at 0.6 V, is seen for a 45 nm sub-layer followed by a decline to 0.40 A/cm^2 at 0.6 V for the 119 nm sub-layer. This trend suggests that an optimized platinum sub-layer could be employed that offers increased platinum utilization closest to the electrolyte. The data set is limited but this optimum appears to occur at ~45 nm in platinum sub-layer thickness.

It would be instructive to examine the effects, on a bi-layered architecture, of a sub-layer that varies from 10-100 nm thick while using loadings of 0.05 – 0.2 mg/cm^2 for the composite layer. This investigation has shown that a minimum amount of platinum should be present to reduce kinetic losses and for sub-layer architectures this appears to be approximately 0.05 mg/cm^2. The OCVs for the bi-layered structures are low. There is a positive correlation between composite loading on the bi-layer and performance. Increasing the sub-layer thickness beyond an optimum serves to diminish performance and requires higher loadings for equivalent performance when examining the same composite layer thickness. Further studies at higher loading values would be instructive to examine the performance premium possible at loadings of 0.5 – 0.2 mg/cm^2.

Finally, despite less favorable Nernst and mass transport conditions, the performance of the 0.12 mg/cm^2 composite layer architecture exhibited iR-free voltages at 1 A/cm^2 of 0.68 and 0.70. The initial performance of un-optimized processing parameters and composition suggests an exciting avenue for further study.

5 Method development and preparation for systematic study

5.1 Introduction

One limitation of the previous section toward integrated physical and electrochemical method development is the lack of simultaneous data relating to a set of experimental RSDT conditions performed on the same day and under the same conditions. It is envisioned that a more complete testing plan could be developed with more than just the one sample provided by expanding the deposition area to include three samples in one run. This would allow for 3 nominally identical samples to be manufactured at the same time. This arrangement allows for two previously anode coated Nafion® electrolyte substrates and one blank polypropylene substrate. The two Nafion® electrolytes could be used for full cell testing in replicate, while the polypropylene would allow for ICP analysis, gravimetric analysis, x-ray diffraction, TEM and XPS. To this end a better understanding of the manufacturing process and the baseline repeatability was sought through examination of variance of platinum loading and carbon loading. This variance was examined by looking at intra-run variances caused by location of the sample relative to the spraying system and inter-run variances caused by sample preparation, sample mounting, and system alignment.

5.2 Experimental procedure

Square samples of polypropylene substrate were cut from a stock of 3-ring binder material (Office Depot) to use as blank substrates. The samples were weighed on a balance with 6 digits in triplicate. Three samples were placed in positions 1, 2 and 3 corresponding to the left, middle and right parts of the mask as shown in Figure 21. Each exposed mask is 25 cm^2 in area. A solution was

prepared and the RSDT conditions were set as described in Table 3. The secondary spray nozzles were turned on with isopropanol at a flow rate of 0.8 ml/min to mimic the actual spray conditions used when making ternary composite carbon, Nafion® and platinum electrodes. The carbon and ionomer were intentionally left out so that the platinum sprayed could be determined gravimetrically. The depositions were run for a total of 90 minutes, and after completion, the samples were weighed in triplicate. The experiment was repeated on three separate days. Samples are numbered according to the day they were run and the position on the mask i.e. 2M represents day two and the middle position. The platinum precursor solution was prepared on day 1 and re-used on subsequent days 2 and 3.

After the platinum experiments, a series of four carbon solutions were each prepared by placing a weighed mass of Vulcan XC-72R carbon into a beaker, adding the required amount of isopropanol, and mixing with a stir-bar for 10 minutes. The solution was then sonicated, while being stirred, using a Misonix 3000 sonicator (Misonix, Inc., Farmingdale, NY) for 30 minutes using a 2 second on and 2 second off sonicating pattern. After sonication the samples were immediately transferred to a syringe pump for deposition.

A motion program covering an area of 5 cm by 21 cm was used with linear speeds of 450 cm/min, using the same pattern described previously except for the changes to the horizontal and vertical travel as shown in Table 13.

motion program	***unit***	***value***
x distance	cm	21
y distance	cm	5
total area	cm^2	105
pattern linear distance	cm	131
nozzle speed	cm/sec	7.5
total pattern time	seconds	17

Table 13: Tabulated motion program details to accommodate three samples simultaneously.

In a separate set of experiments, the compositional analysis for several samples was determined by inductively coupled plasma optical emission

spectroscopy (ICP-OES). The method required three punches using a circular die with a diameter of ¼" (0.317 cm^2) of each sample. The punches were taken either in the lower left hand corner, the middle or the upper right hand corner. The three punches per sample are then weighed, placed in a plastic bag and mailed to Norwest Labs, Inc. (Surrey, Canada) for digestion and analysis. The digestion process involves placing the three punches per sample into aqua regia and boiling. The solution is boiled down to near dryness, more aqua regia is added, and boiled down again. After the second boiling, the remaining solution is rinsed with 10 wt.% HNO_3 and brought to 50 mL and analyzed. The results are reported in both milligrams per liter of diluted solution and milligrams of platinum per gram of sample. The samples for this set of experiments were created using the 5 cm X 21 cm motion program shown in Table 13. The only variable changed from one sample to the next was the time of deposition. The times were 23 min, 46 min, 92 min and 184 min for nominal platinum loadings of 0.0125, 0.025, 0.05 and 0.1 $mg_{platinum}/cm^2$. All RSDT samples were positioned on the right side of the three slot mask and the substrate was polypropylene.

Finally, in this section, a direct comparison is made between a GORE™ PRIMEA® Series 57 MEA with an anode/cathode loading of 0.4 / 0.4 $mg_{platinum}/cm^2$ under single cell testing conditions to an ultra-low anode/cathode loading of 0.2 / 0.05 $mg_{platinum}/cm^2$ prepared by RSDT. The cell testing protocols are identical to those listed in Table 7, except that the flow rates are 1 L/min on both the anode and cathode. Additionally, the testing station and cell hardware are different due to the fact that access to the test stations used previously ended with the conclusion of collaboration with our industrial partner. In these cell tests an ElectroChem, Inc. CompuCell GT test station was used with a TDI Dynaload single channel load bank #RBL 232 50-150-800. To compensate for the higher power rating of this load bank an Agilent power supply6651A DC 0-8V/0-50A was used to boost the overall voltage output of the test cell by 8V. The test cell was a TP-50 (Tandem Technologies, Ltd.) stand with flow field plates specially machined to mimic the straight channels used in the previous experiments. The active area is 20.9 cm^2 and the gas channel/rib area ratio is 1.2. Cell resistances

as a function of current density (i.e., the sum of the proton-conduction resistance in the membrane and the various electronic resistances (bulk and contact resistances)) were determined using an AC perturbation of 1 kHz with a Tsuruga Model 3566 ohm-meter.

5.3 Results and discussion

The results of the platinum loading tests are tabulated in Table 14.

sample #	average blank polypropylene mass (mg)	variance blank polypropylene (mg)	average sprayed polypropylene mass (mg)	variance sprayed polypropylene (mg)	mass sprayed platinum (mg)	platinum loading (mg/cm^2)	platinum loading rate (mg/cm^2-min)
1L	334.23	0.05	335.31	0.03	1.07	0.043	4.8E-04
1M	312.34	0.02	313.64	0.03	1.30	0.052	5.8E-04
1R	338.16	0.03	339.20	0.02	1.05	0.042	4.7E-04
2L	339.92	0.02	341.12	0.02	1.20	0.048	5.3E-04
2M	342.97	0.02	344.41	0.03	1.44	0.058	6.4E-04
2R	331.21	0.02	332.45	0.03	1.24	0.049	5.5E-04
3L	321.35	0.03	322.46	0.01	1.11	0.045	4.9E-04
3M	350.19	0.01	351.57	0.01	1.38	0.055	6.1E-04
3R	338.97	0.02	340.17	0.01	1.20	0.048	5.3E-04

Table 14: Platinum loading results for RSDT conditions as described in Table 3 for 90 minutes. L = left position, M = middle position, R = right position and 1-3 represent the day on which the experiment was performed.

Table 14 shows that approximately 1.1 – 1.4 mg of platinum is deposited on each 25 cm^2 mask area. This corresponds to loadings in the range of (0.043 – 0.058 $mg_{platinum}/cm^2$) and a platinum deposition rate of ~5-6x10^{-4} $mg_{platinum}/(cm^2$-min). The intra-run platinum averages were compared to the positional averages to examine the source of variances. Inter-run variance refers to the variance observed between positions 1-3 for a single experiment. Nominally, these three samples should be identical. Intra-run variance refers to variance observed with nominally identical experimental conditions performed on a different day. Averages per day are represented as P1, P2 and P3 representing platinum day 1, day 2 and day 3 respectively. The same analysis was performed for the same

position PL, PM and PR on the mask but different days representing left, middle and right. The results are shown in Table 15.

Day or position	*Average platinum loading per run (mg/cm^2)*	*variance platinum loading per run (%)*	*Average platinum loading rate per run (mg/cm^2-min)*	*variance platinum loading rate per run (%)*
P1	0.046	12.1	5.06E-04	12.1
P2	0.052	9.7	5.74E-04	9.7
P3	0.049	16.3	5.47E-04	16.3
PL	0.045	5.6	5.01E-04	14.8
PM	0.055	5.4	6.10E-04	9.6
PR	0.046	8.7	5.16E-04	11.6

Table 15: Platinum loading results examined as averages based on intra-run and positional variances

Table 15 shows two trends. The first trend is that the variance is relatively constant from day to day on a given position. This is reflected by the narrow variance spread of 5.30×10^{-3} to 5.49×10^{-3} $mg_{platinum}/cm^2$ (10-12 standard deviation percentage, %σ). The second trend is that there is a much higher variance between the left, middle and right positions on the mask, as evidenced by an increasing variance moving from 2.52×10^{-3} $mg_{platinum}/cm^2$ (6 %σ) on the left position to 4.03×10^{-3} $mg_{platinum}/cm^2$ (8.8 %σ) on the right position. However, it is also interesting that the inter-day runs (PL-PR) have a smaller variance magnitude but a larger variance spread, while the intra-day variances (P1-P3) exhibit a larger variance magnitude and a smaller spread. This suggests that the positional variance needs to be better addressed by possible modification of the rastering program for better coverage. A longer rastering travel length could achieve reduction of the variance. However, this would increase deposition time and decrease the platinum loading rate. Currently the mask covers three 5 cm X 5 cm slots that total 21 cm in width when including the separation between samples. The motion program is 5 cm vertical X 21 cm horizontal traverse and so the center of the spray passes over each spot on the three masks. The spray

area is approximately circular and is 5-6 cm in diameter; therefore, an additional 2.5-3 cm of horizontal and vertical travel, at each end, would allow for the entire spray area to pass over every exposed portion of the samples. A rastering program of 11 cm vertical X 27 cm horizontal would achieve this goal.

The same procedure was repeated for determination of the carbon loading, except this time the platinum II, IV pentanedionate was left out of the precursor solution. The other difference was that the carbon solution was made separately each day with different carbon concentrations. The carbon is notoriously difficult to measure as it has a tendency to cling to surfaces and disperse readily with electrostatic fluctuations or even the slightest airflow over its surface.

sample #	carbon slurry concentration (mg/ml)	average blank poly-p mass (mg)	variance blank poly-p (mg)	average sprayed poly-p mass (mg)	variance sprayed poly-p (mg)	mass sprayed carbon (mg)	carbon loading (mg/cm^2)	carbon loading rate (mg/cm^2-min)
C1L	0.600	338.13	0.006	343.51	0.006	5.37	0.215	2.39E-03
C1M		338.78	0.006	344.99	0.010	6.21	0.249	2.76E-03
C1R		333.39	0.012	339.52	0.006	6.13	0.245	2.72E-03
C2L	0.145	336.76	0.010	338.85	0.000	2.09	0.084	9.29E-04
C2M		335.52	0.006	337.06	0.015	1.55	0.062	6.87E-04
C2R		335.25	0.006	336.86	0.006	1.61	0.064	7.16E-04
C3L	0.055	333.95	0.006	335.88	0.029	1.94	0.077	8.61E-04
C3M		342.52	0.006	343.93	0.046	1.41	0.056	6.27E-04
C3R		340.45	0.012	341.46	0.038	1.01	0.040	4.49E-04
C4L	0.211	255.38	0.012	257.26	0.006	1.88	0.075	8.36E-04
C4M		259.62	0.006	261.26	0.006	1.64	0.066	7.29E-04
C4R		250.85	0.023	252.54	0.006	1.70	0.068	7.54E-04

Table 16: Carbon loading results for RSDT conditions as described in Table 3 with three Vulcan XC-72R slurry concentrations and a liquid flow rate of 0.8 ml/min for 90 minutes. Note: poly-p = polypropylene blank

Due to the design of the carbon loading experiment only the intra day averages could be examined, as the concentration was changed each day. Table 16 shows that except for C1, the left most mask receives the most carbon, and this could be explained by a misalignment in the centering of the slurry spray that

puts the spray off-center. The intra-run loading averages for each day were then calculated as well as the corresponding carbon deposition rate, as shown in Table 17.

Day	*carbon slurry concentration (mg/ml)*	*Average carbon loading per run (mg/cm^2)*	*variance carbon loading per run (mg/cm^2)*	*standard deviation percentage (σ %)*	*Average carbon loading rate per run (mg/cm^2-min)*	*variance carbon loading rate per run (mg/cm^2-min)*
C1	0.600	0.236	1.85E-02	7.8	2.62E-03	2.06E-04
C2	0.145	0.070	1.19E-02	17.0	7.77E-04	1.32E-04
C3	0.055	0.058	1.86E-02	32.0	6.45E-04	2.07E-04
C4	0.211	0.070	5.02E-03	7.2	7.73E-04	5.58E-05

Table 17: Carbon loading results examined as averages based on intra-run variances

The variance for carbon loading (intra-run) is relatively steady for the first three days C1-C3 at 1.2-1.8 mg_{carbon}/cm^2 and was exceptionally low on the fourth day. However, the variance as a percentage of total loading varies considerably from 7-32%. It is also important to note that the slurry inks made with the highest carbon slurry concentrations, C1 (0.600 mg_{carbon}/ml_{ipa}) and C4 (0.211 mg_{carbon}/ml_{ipa}), show lowest standard deviation percentages. This makes sense because heavier, hence thicker, samples have more material mass to average out the inconsistencies while lighter, hence thinner, samples have less material. This suggests that more consistent spray alignment and accurate weighing is crucial at lower loading compositions. This point is especially important as future electrode architectures are inevitably going to be thinner to decrease mass transport losses(9). Furthermore, the data suggest that weighing and transferring a larger amount of carbon, increasing the batch size, could minimize weighing associated errors.

The limitation of the gravimetric method for platinum determination is that it does not allow for spatial resolution of the loading and can only be used on polypropylene and without Nafion® and carbon. It cannot be used for platinum determination on humidity sensitive membranes because the changes in

humidity before and after deposition can cause the mass to change above or below the deposited platinum mass. Earlier attempts at using thermal gravimetric analysis (TGA) were unsuccessful for low loadings below 0.2 mg/cm^2. This was partially due to the how impractical it was to get enough punches for a viable signal and partially because during thermal decomposition the samples would melt in a way that would either cause sizeable portions to fall out of the weighing cylinder or would touch the sample thermocouple and ruin the mass measurement. A single ¼" punch for a 0.05 $mg_{platinum}/cm^2$ sample would only yield 0.013 mg per sample. The resolution for the instrument was only 0.01 mg, so that roughly 10 times (10 punches) would be required, and 20 times that for 0.025 $mg_{platinum}/cm^2$. These limitations and the associated sample preparation time made this method unacceptable for routine platinum determination on Nafion® membranes and on ultra low loadings of 01 $mg_{platinum}/cm^2$ and below.

Inductively coupled plasma optical emission spectrometry is a well-established technique for trace metals analysis. Therefore, ICP analysis was performed on a set of samples deposited with nominally calculated platinum loadings of 0.0125, 0.25, 0.5 and 0.1 $mg_{platinum}/cm^2$. Additionally, a sample anode manufactured by a traditional spray processing technique (with a known loading), and a commercially available GORE™ PRIMEA® Series 57 MEA were also analyzed for comparison. The anode had a nominal loading of 0.4 $mg_{platinum}/cm^2$ and the Gore 57 a nominal loading of 0.8 $mg_{platinum}/cm^2$. It should be noted that the GORE sample has both an anode and a cathode coating on their proprietary membrane and the ICP analysis will only provide the combined loading. The anode manufactured by a spray method is coated on a Nafion® NRE-211 membrane. The results for these tests are shown in Table 18.

nominal loading (mg/cm^2)	*sample or spatial position*	*mass of 3 punched samples (g_{sample})*	*mass specific ICP analysis (mg_{pt}/g_{sample})*	*vol. spec. ICP analysis (mg_{pt}/L)*	*ICP loading by mass (mg/cm^2)*	*ICP loading by volume (mg/cm^2)*
0.8	Gore G57	0.00720	108	16.4	0.818	0.863
0.4	anode	0.01411	28.6	8.0	0.425	0.421
0.0125	M	0.00559	1.8	0.2	0.011	0.011
0.0125	UR	0.00553	1.3	0.1	0.008	0.005
0.025	M	0.00579	4.7	0.5	0.029	0.026
0.05	LL	0.00571	10.7	1.1	0.064	0.058
0.05	M	0.00574	9.44	1.1	0.057	0.058
0.05	UR	0.00560	7.5	0.8	0.044	0.042
0.1	M	0.00622	18.7	2.2	0.122	0.116

Table 18: Results of ICP analysis on RSDT samples with nominal loadings of 0.0125 – 0.1 $mg_{platinum}/cm^2$, a reference anode made by a spraying technique and a GORE G57 MEA. M = middle, UR = upper right and LL = lower left to designate the location of the punches on each sample.

Several results should be noted. First the ICP platinum concentration is determined by taking a sample, digesting in aqua regia and then bringing the contents of the digestion to 50 mL in a volumetric flask with 10 wt. % HNO_3. This solution is then analyzed with the ICP instrument by pumping the solution with a peristaltic pump into a nebulizer and then passing the spray into an argon plasma to dissociate the sample into its constituent atoms or ions, which excites them to a level where they emit light of a characteristic wavelength. ICP-OES is a fast multi-element technique with a dynamic linear range and moderate-low detection limits (~0.2-100 ppb). Norwest Labs, Inc. reports results as both mass specific ($mg_{platinum}/g_{sample}$) and volume specific ($mg_{platinum}/g_{sample}$) concentrations. The mass specific concentration normalizes the platinum mass to the total sample mass of the three punches. Any error in the weighing would inject error into the final loading reported by mass specific concentration. Alternatively, the volume specific loading does not incorporate any weighing error into the reported values. It does, however, require that the final volume of the sample be accurate, and this is achieved through the use of volumetric glassware. A comparison of the

differences in the two reported values as well as the percent difference based on the volume specific values is tabulated in Table 19.

nominal loading (mg/cm^2)	*sample or spatial position*	*difference loading by mass - volume (mg/cm2)*	*% difference ICP_{volume} to nominal (mg_{pt}/cm^2)*
0.8	Gore G57	-4.46E-02	7.9
0.4	anode	3.73E-03	5.3
0.0125	M	6.53E-05	-15.8
0.0125	UR	2.30E-03	-57.9
0.025	M	2.33E-03	5.3
0.05	LL	6.42E-03	15.8
0.05	M	-8.57E-04	15.8
0.05	UR	2.11E-03	-15.8
0.1	M	6.65E-03	15.8

Table 19: Comparison of volume specific and mass specific loading values determined by ICP and examination of the percent difference of the reported values from the nominal value. LL = lower left, M = middle and UR = upper right.

The mass specific platinum loading values tend to be larger in magnitude than the corresponding volume specific measurements, as most of the values in column 3 of Table 19 are positive. The differences between the two methods of reporting the mass are <10% except for the upper right (UR) sample from the nominal .0125 $mg_{platinum}/cm^2$ sample, where it is 36% higher by mass specific loading. In general, the sample platinum loadings are within 16% of the nominal value. As before, this difference is greater at lower loadings, and the upper right sample of the nominal .0125 $mg_{platinum}/cm^2$ sample is almost 60% lower than expected.

Referring back to Table 18, examination of the loading for the GORE™ PRIMEA® Series 57 MEA and the anode compared to the nominal values using the volume specific values shows that the ICP loadings are slightly higher than expected at 7.8% and 5.3% respectively. No further positional analysis was performed on these samples due to the cost of analysis ($60 CDN/sample).

One trend that is immediately obvious is seen on the nominally 0.05 $mg_{platinum}/cm^2$ sample. For this sample, a series of three punches was taken in

the lower left (LL), middle (M) and upper right (UR) corner of the sample. The upper right value is approximately 27% lower in loading (.042 versus .058 $mg_{platinum}/cm^2$). Examination of the nominally 0.0125 $mg_{platinum}/cm^2$ sample shows that the middle sample is 50% higher in loading compared to the upper right sample (.005 versus .011 $mg_{platinum}/cm^2$). The samples for the ICP study occupy the right slot in the mask, shown in Figure 21, and there was evidence of a larger variance for platinum and carbon loading at this position (R) in the previous study using gravimetric methods. This further confirms that a modified motion program should be adopted to even out the inconsistencies in platinum and carbon deposition.

In order to directly compare the GORE™ PRIMEA® Series 57 MEA sample under single cell testing conditions to an ultra-low loading sample prepared by RSDT, two power curves were run using the GORE™ PRIMEA® Series 57 described in the ICP analysis section and the nominally 0.05 $mg_{platinum}/cm^2$. The average loading of the 0.05 $mg_{platinum}/cm^2$ samples is 0.053 $mg_{platinum}/cm^2$. The results for this comparison are shown in Figure 47.

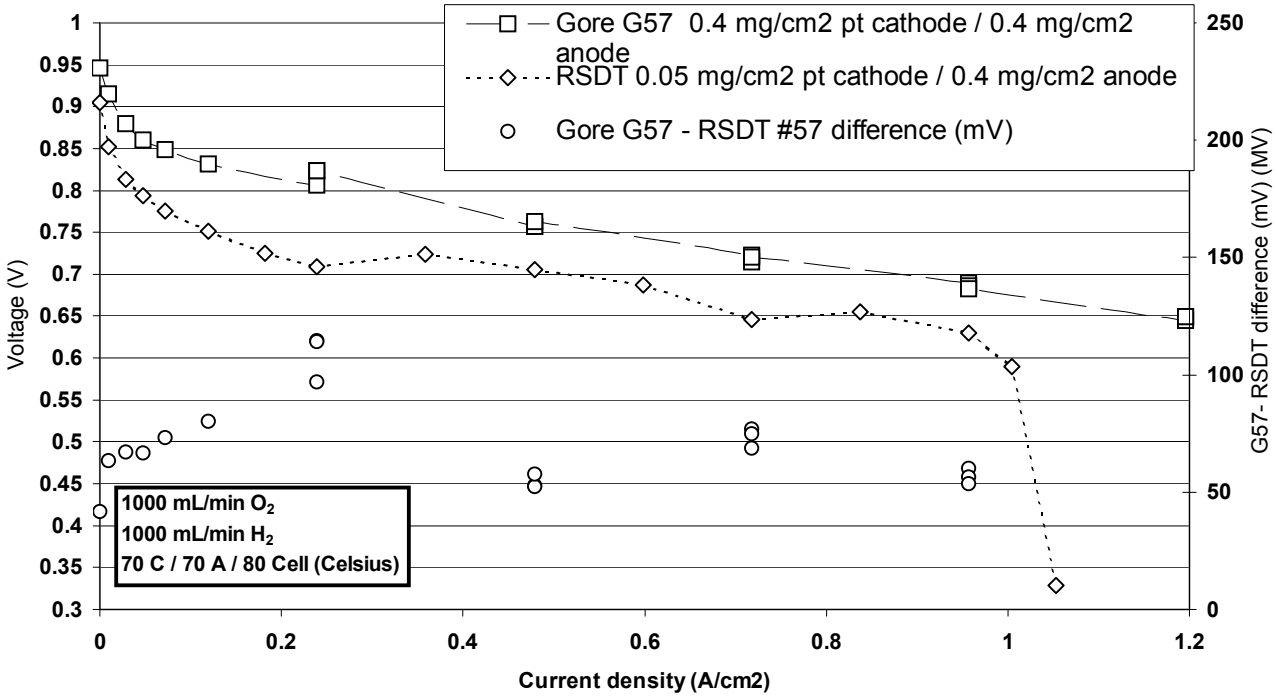

Figure 47: Power curves for a GORE™ PRIMEA® Series 57 MEA anode / cathode (0.4 / 0.4 $mg_{platinum}/cm^2$) with an RSDT manufactured cathode and an anode sprayed by a traditional processing method anode/cathode (0.42 / 0.053 $mg_{platinum}/cm^2$) under identical testing conditions.

The various performance metrics for the polarization curves in Figure 47 are tabulated in Table 20.

	total platinum loading (mg/cm^2)	*open circuit voltage (V)*	*voltage at 1 A/cm^2 (V)*	*iR-free voltage at 1 A/cm^2 (V)*	*Tafel slope (mV/dec)*	*mass specific power at 1 A/cm^2 (g_{pt}/kW)*	*area specific power at 1 A/cm^2 (W/cm^2)*
Gore G57	0.86	0.946	0.686	0.860	65.4	1.25	0.686
RSDT	0.473	0.905	0.629	0.773	75.8	0.75	0.629

Table 20: Power curve metrics comparison of a GORE™ PRIMEA® Series 57 MEA anode / cathode (0.4 / 0.4 $mg_{platinum}/cm^2$) with an RSDT manufactured cathode and an anode sprayed by a traditional processing method anode/cathode (0.42 / 0.053 $mg_{platinum}/cm^2$)

The Tafel slope for the RSDT sample shows improvement over the ~95 mV/dec observed for the 0.12 mg/cm^2 RSDT samples in Table 12, and this indicates a slight improvement in the kinetic activity of the electrode. However, it should be noted that the OCV is approximately 70 mV lower for the 0.053 $mg_{platinum}/cm^2$ electrode compared to the 0.12 mg/cm^2. The RSDT sample in Table 20 performs about 50 mV lower than the Gore G57 membrane over then entire range, and this is roughly equal to the difference in OCV between the two samples of 41 mV. However, the loading on the cathode is 8 times lower for the RSDT sample compared to the GORE G57 sample. The high frequency resistance for both samples suggests that the test cell exhibits a relatively high ohmic resistance of ~7 mOhm and it is known by the author that other test stands used at NRC-IFCI have lower resistances of ~3-4 mOhm.

Current state of the art single cell performance (with H_2/air at 80^{o}C) is 0.7 W/cm^2 at 0.68 V (58% energy conversion at 1.03 A/cm^2), corresponding to 0.85-1.1 g_{pt}/kW (0.59-0.77 mg_{Pt}/cm^2)(9). According to the DOE, market penetration will require platinum specific power density reduced to 0.2 g_{pt}/kW at >0.65 V (0.3 mg_{Pt}/cm^2)(10). The samples tested fall short of the DOE targeted platinum specific power density, but this value could be improved by optimization of the diffusion media, use of serpentine flow channels and appropriate water management. Considering that state of the art platinum specific power densities are 0.85-1.1 g_{pt}/kW at total MEA platinum loadings of 0.59-0.77 $mg_{platinum\ total}/cm^2$, it is conceivable that a 0.7 $g_{platinum\ total}$/ kW mass specific power density at a total platinum loading of 0.47 $mg_{platinum\ total}/cm^2$ is achievable. Table 20 shows that the RSDT sample achieved a mass specific power density of 0.75 $g_{platinum\ total}$/ kW and an area specific power density of ~0.63 W/cm^2. These values are still 7% high and 10% low respectively. Additionally, the oxidant was oxygen and not air. However, if one considers that optimized anodes can be brought to platinum loadings as low as 0.05 mg/cm^2 with minimal polarization losses, incorporating thinner electrode layers, and utilizing novel architectures that increase platinum

utilization, then the prospect of attaining DOE targets utilizing RSDT technology represents an exciting area for further research.

6 Conclusion

6.1 Summary

The research described above represents the preliminary stages of inquiry into the development of the Reactive Spray Deposition Technology process for direct CCM manufacture of carbon supported platinum catalysts for PEM fuel cell applications. Modification of the conventional RSDT system by introduction of a quenching system and a secondary spray system, and the adoption of suitable process parameters allows for the direct deposition of platinum directly onto substrates at surface temperatures as low as 100^{o}C. The RSDT system was designed and built in-house at the NRC-IFCI and a formal patent is in the prosecution stage based on these developments.

Transmission electron microscopy showed that tiny particles, most less than 10 nm, are indeed produced using an un-optimized set of conditions. Phase analysis confirms that the bulk phase of the formed catalyst is platinum metal, and higher deposition temperatures (without the quench) encourage larger particle sizes and grain growth at temperatures of 220^{o}C and above. Above this temperature a shiny film of platinum metal can be deposited by simply placing a substrate into the reaction plume. Surface analysis by XPS seemed to contradict the bulk phase data obtained by x-ray diffraction. However, it is surmised that the bulk of the catalyst is indeed platinum metal, while the outer layer consists of a shell of a highly oxidized platinum species. The residence time of the un-sublimated platinum vapors, the location of sublimation, flame temperature, and relative oxidative strength of the flame likely control the extent of this oxidized shell. Cyclic voltammetry confirms that there appears to be surface restructuring and the extent of this restructuring is related to the peak voltage but this effect plateaus at 1.2 V.

Incorporation of a quenching system and directly depositing onto various substrates and analyzing by TEM showed that thin platinum sub-layers of 15-150 nm could be deposited and that the sub-layer morphology does not appear dense, but rather as a collection of closely packed aggregates of platinum 10-20 nm in diameter. Further incorporation of a secondary slurry spraying system allowed the independent introduction of carbon and Nafion® into the plume of platinum vapors. Ternary composite layers of platinum, Nafion®, and carbon of 3.5 to 5.5 μm in thickness were fabricated and characterized. Additionally, bi-layers consisting of a platinum sub-layer and a ternary composite layer were manufactured and imaged by TEM. The ability to decouple the carbon and Nafion® in real processing time represents a breakthrough in processing capability.

Initial cell tests of a ternary composite cathode by RSDT with a loading of 0.12 $mg_{platinum}/cm^2$ showed very promising performance with OCV values near 1 V and current densities of 1.0 A/cm^2 and 1.1 A/cm^2 at 0.6 V. The samples exhibited iR-free voltages at 1 A/cm^2 of 0.68 (0.60 V with iR) and 0.70 V (0.62 V with iR). These results are also very exciting considering that the performance curve represents an un-optimized deposition process. The Tafel slopes are 95.8 and 98.6 mV/dec, which represents slower electrode kinetics compared to the expected 69 mV/dec value for carbon supported platinum catalysts.

An experimental study of the effect of sub-layer and ternary composite layer thickness on a bi-layered structure showed that a minimum amount of platinum should be present to reduce kinetic losses, and for sub-layer architectures this amount appears to be approximately 0.05 mg/cm^2. There is a positive correlation between composite loading on the bi-layer and performance. Increasing the sub-layer thickness beyond an optimum serves to diminish performance and requires higher loadings for equivalent performance when examining the same composite layer thickness, which may be related to difficulty in proton mobility across an ionic insulating layer.

Finally, a set of loading tests was performed for platinum and carbon using an expanded motion program so that several samples could be deposited in one

deposition to investigate sources of variance in the process. For platinum it was found that the variance is relatively constant from day to day at a given position on the mask but that there is a much higher variance between the left, middle and right positions on the mask. The inter-day runs have a better variance spread, but the intra-day positional variances are smaller in magnitude. This suggests that the positional variance needs to be better addressed by possible modification of the rastering program for better coverage. An 11 cm X 27 cm rastering program would be a good start considering that the spray pattern has a ~3 cm radius.

For the carbon loading it was found that a more consistent spray alignment and accurate weighing is crucial at lower loading compositions. This point is especially important as future electrode architectures are inevitably going to be thinner to decrease mass transport losses. Furthermore, the data suggest that weighing and transferring a larger amount of carbon, increasing the batch size, could minimize weighing associated errors.

An investigation of platinum loading by ICP confirmed the positional variances in platinum loading and suggests that the upper right corner is getting up to 27% less platinum compared to the middle and lower left areas. This confirms the need to redesign the spraying pattern for better uniformity. Comparisons of the ICP results with other samples of known nominal platinum loading confirm that the method works. It was determined that TGA analysis was not adequate for platinum determination of samples with low platinum loading.

Finally, cell voltages of 0.60 V at 1 A/cm^2 using H_2/O_2 at a loading of 0.053 $mg_{platinum}/cm^2$ have been achieved. The architecture for this sample was an un-optimized ternary composite layer. The 0.7 $g_{platinum\ total}$/ kW platinum specific power density using a total platinum loading of 0.47 $g_{platinum\ total}/cm^2$ represents a promising avenue for further development. Considering that optimized anodes can be brought to platinum loadings as low as 0.1 mg/cm^2 with minimal polarization losses makes the development potential for RSDT manufactured electrodes even more exciting.

6.2 Recommendations for future work

Based on the data generated in this thesis, it seems clear that a better understanding of the particle size and distribution of platinum particles at various quench positions and geometries should be further quantified for the current deposition conditions. The presence of a visible spread in the catalyst particle size in this thesis suggests that much room for improvement is possible to narrow the distribution. Considering that a narrow window of optimal diameter is 2-5 nm then conditions that favor monodisperse platinum should be researched to improve the mass specific power density. A better understanding of the oxide shell on the platinum particles and the conditions that favor or retard this layer would be interesting as well as supportive cyclic voltammetry data. This surface oxidation study could be integrated into a parametric study of RSDT process conditions along with the particle size. Limitations with the current quench system may be addressed by enclosing the entire process plume in a shroud and/or the use of a circular quench. Furthermore, a humidified quench gas would have a higher heat capacity and may allow for a more uniform quench zone and stop the reaction/agglomeration faster.

A better understanding of the repeatability of the process would be instructive as well as lay the groundwork for further exploration of compositional optimization of the Nafion®, carbon and platinum in the ternary composite layer. The RSDT process is also an incredibly flexible processing technique, and since the platinum loading is decoupled from the carbon loading, a thinner electrode structure of 1 um and below should be examined for the ternary composite architecture as well as with the bi-layer architecture. Integrated with this reduction in thickness should be a study with increased loading values for bi-layer electrodes to examine the performance premium possible at loadings of 0.5 – 0.2 mg/cm^2.

It is also recognized by this author that carbon corrosion and platinum agglomeration represent existential threats to the widespread introduction of fuel cells for automotive applications. It would be an important parallel step to

examine if there is any benefit to the RSDT process that retards agglomeration of the catalyst particles due to the higher energy conditions present in the reaction plume during platinum deposition on the carbon support. Alternate catalysts and supports such as TiO_2-Pt could conceivably be produced quickly using suitable organo-metallic precursors of titania and platinum in the same solution.

Reference list

(1) Hearing on sustainable, low emission, electricity generation: of the House Comm. on US Senate Committee on Energy and Natural Resources, R.Smalley, (Apr 27, 2008).

(2) International Energy Agency. World Energy Outlook 2006. OECD/IEA; 2006.

(3) US Climate Action Parternership. A Call for Action. 2007 Jan 22.

(4) Amy Taylor, Mark Winfield, Matthew Bramley. Government Spending on Canada's Oil and Gas Industry: Undermining Canada's Kyoto Commitment. 2008 Jan 31.

(5) Bar-On I, Kirchain R, Roth R. Technical cost analysis for PEM fuel cells. Journal of Power Sources 2002 Jun 15;109(1):71-5.

(6) Tsoskounoglou M, Ayerides G, Tritopoulou E. The end of cheap oil: Current status and prospects. Energy Policy 2008 Oct;36(10):3797-806.

(7) Rebecca Osakwe. PEM Fuel Cells and Russia's Supply of Platinum Trading one bottleneck for another? Stanford Student Journal of Russian, East European and Eurasian Studies 2006;2(Spring 2006).

(8) Carlson E. Precious Metal Availability and Cost Analysis for PEMFC Commercialization. 2003. Report No.: DE-FC04-01AL67601.

(9) Gasteiger HA, Kocha SS, Sompalli B, Wagner FT. Activity benchmarks and requirements for Pt, Pt-alloy, and non-Pt oxygen reduction catalysts for PEMFCs. Applied Catalysis B: Environmental 2005 Mar 10;56(1-2):9-35.

(10) E.J.Carlson, P.Kopf, J.Sinha, S.Sriramulu, Y.Yang. Cost Analysis of PEM Fuel Cell Systems for Transportation. 2005 Dec 1. Report No: NREL/SR-560-39104.

(11) Mehta V, Cooper JS. Review and analysis of PEM fuel cell design and manufacturing. Journal of Power Sources 2003 Feb 25;114(1):32-53.

(12) Mark Hampden-Smith, Paolina Atanassova, Plamen Atanassov, Toivo Kodas. Manufacture of Electrocatalyst Powders by a Spray-based Production Platform. The Handbook of Fuel Cell Technology, Volume 3, Chapter 3.3.4 2006.

(13) Song D, Wang Q, Liu Z, Eikerling M, Xie Z, Navessin T, et al. A method for optimizing distributions of Nafion and Pt in cathode catalyst layers of PEM fuel cells. Electrochimica Acta 2005 May 30;50(16-17):3347-58.

(14) Song D, Wang Q, Liu Z, Navessin T, Holdcroft S. Numerical study of PEM fuel cell cathode with non-uniform catalyst layer. Electrochimica Acta 2004 Nov 30;50(2-3):731-7.

(15) Wee JH, Lee KY, Kim SH. Fabrication methods for low-Pt-loading electrocatalysts in proton exchange membrane fuel cell systems. Journal of Power Sources 2007 Mar 20;165(2):667-77.

(16) Saha MS, Gullβ AF, Allen RJ, Mukerjee S. High performance polymer electrolyte fuel cells with ultra-low Pt loading electrodes prepared by dual ion-beam assisted deposition. Electrochimica Acta 2006 Jun 5;51(22):4680-92.

(17) Kim H, Subramanian NP, Popov BN. Preparation of PEM fuel cell electrodes using pulse electrodeposition. Journal of Power Sources 2004 Nov 15;138(1-2):14-24.

(18) Antoine O, Durand R. In Situ Electrochemical Deposition of Pt Nanoparticles on Carbon and Inside Nafion. Electrochemical and Solid-State Letters 2001 May;4(5):A55-A58.

(19) Andrew T.Haug, Narender Rana, Timothy Stoner, Steven Shi, Wayne Huang, John W.Weidner, et al. Increasing Proton Exchange Membrane Fuel Cell Catalyst Effectiveness Through Sputter Deposition. Journal of The Electrochemical Society 2002 Jan 29;149(3):A280-A287.

(20) Hayre R, Lee SJ, Cha SW, Prinz F. A sharp peak in the performance of sputtered platinum fuel cells at ultra-low platinum loading. Journal of Power Sources 2002 Jul 1;109(2):483-93.

(21) Caillard A, Coutanceau C, Brault P, Mathias J, Lager JM. Structure of Pt/C and PtRu/C catalytic layers prepared by plasma sputtering and electric performance in direct methanol fuel cells (DMFC). Journal of Power Sources 2006 Nov 8;162(1):66-73.

(22) Wee JH. Reply to D. Gruber's comment on my previous paper. Journal of Power Sources 2007 Nov 8;173(1):644-5.

(23) Gruber D. Comment on "Fabrication methods for low-Pt-loading electrocatalysts in proton exchange membrane fuel cell systems" [J.-H. Wee, K.-Y. Lee, S.H. Kim, J. Power Sources 165 (2007) 667-677]. Journal of Power Sources 2007 Nov 8;173(1):642-3.

(24) Debe MK, Schmoeckel AK, Vernstrom GD, Atanasoski R. High voltage stability of nanostructured thin film catalysts for PEM fuel cells. Journal of Power Sources 2006 Oct 27;161(2):1002-11.

(25) Gulla AF, Saha MS, Allen RJ, Mukerjee S. Dual Ion-Beam-Assisted Deposition as a Method to Obtain Low Loading-High Performance Electrodes for PEMFCs. Electrochemical and Solid-State Letters 2005 Oct;8(10):A504-A508.

(26) Cunningham N, Irissou E, Lefevre M, Denis MC, Guay D, Dodelet JP. PEMFC Anode with Very Low Pt Loadings Using Pulsed Laser Deposition. Electrochemical and Solid-State Letters 2003 Jul;6(7):A125-A128.

(27) Paschos O, Choi P, Efstathiadis H, Haldar P. Synthesis of platinum nanoparticles by aerosol assisted deposition method. Thin Solid Films 2008 Apr 30;516(12):3796-801.

(28) Park HS, Cho YH, Cho YH, Jung CR, Jang JH, Sung YE. Performance enhancement of PEMFC through temperature control in catalyst layer fabrication. Electrochimica Acta 2007 Dec 1;53(2):763-7.

(29) Rajalakshmi N, Dhathathreyan KS. Catalyst layer in PEMFC electrodes--Fabrication, characterisation and analysis. Chemical Engineering Journal 2007 May 1;129(1-3):31-40.

(30) Prasanna M, Cho EA, Lim TH, Oh IH. Effects of MEA fabrication method on durability of polymer electrolyte membrane fuel cells. Electrochimica Acta 2008 Jun 30;53(16):5434-41.

(31) Attwood PA, McNicol BD, Short RT. The electrocatalytic oxidation of methanol in acid electrolyte: preparation and characterization of noble metal electrocatalysts supported on pre-treated carbon-fibre papers. Journal of Applied Electrochemistry 1980 Mar 1;10(2):213-22.

(32) Frelink T, Visscher W, van Veen JAR. Particle size effect of carbon-supported platinum catalysts for the electrooxidation of methanol. Journal of Electroanalytical Chemistry 1995 Feb 7;382(1-2):65-72.

(33) Takasu Y, Ohashi N, Zhang X-G, Murakami Y, Minagawa H, Sato S, et al. Size effects of platinum particles on the electroreduction of oxygen. Electrochimica Acta 1996;41(16):2595-600.

(34) Watanabe M, Saegusa S, Stonehart P. High platinum electrocatalyst utilizations for direct methanol oxidation. Journal of Electroanalytical Chemistry 1989;271(1-2):213-20.

(35) R. Maric, Spray-based and CVD Processes for Synthesis of Fuel Cell Catalysts and Thin Catalyst Layers, PEM Fuel Cell Electrocatalysts and Catalyst Layers, Springer London 2008 DOI 10.1007/978-1-84800-936-3_20

(36) R.Maric, A.Tuck, R.Neagu, K.Fatih, J.Roller. Novel Processing of Low Loading Catalyst Layers. 2007 Fuel cell seminar & exposition. ECS Transactions, 2008

(37) Charojrochkul S, Choy KL, Steele BCH. Flame assisted vapour deposition of cathode for solid oxide fuel cells. 1. Microstructure control from processing parameters. Journal of the European Ceramic Society 2004 Jul;24(8):2515-26.

(38) Charojrochkul S, Lothian RM, Choy KL, Steele BCH. Flame assisted vapour deposition of cathode for solid oxide fuel cells. 2. Modelling of processing parameters. Journal of the European Ceramic Society 2004 Jul;24(8):2527-35.

(39) Song H, Xia C, Meng G, Peng D. Preparation of Gd2O3 doped CeO2 thin films by oxy-acetylene combustion assisted aerosol-chemical vapor deposition technique on various substrates and zone model for microstructure. Thin Solid Films 2003 Jun 23;434(1-2):244-9.

(40) Breitkopf-Richard, Hwang-Jan, Maniei-Farzaneh, Hunt-Andrew. Carbon supported Pt nanaomaterials for fuel cell applications using combustion chemical vapor condensation. 2003 p. 490-2.

(41) Hwang TJ. Platinum-catalyzed polymer electrolyte membrane for fuel cells. 2000 p. 239-46.

(42) Hunt ATeal. Combustion chemical vapor deposition: A novel thin-film deposition technique. Appl Phys Lett 1993 Apr 21;63:266-8.

(43) Liu Y, Rauch W, Meilin Liu. Nano-Particles And Nanostructured Electrodes Fabricated By Combustion CVD. 2002 p. 205-14.

(44) Xu-Zhigang, Sankar-Jag, Wei-. Combustion chemical vapor deposition of YSZ thin films for fuel cell applications. 2001.

(45) Ying Liu. Fabrication of Nanostructured Electrodes and Interfaces Using Combustion CVD. Georgia Tech; 2005.

(46) Xu Z, Sankar J, Yarmolenko S. Yttria-stabilized zirconia coatings produced using combustion chemical vapor deposition. Surface and Coatings Technology 2004 Jan 30;177-178:52-9.

(47) Wang HB, Meng GY, Peng DK. Aerosol and plasma assisted chemical vapor deposition process for multi-component oxide La0.8Sr0.2MnO3 thin film. Thin Solid Films 2000 Jun 15;368(2):275-8.

(48) Wang HB, Song HZ, Xia CR, Peng DK, Meng GY. Aerosol-assisted MOCVD deposition of YDC thin films on (NiO + YDC) substrates. Materials Research Bulletin 2000 Nov;35(14-15):2363-70.

(49) Song HZ, Wang HB, Zha SW, Peng DK, Meng GY. Aerosol-assisted MOCVD growth of Gd2O3-doped CeO2 thin SOFC electrolyte film on anode substrate. Solid State Ionics 2003 Jan;156(3-4):249-54.

(50) Meng G, Song H, Dong Q, Peng D. Application of novel aerosol-assisted chemical vapor deposition techniques for SOFC thin films. Solid State Ionics 2004 Nov 30;175(1-4):29-34.

(51) Wang HB, Xia CR, Meng GY, Peng DK. Deposition and characterization of YSZ thin films by aerosol-assisted CVD. Materials Letters 2000 May;44(1):23-8.

(52) Song H, Xia C, Jiang Y, Meng G, Peng D. Deposition of Y2O3 stabilized ZrO2 thin films from Zr(DPM)4 and Y(DPM)3 by aerosol-assisted MOCVD. Materials Letters 2003 Aug;57(24-25):3833-8.

(53) Liu Y, Rauch W, Zha S, Liu M. Fabrication of Sm0.5Sr0.5CoO3-[delta]-Sm0.1Ce0.9O2-[delta] cathodes for solid oxide fuel cells using combustion CVD. Solid State Ionics 2004 Jan 30;166(3-4):261-8.

(54) Liu-Ying, Zha-Shaowu, Liu-Meilin. Novel nanostructured electrodes for solid oxide fuel cells fabricated by combustion chemical vapor deposition (CVD). Advanced Materials 2004 Feb 3;16(3):256-60.

(55) Liu Y, Compson C, Liu M. Nanostructured and functionally graded cathodes for intermediate temperature solid oxide fuel cells. Journal of Power Sources 2004 Nov 15;138(1-2):194-8.

(56) Choy KL, Wiedemann I, .Derby B. Flame-Assisted Deposition of Lead Titanate-Based Thin Films; Correlation of Deposition Process, Microstructure and Electrical Properties. In: F.R.Sale, editor. *Novel Synthesis and Processing of Ceramics*.London: The Institute of Materials, London, U.K., 1994.; 1994. p. 133-42.

(57) Charojrochkul S, Choy K-L, Steele BCH. Cathode/electrolyte systems for solid oxide fuel cells fabricated using flame assisted vapour deposition technique. Solid State Ionics 1999 Jun;121(1-4):107-13.

(58) Charojrochkul S, Choy KL, Steele BCH. Flame assisted vapour deposition of cathode for solid oxide fuel cells. 1. Microstructure control from processing parameters. Journal of the European Ceramic Society 2004 Jul;24(8):2515-26.

(59) Madler L, Kammler HK, Mueller R, Pratsinis SE. Controlled synthesis of nanostructured particles by flame spray pyrolysis. Journal of Aerosol Science 2002 Feb;33(2):369-89.

(60) Madler L, Stark W, Pratsinis S. Flame-made ceria nanoparticles. 17 ed. 2008. p. 1356-62.

(61) Kuo K. K. Principles of Combustion. 2nd ed. Wiley-Interscience; 2008.

(62) Xu Z. Yttria-stabilized zirconia coatings produced using combustion chemical vapor deposition. Surface and Coatings Technology 2004;177-178:52-9.

(63) Thornton JA. High Rate Thick Film Growth. Annual Review of Materials Science 1977 Aug 21;7(1):239-60.

(64) Thornton JA. Influence of apparatus geometry and deposition conditions on the structure and topography of thick sputtered coatings. Journal of Vacuum Science and Technology 1974 Jul;11(4):666-70.

(65) Polley TA, Carter WB. Zone model for zinc oxide deposited by combustion chemical vapor deposition. Thin Solid Films 2001 Mar 15;384(2):177-84.

(66) Pratsinis S. E. Flame aerosol synthesis of ceramic powders. Progress in Energy and Combustion Science 1998;24(3):197-219.

(67) Kammler H. K. (CH), Pratsinis S. (CH), inventors; Composite carbon clack-fumed silica nanostructured particles. EP1122212. 2001 Aug 8.

(68) Strobel R, Pratsinis SE. Flame aerosol synthesis of smart nanostructured materials. Journal of Materials Chemistry 2007 Nov 25;17(45):4743-56.

(69) Stark W. J. (CH), Maedler L. (CH), Pratsinis S. E. (CH), inventors; Metal oxides prepared by flame spray pyrolysis. WO2004005184. 2004 Jan15.

(70) R.Breitkopf, F.Maniei, A.Hunt, J.Hwang. Carbon Supported Pt Nanomaterials for Fuel Cell Applications Using Combustion Chemical Vapor Condensation. NSTI Nanotech 2003 Conference Technical Program Abstract. 2003 p.490-2.

(71) Lee-Stein, Breitkopf-Richard, Hwang-Jan, Faguy-Peter, Hunt-Andrew. A versatile nanofabrication technology for polymer/inorganic composites for fuel cell and pulse power applications. NSTI Nanotech 2003 Conference Technical Program Abstract p.486-9.

(72) Faguy PM, Miller CM, Hunt AT, Hwang JT-J, inventors; Fuel cell having improved catalytic layer. 20040185325. 2004 Sep 23.

(73) Hwang, T.J. ; Shao, H. ; Richards, N. ; Schmitt, J. ; Hunt, A. ; Lin, W.Y. Platinum-catalyzed polymer electrolyte membrane for fuel cells. 1999 Materials Research Society Spring Meeting, San Francisco, CA Materials Research Society symposium proceedings, Volume 575, 2000 Jul 1.

(74) R.Maric, J.Roller, T.Vanderhoek, inventors; National Research Council Of Canada, assignee. Reactive Spray Formation Of Coatings and Powders. BC, Canada patent WO/2007/045089. 2007 Apr 26.

(75) Nanomiser Device. http://www ngimat com/technology/nanomiser html 2008 [cited 2008 Oct 11];Available from: URL: http://www.ngimat.com/technology/nanomiser.html

(76) Deshpande G, Jones M, Hunt A. Silica-Based Oxygen Barrier Coatings onto PET Films via Combustion Chemical Vapor Deposition. Proceedings of the Annual Technical Conference- Society of Vacuum Coaters. 2002, ISSU 45, pages 93-95

(77) Oljaca M, Lovelace C, Xing Y, Shanmugham S, Hunt A. Flame synthesis of nanopowders via combustion chemical vapor deposition. Journal of Materials Science Letters, Vol. 21, No. 8, 15 April 2002 , pp. 621-626(6)

(78) NanoSpray Combustion Processing. http://www ngimat com/technology/index html 2008 October 11 [cited 2008 Oct 11];

(79) Antolini E, Giorgi L, Pozio A, Passalacqua E. Influence of Nafion loading in the catalyst layer of gas-diffusion electrodes for PEFC. Journal of Power Sources 1999 Feb;77(2):136-42.

(80) Gode P, Jaouen F, Lindbergh G, Lundblad A, Sundholm G. Influence of the composition on the structure and electrochemical characteristics of the PEFC cathode. Electrochimica Acta 2003 Dec 15;48(28):4175-87.

(81) Parthasarathy A, Martin CR, Srinivasan S. Investigations of the O[sub 2] Reduction Reaction at the Platinum/Nafion[registered sign] Interface Using a Solid-State Electrochemical Cell. Journal of The Electrochemical Society 1991 Apr;138(4):916-21.

(82) Guangchun Li, Peter G.Pickup. Ionic Conductivity of PEMFC Electrodes Effect of Nafion Loading. Journal of The Electrochemical Society 2003;150(11):C745-C752.

(83) Passalacqua E, Lufrano F, Squadrito G, Patti A, Giorgi L. Nafion content in the catalyst layer of polymer electrolyte fuel cells: effects on structure and performance. Electrochimica Acta 2001 Jan 1;46(6):799-805.

(84) Wilson MS, Gottesfeld S. Thin-film catalyst layers for polymer electrolyte fuel cell electrodes. Journal of Applied Electrochemistry 1992 Jan 21;22(1):1-7.

(85) Chaparro AM, Benitez R, Gubler L, Scherer GG, Daza L. Study of membrane electrode assemblies for PEMFC, with cathodes prepared by the electrospray method. Journal of Power Sources 2007 Jun 10;169(1):77-84.

(86) Malek K, Eikerling M, Wang Q, Navessin T, Liu Z. Self-Organization in Catalyst Layers of Polymer Electrolyte Fuel Cells. J Phys Chem C 2007 Sep 13;111(36):13627-34.

(87) Qi Z, Kaufman A. Low Pt loading high performance cathodes for PEM fuel cells. Journal of Power Sources 2003 Jan 1;113(1):37-43.

(88) Baturina OA, Wnek GE. Characterization of Proton Exchange Membrane Fuel Cells with Catalyst Layers Obtained by Electrospraying. Electrochemical and Solid-State Letters 2005 Jun;8(6):A267-A269.

(89) Kinoshita K. Particle Size Effects for Oxygen Reduction on Highly Dispersed Platinum in Acid Electrolytes. Journal of The Electrochemical Society 1990 Mar;137(3):845-8.

(90) Kim Kinoshita. Electrochemical oxygen technology. New York : Wiley, c1992.; 1992.

(91) Kuzume A, Herrero E, Feliu JM. Oxygen reduction on stepped platinum surfaces in acidic media. Journal of Electroanalytical Chemistry 2007 Jan 15;599(2):333-43.

(92) Wilkinson D, Campbell S, Davis M, St-Pierre J, Johnson M, Ralph T, et al. Low Cost Electrodes for Proton Exchange Membrane Fuel Cells - Performance in Single Cells and Ballard Stacks. J Electrochem Soc 1997 Nov 1;144(11):3845-57.

(93) Steven Holdcroft, Qianpu Wang, Michael Eikerling, Datong Song, Zhongsheng Liu, Titichai Navessin, et al. Functionally Graded Cathode Catalyst Layers for Polymer Electrolyte Fuel Cells I. Theoretical Modeling. J Electrochem Soc 2004 May 19;151(7):A950-A957.

(94) Maass S, Finsterwalder F, Frank G, Hartmann R, Merten C. Carbon support oxidation in PEM fuel cell cathodes. Journal of Power Sources 2008 Feb 1;176(2):444-51.

(95) Chhina H, Campbell S, Kesler O. An oxidation-resistant indium tin oxide catalyst support for proton exchange membrane fuel cells. Journal of Power Sources 2006 Oct 27;161(2):893-900.

(96) Halalay I, Merzougui B, Carpenter M, Swathirajan S, Garabedian G, Mance A, et al., inventors; General Motors Global Technology Operations I, assignee. Supports for Fuel Cell Catalysts. Michigan, USA patent WO/2006/119147. 2006 Nov 9.

(97) Gruber D, Ponath N, Muller J, Lindstaedt F. Sputter-deposited ultra-low catalyst loadings for PEM fuel cells. Journal of Power Sources 2005 Oct 4;150:67-72.

(98) Makharia R, Mathias MF, Baker DR. Measurement of Catalyst Layer Electrolyte Resistance in PEFCs Using Electrochemical Impedance Spectroscopy. Journal of The Electrochemical Society 2005 May;152(5):A970-A977.

(99) Wang Q, Eikerling M, Song D, Liu ZS. Modeling of Ultrathin Two-Phase Catalyst Layers in PEFCs. Journal of The Electrochemical Society 2007 Jun;154(6):F95-F101.

(100) Neyerlin KC, Gu W, Jorne J, Clark J, Gasteiger HA. Cathode Catalyst Utilization for the ORR in a PEMFC. Journal of The Electrochemical Society 2007 Feb;154(2):B279-B287.

(101) Farhat ZN. Modeling of catalyst layer microstructural refinement and catalyst utilization in a PEM fuel cell. Journal of Power Sources 2004 Nov 15;138(1-2):68-78.

(102) Eikerling MH, Malek K, Wang Q. Catalyst Layer Modeling: Structure, Properties and Performance. 2008. p. 381-446.

(103) Bonakdarpour A, Stevens K, Vernstrom GD, Atanasoski R, Schmoeckel AK, Debe MK, et al. Oxygen reduction activity of Pt and Pt-Mn-Co electrocatalysts sputtered on nano-structured thin film support. Electrochimica Acta 2007 Dec 1;53(2):688-94.

(104) Andreas Graichen. 3M Brennstoffzellen-technologie. http://www brennstoffzelle-nrw de 2007 [cited 2008 Sep 4];

(105) H.A. Gasteiger, W. Gu, R. Makhatia, M.F. Mathias, and B. Sompalli, in Handbook of Fuel Cells-Fundamentals, Technology and Applications, W. Veilstich, A. Lamm, and H. Gasteiger, Editors, Vol. 3, p. 593, Wiley, Weinhem (2003).

(106) Hirano S, Kim J, Srinivasan S. High performance proton exchange membrane fuel cells with sputter-deposited Pt layer electrodes. Electrochimica Acta 1997;42(10):1587-93.

(107) Alvisi M, Galtieri G, Giorgi L, Giorgi R, Serra E, Signore MA. Sputter deposition of Pt nanoclusters and thin films on PEM fuel cell electrodes. Surface and Coatings Technology 2005 Nov 21;200(5-6):1325-9.

(108) Chang CL, Chang TC, Ho WY, Hwang JJ, Wang DY. Electrochemical performance of PEM fuel cell with Pt-Ru electro-catalyst layers deposited by sputtering. Surface and Coatings Technology 2006 Dec 20;201(7):4442-6.

(109) Ticianelli EA, Beery JG, Srinivasan S. Dependence of performance of solid polymer electrolyte fuel cells with low platinum loading on morphologic characteristics of the electrodes. Journal of Applied Electrochemistry 1991 Jul 1;21(7):597-605.

(110) Scheiba F, Benker N, Kunz U, Roth C, Fuess H. Electron microscopy techniques for the analysis of the polymer electrolyte distribution in proton exchange membrane fuel cells. Journal of Power Sources 2008 Mar 1;177(2):273-80.

(111) Wagner C, Moulder J, Davis I, Riggs W. Handbook of X-ray photoelectron spectroscopy. 1 ed. Eden Prairie, MN: Perkin-Elmer Corp.; 1979.

(112) Weaver JF, Chen JJ, Gerrard AL. Oxidation of Pt(111) by gas-phase oxygen atoms. Surface Science 2005 Nov 1;592(1-3):83-103.

(113) Hall SC, Subramanian V, Teeter G, Rambabu B. Influence of metal-support interaction in Pt/C on CO and methanol oxidation reactions. Solid State Ionics 2004 Nov 30;175(1-4):809-13.

(114) He B, Ha Y, Liu H, Wang K, Liew KY. Size control synthesis of polymer-stabilized water-soluble platinum oxide nanoparticles. Journal of Colloid and Interface Science 2007 Apr 1;308(1):105-11.

(115) Tu WY, Liu WJ, Cha CS, Wu BL. Study of the powder/membrane interface by using the powder microelectrode technique I. The Pt-black/Nafion interfaces. Electrochimica Acta 1998 Aug 21;43(24):3731-9.

(116) Lin R.B., Shih S.M. Kinetic analysis of the hydrogen oxidation reaction on Pt-black/Nafion electrode. Journal of Solid State Electrochemistry 2006 Apr 11;10(4):243-9.

(117) Lamy-Pitara E, Barbier J. Platinum modified by electrochemical deposition of adatoms. Applied Catalysis A: General 1997 Jan 23;149(1):49-87.

(118) Grolleau C, Coutanceau C, Pierre F, Lager JM. Effect of potential cycling on structure and activity of Pt nanoparticles dispersed on different carbon supports. Electrochimica Acta 2008 Oct 15;53(24):7157-65.